DESIGN AND DEVELOPMENT OF METAMATERIAL BASED MICROWAVE COMPONENTS

Thesis

Submitted in partial fulfilment of the requirements for the degree of

Doctor of Philosophy

in

Electronics and Communication Engineering

by

Priyanka Garg

2K16/PHD/EC/16

Under the guidance of

Dr Priyanka Jain



DEPARTMENT OF ELECTRONICS & COMMUNICATION ENGINEERING
DELHI TECHNOLOGICAL UNIVERSITY, NEW DELHI, INDIA

SEPTEMBER 2020

DECLARATION

I hereby declare that the work which is being presented in the thesis entitled "Design and De-

velopment of Metamaterial Based Microwave Components" submitted to the Department

of Electronics and Communication Engineering, Delhi Technological University (New Delhi)

in partial fulfilment of the requirements for the award of the degree of Doctor of Philosophy is

a bonafide work carried out during the period from 2016 to 2020 by me under the guidance of

Dr Priyanka Jain, Associate Professor, Department of Electronics and Communication Engi-

neering, Delhi Technological University, Delhi, India. The content of this thesis has not been

submitted anywhere for any award. Where other sources of information have been used, they

have been acknowledged.

Date: 10 SEPT 2020

Priyanka Garg

Place: DTU, New Delhi

CERTIFICATE

Certified that **Priyanka Garg** (2K16/PHD/EC/16) has carried out the research work presented

in this thesis entitled "Design And Development of Metamaterial based Microwave Com-

ponents" for the award of **Doctor of Philosophy** from Delhi Technological University, New

Delhi under my supervision. The thesis embodies results of original work, and studies are

carried out by the student herself and the contents of the thesis do not form the basis for the

award of any other degree to the candidate or to anybody else from this or any other Univer-

sity/Institution.

Dr. Priyanka Jain

(Supervisor)

Associate Professor

Delhi Technological University

New Delhi, INDIA

Date: 10 SEPT 2020

The Viva Voce Examination was successfully held at Delhi Technological University, New

Delhi on 10 SEPT 2020

ABSTRACT

Planar technology has gained a lot of popularity since its inception due to various advantages it offered to the scientific world such as, light weight, compact size, ease of fabrication and integration, suitability of mass production and compatibility with planar solid state devices. However they also have certain drawbacks in terms of bandwidth, further miniaturization, gain, efficiency, etc.

Metamataterials are introduced in the late 60s by a Russian physicist Victor Veselago [1], which were further investigated by Pendry *et. al.* [2] and are an active area of research these days. Metamaterials are the artificially engineered structures that offer extraordinary electromagnetic properties not found in nature such as epsilon negative media (ENG), mu negative media (MNG), double negative media (DNG), photonic band gap structures etc. They consist of multiple unit cells whose dimensions are much smaller than $\lambda_0/4$, where λ_0 is the wavelength corresponding to the highest frequency of operation, to achieve homogenization. It was discovered that these materials alter the behaviour of electromagnetic waves in an unconventional way leading to important phenomenon such as, reversal of Snells Law, Doppler effect and Vavilov-Cerenkov radiation.

Due to the extraordinary behaviour of metamaterials they are used to improve the properties of various planar devices and components which are discussed earlier. They can be used to improve antenna's gain, directivity, bandwidth and size, filter's size, roll off, out of band rejection levels and bandwidth. They are used for multiple frequency operation. They are also being used for the development of super lenses, ultrathin perfect absorbers, cloaks, high sensitivity and high resolution sensors, phase compensator etc. The main focus of this thesis is on metamaterial based antennas, filters and absorbers.

Chapter 3 presents the design of a compact, low-profile, coplanar waveguide (CPW)-fed metamaterial inspired dual band microstrip antenna for WLAN application. To achieve the goal a triangular split ring resonator (TSRR) is used along with an open ended stub. The proposed antenna has a compact size of 20×24 mm² fabricated on an FR-4 epoxy substrate with dielectric constant (ε_r =4.4). The antenna provides two distinct bands I from 2.40-2.48 GHz and II from 4.7-6.04 GHz with reflection coefficient better than -10 dB, covering the entire WLAN (2.4/5.2/5.8 GHz) band spectrum. The performance of this metamaterial inspired antenna is also studied in terms of the radiation pattern, efficiency, and realized gain. The antenna is practically fabricated and tested to show good agreement with the simulated results.

Chapter 4 is divided into four sections. The first section presents a compact, low-profile Band Stop Filter (BSF) designed using Complimentary Split Ring Resonator (CSRR). An equivalent circuit model is also presented along with the simplified mathematical approach to extract the parameters of the circuit model. This paper also presents the effect of variation in the dimensions of split rings on characteristics of BSF. The proposed BSF has a compact size of $27 \times 20 \text{ }mm^2$ designed on FR-4 substrate with dielectric constant (ε_r) =4.3. The filter provides complete suppression of the band at 2.4 GHz. The design and circuit analysis of this metamaterial based filter is presented in terms of reflection coefficient, transmission coefficient and impedance curve. The second section presents the design and analysis of a metamaterial inspired Bandstop Filter (BSF) providing suppression of frequency at 3 GHz. The overall size of proposed BSF is $20mm \times 20mm \times 1.6mm$. Further, the extraction of lumped parameters of the designed BSF using simulated results is presented and validation of the results using equivalent circuit simulation is also presented. The third section presents a comparison based study of microstrip transmission line based bandstop filters taking different complementary resonators on the ground plane. Six metamaterial resonators unit cells have been investigated from the literature. The dimensions are optimized to operate at 3 GHz and then their comparative analysis is performed based on various properties of filters such as insertion loss, 3 dB

bandwidth, quality factor (Q), shape factor, overall size, unit cell size and group delay. There are a number of metamaterial based resonators available in literature, so the objective of this section of the chapter is to provide a comparative analysis so that the user can point out the best configuration required while designing the bandstop filter that suits the desired specification and also helps in developing the future ideas by taking into account the advantages of the available structures. The forth section presents a compact, low-profile, Band Pass Filter (BPF) based on balanced Dual Composite Right/Left Handed (D-CRLH) Transmission Line (TL) is presented in this chapter. A balanced D-CRLH TL can be used to provide wideband filter characteristics due to no frequency separation between the RH and LH frequency bands. The proposed D-CRLH TL is designed using U-shaped complementary split ring resonator (UCSRR). The extraction of equivalent circuit model of proposed UCSRR unit cell is also performed. Further, the bandwidth of the proposed filter is enhanced by using the concept of electric and magnetic coupling between the slot lines. The proposed via less BPF has a compact size of 15×15 mm² designed on an FR-4 substrate with dielectric constant(ε_r)=4.3. The design analysis of proposed bandpass filter is presented in terms of reflection coefficient, transmission coefficient, impedance curve, propagation constant and group delay.

Chapter 5 presents a novel resonant metamaterial absorber exhibiting five resonant peaks with absorptivity more than 90% in the range from S band to Ku band for radar cross-section reduction and other FCC-airborne applications. The structure is designed on a low cost FR-4 substrate with 1 mm thickness which is equivalent to $\lambda/17.75$ where λ is the wavelength corresponding to maximum resonant frequency of absorption, showing its ultrathin nature. The fourfold symmetry of the design results in polarization insensitivity and provides an angular stability up to 60° of incident angle. The multiband characteristics are obtained by combining three different geometries in a single structure. Performance of the absorber is studied in terms of absorptivity, material parameters, normalized impedance, polarization insensitivity and oblique incidence. Finally, the design is fabricated on a $200\times200mm^2$ FR-4 substrate and measurements are performed. Further, the chapter also presents a closed meander line shaped

metamaterial absorber operating at 3.5 GHz WiMAX band. The proposed metamaterial absorber unit cell has a compact size of $0.11\lambda_0\times0.11\lambda_0$ design on an ultrathin FR-4 substrate with thickness $0.018\lambda_0$, where λ_0 is the wavelength corresponding to operating frequency. The proposed absorber shows an absorptivity of 98.5 % at the intended frequency. The design is evolved from a simple square loop to a symmetrical meander line structure whose dimensions are optimized to operate at 3.5 GHz WiMAX band. An equivalent circuit model is also defined to depict the electrical properties of the structure. The proposed design also shows insensitivity to polarization as well as change in incident angle of the wave over a wide-angle (upto 60°) for both TE and TM polarization. The proposed structure is a good candidate for radar cross section reduction of an antenna.

Chapter 6 demonstrates the use of metamaterial absorber (MA) to achieve high isolation between two patch antennas in a 2-element MIMO system operating at 5.5 GHz resonant frequency useful for WiMAX application. The proposed flower shaped MA, designed on a $9 \times 9mm^2$ FR-4 substrate with 1 mm thickness, exhibits near unity normalized impedance at 5.5 GHz with an absorptivity of 98.7 %. A 4 element array of the MA is arranged in the form of a line in the middle of the two radiating patches in order to suppress the propagation of surface current between them at the operating frequency. Using the proposed flower shaped MA, an isolation of nearly 35 dB is achieved. The MIMO structure is studied in terms of return loss, isolation, overall gain, radiation pattern, Envelope Correlation Coefficient (ECC), Diversity Gain (DG), and Total Active Reflection Coefficient (TARC) etc. The structure is finally fabricated and measured to show good agreement with the simulated results.

ACKNOWLEDGMENTS

First and foremost, praises and thanks to God, the almighty, for Divine showers of blessings on me for successful completion of my research work. It is my immense pleasure to express my deepest sense of gratitude and indebtedness to my highly respected and esteemed Supervisor Dr. Priyanka Jain, Delhi Technological University, New Delhi, India for providing sagacious, guidance, all sorts of assistance, fruitful discussions, motivation throughout the research period and sparing invaluable time for thorough editing of the thesis without which the present work could not have been completed. I am also grateful to Head of ECE Deptt., DTU, New Delhi, India for providing necessary facilities. Special thanks to Prof. A. K Verma, retired from Delhi University, South Campus, New Delhi, India and Dr. N. Sridhar for extending kind support and cooperation in my research work, despite their hectic schedules and Mr. Padam Saini of G. B. Pant Engineering College, New Delhi, India for providing measurement facilities in his lab.

My special thanks to my dear colleagues and friends for their active interest, fruitful discussion and help from time to time. I am grateful to my venerable parents whose blessings and constant encouragement have helped me to complete this research work. I express my appreciation to my husband, sisters and all other relatives for their patience and understanding during the time devoted to research.

TABLE OF CONTENTS

D)	ECLA	RATIO	ON	ii
C	ERTI	FICAT	E	iii
A	BSTF	RACT		iv
A	CKN	OWLE	DGMENTS	viii
L	IST O	F ACR	ONYMS	xxii
1.	INT	RODU	CTION	1
	1.1	INTRO	ODUCTION	2
	1.2	BASI	C OVERVIEW	2
	1.3	REAL	JIZATION OF LEFT-HANDED METAMATERIALS	7
		1.3.1	Negative permittivity in the medium using metal wire geometry	7
		1.3.2	Negative permeability in the medium using split ring resonators	8
	1.4	ADVA	NTAGES AND APPLICATIONS	9
		1.4.1	Metamaterial as Antennas	10
		1.4.2	Metamaterial as filter	10
		1.4.3	Metamaterial as Superlens	11
		1.4.4	Metamaterial as Absorber	11
		1.4.5	Metamaterial as cloaks	12
		1.4.6	Metamaterial as sensor	13
		1.4.7	Metamaterial as Phase compensator	13
	1.5	OTHE	R TERMINOLOGIES RELATED TO METAMATERIALS	13
		1.5.1	Backward waves	13

		1.5.2	Electromagnetic band gap structures	15
	1.6	MOTIV	VATION	16
	1.7	CHAL	LENGES IN DESIGN	17
	1.8	RESEA	ARCH PROBLEM STATEMENT	18
	1.9	THESI	S ORGANISATION	19
	1.10	SUMM	IARY	20
2.	LITI	ERATU	RE REVIEW	21
	2.1	ANTE	NNAS	22
	2.2	FILTE	RS	28
		2.2.1	Filter Metrics:	29
		2.2.2	Metamaterial inspired filters	30
	2.3	ABSO	RBERS	38
		2.3.1	Narrowband metamaterial absorber	39
		2.3.2	Multiband metamaterial absorber	40
		2.3.3	Broadband Absorbers	44
3.	MET	ГАМАТ	ERIAL INSPIRED DUAL BAND ANTENNA FOR WLAN APPLI-	ı
	CAT	ION		47
	3.1	MATE	RIAL PARAMETER EXTRACTION	49
	3.2	ANTE	NNA DESIGN AND SIMULATION APPROACH	52
	3.3	RESUI	LTS AND DISCUSSION	55
		3.3.1	Impedance Performance	55
		3.3.2	Radiation Performance	56
		3.3.3	Performance Comparison	57
	3.4	EXPE	RIMENTAL RESULTS AND DISCUSSION	58
	3.5	SHMM	IARY	61

1.	ME	TAMAT	ERIAL BASED FILTERS	62
	4.1	COMP	PLIMENTARY SPLIT RING RESONATOR BACKED MICROSTRIP	
		TRAN	SMISSION LINE USING EQUIVALENT CIRCUIT MODEL	63
		4.1.1	Design and Circuit Simulation Approach	64
		4.1.2	Results and Discussion	69
		4.1.3	Parametric Analysis	72
		4.1.4	Experimental Results and Discussion	73
		4.1.5	Summary	74
	4.2	EXTR	ACTION OF EQUIVALENT CIRCUIT PARAMETERS OF META-	
		MATE	RIAL BASED BANDSTOP FILTER	75
		4.2.1	Design and circuit simulation	75
		4.2.2	Results and Discussion	78
		4.2.3	Summary	78
	4.3	COMP	PARATIVE ANALYSIS OF TRANSMISSION LINE BASED BAND-	
		STOP	FILTERS USING DIFFERENT METAMATERIAL UNIT CELLS OP-	
		ERAT	ING AT 3 GHZ	81
		4.3.1	Design and simulation approach	81
		4.3.2	Design and simulation of metamaterial based filters	82
		4.3.3	Comparative Analysis	93
		4.3.4	Summary	95
	4.4	BAND	PASS FILTER USING DUAL COMPOSITE RIGHT/LEFT HANDED	
		(D-CR	LH) TRANSMISSION LINE SHOWING BANDWIDTH ENHANCE-	
		MENT	2	96
		4.4.1	Design and Simulation Approach	98
		4.4.2	Results and Discussion	101
		4.4.3	Comparison with previously proposed BPF	110
		4.4.4	Experimental Results and Discussion	111

		4.4.5	Summary	111
5.	ME	ГАМАТ	TERIAL ABSORBERS	113
	5.1	NOVE	L ULTRATHIN PENTA-BAND METAMATERIAL ABSORBER	114
		5.1.1	Introduction	114
		5.1.2	Design and Simulation Approach	115
		5.1.3	Equivalent circuit analysis	122
		5.1.4	Results and Discussion	124
		5.1.5	Experimental Results and Discussion	128
		5.1.6	Summary	131
	5.2	DESIG	SN AND ANALYSIS OF METAMATRIAL ABSORBER AT 3.5 GHZ	
		USINC	G EQUIVALENT CIRCUIT MODEL	132
		5.2.1	Design and Simulation Approach	133
		5.2.2	Results and Discussion	135
		5.2.3	Summary	140
6.	ISO	LATIO	N IMPROVEMENT OF MIMO ANTENNA USING A NOVEL FLOW	/ER
	SHA	PED M	IETAMATERIAL ABSORBER AT 5.5 GHZ WIMAX BAND	142
	6.1	PROPO	OSED METAMATERIAL ABSORBER DESIGN AND SIMULATION	144
	6.2	MIMO	ANTENNA DESIGN AND SIMULATION	147
	6.3	MIMO	DIVERSITY PERFORMANCE	150
	6.4	EXPE	RIMENTAL RESULTS AND DISCUSSION	152
	6.5	SUMM	1ARY	153
7.	CON	NCLUS	ION	155
	7.1	CONC	LUSION	156
o	ימי זקן	TIDE O	COPE	160
	X.I	PUTU	RE SCOPE	161

CHRRICHLI	IM VITAE	101	
LIST OF PUBLICATIONS			
REFEREN	NCES	162	
8.1.3	Metamaterial Absorbers	161	
8.1.2	Metamaterial Filters	161	
8.1.1	Metamaterial Antennas	161	

LIST OF TABLES

3.1	Real values of ε, μ, n	52
3.2	Design parameters of the proposed antenna	53
3.3	Performance comparison of the proposed antenna with other reported antennas.	58
3.4	Comparative analysis of proposed antenna and previously proposed antennas	
	operating on WLAN band	59
4.1	Performance comparison table	95
4.2	Design parameters of the proposed BPF	101
4.3	Synthesis Equations based on parametric analysis	110
4.4	Comparative analysis of proposed BPF with previously proposed ones	110
5.1	Design parameters of the proposed unit cell	117
5.2	Simulated result of Proposed Unit cell	124
5.3	Equivalent Circuit Parameters	124
5.4	Values of retrieved parameters with respect to absorption peaks	126
5.5	Comparative analysis of proposed absorber with previously proposed ones .	129
5.6	Design parameters of proposed unit cell	134
5.7	Comparative analysis of proposed absorber with previously proposed ones .	140
6.1	Performance comparison of the MIMO antenna with and without the proposed	
	MA at 5.5 GHz	151
6.2	A comparison of proposed technique with previously presented ones	153

LIST OF FIGURES

1.1	$\varepsilon - \mu$ diagram	3
1.2	(a) Right handed material (b) Left handed material	4
1.3	(a)Geometry for a medium with metallic wire strips, (b) Variation of real part	
	of electric permittivity as a function of frequency	8
1.4	Split Ring Resonator (SRR) Configurations. (a) Square split ring resonator (b)	
	Circular split ring resonator	9
1.5	Variation of effective permeability as a function of frequency	9
1.6	(a) Forward wave supporting RH transmission line (b) Backward wave sup-	
	porting LH transmission line	14
1.7	Dispersion diagram (a) Forward wave line (b) Backward wave line	14
2.1	Structures offering -negative behaviour.	23
2.2	Various available SRR structures	24
2.3	Different CELC structures	26
2.4	SRR structures for reduction of mutual coupling	26
2.5	Variants of DNG structures	28
2.6	DNG structures developed by combining SNG structures	29
2.7	Equivalent circuit model for the ideal CRLH TL	31
2.8	Metamaterial coupled TL filter	33
2.9	Defected Microstrip line filter	34
2.10	Defected Ground structures	36
2.11	Coplanar Waveguide Filters	37
2.12	Narrowband metamaterial absorbers	39

2.13	Unit cell with scaled versions of flower shape (a) Use of different resonant	
	structures (b,c), Rotated versions of unit cell (d,e,f)	41
2.14	Scaled unit cells one within the other	42
2.15	Multi resonant structures	43
2.16	Unit cells with different resonant structures	44
2.17	Unit cells with multi-layered structures	45
2.18	Unit cells with mono-layered structures	46
3.1	Simulation setup of proposed metamaterial unit cell	50
3.2	Real part of permittivity (a), real part of permeability (b), and real part of	
	refractive index (c)	51
3.3	Schematic configuration of the proposed dual band antenna	53
3.4	Stepwise evolution procedure of the proposed antenna	54
3.5	Simulated surface current distributions at (a) 2.45 GHz and (b) 5.45 GHz	55
3.6	Simulated S-Parameters against frequency for the dual band antenna	56
3.7	The simulated radiation pattern at frequencies 2.45 GHz (a), (b), (c), (d) and	
	5.45 GHz (e), (f), (g), (h)	57
3.8	Efficiency and gain plots of the metamaterial antenna	58
3.9	Fabricated prototype of antenna	59
3.10	Measurement of (a) Return loss (b) VSWR on Keysight N9914A vector net-	
	work analyzer	60
3.11	Measured and simulated Return loss	60
4.1	(a)Top microstrip line (b) CSRR etched bottom ground plane	64
4.2	Power flow at (a)1.771 GHz (b)2.4 GHz	66
4.3	(a) Transmission coefficient obtained by design simulation. (b) Impedance	
	curve obtained by design simulation	66
44	Fauivalent circuit of the proposed Randston filter	67

4.3	Transmission coefficient obtained by design and circuit simulation (solid lines	
	show design simulated S-parameters and dashed lines show circuit simulated	
	S-parameters)	70
4.6	(a) Parametric analysis of (a) r_{out} (b) d (c) g	70
4.7	Impedance curve obtained by (a) design simulation, (b) circuit simulation	71
4.8	Transmission coefficient obtained by design and circuit simulation after re-	
	placing inductor L_2 shown in Fig. 4.4 by capacitor C_2 (solid lines show design	
	simulated S-parameters and dashed lines show circuit simulated S-parameters)	72
4.9	Fabricated BSF(a) Top view, (b) Bottom view	73
4.10	Snapshots of results on Keysight N9914A vector network analyzer (a) Return	
	loss (b) Insertion loss	73
4.11	Measured and simulated S-parameters of proposed BSF	74
4.12	Design of proposed bandstop filter (light grey color shows 50 microstrip line	
	on top and dark grey color shows OSSRR on bottom of substrate)	76
4.13	Simulated transmission coefficient and impedance curve of the proposed band-	
	stop filter design.	76
4.14	Equivalent circuit of the proposed Bandstop filter	77
4.15	Reflection and transmission coefficient of simulated design	79
4.16	Reflection and transmission coefficient of simulated equivalent circuit	79
4.17	Impedance Curve (a) Design (b) Equivalent Circuit	79
4.18	(a) Side view of the transmission line (b) Top view of transmission line	82
4.19	(a) CELC-I (b)CELC-II (c)OSSRR (d)CSTR (e)SSRR (f)DSRR	83
4.20	CELC-I based bandstop filter	84
4.21	Equivalent circuit of the CELC-I bandstop filter	84
4.22	CELC-I circuit simulation	86
4.23	Power flow at (a)3 GHz (b)4 GHz	86
4 24	CELC-II based bandston filter	87

4.25	OSSRR based bandstop filter	88
4.26	Equivalent circuit of OSSRR based bandstop filter	89
4.27	OSSRR BSF circuit simulation	89
4.28	SSRR based filter	90
4.29	Equivalent circuit of the SSRR based bandstop filter	91
4.30	SSRR BSF circuit simulation	91
4.31	DSRR based bandstop filter	92
4.32	DSRR BSF circuit simulation	93
4.33	CSTR based bandstop filter	94
4.34	Geometry of UCSRR unit cell showing boundary assignment	99
4.35	Real part of extracted material parameters	100
4.36	Imaginary part of the extracted material parameters	100
4.37	(a)Top capacitively loaded microstrip line (b) UCSRR etched bottom ground	
	plane without slot (c) with vertical slot.	101
4.38	S-parameters of the proposed BPF without slot	102
4.39	Equivalent circuit of the proposed UCSRR filter	103
4.40	Simulated S-parameters obtained after periodic arrangement of the filter	104
4.41	Parametric analysis of the separation between the two U-shaped slots i.e. \boldsymbol{g} .	105
4.42	Surface current density plot at the bottom surface of proposed filter with slot	
	and without slot respectively at 3.75 GHz ((a), (b)) and at 1.5 GHz ((c), (d)) $$.	106
4.43	S-parameters of proposed design with (shown by solid lines) and without ver-	
	tical slot (shown by dotted lines)	107
4.44	S-parameters of the proposed BPF with slot	107
4.45	Dispersion Diagram of bandpass filter without slot (Solid line) and with slot	
	(Dashed line)	108
4.46	Group delay of proposed bandpass filter without slot (Solid line) and with slot	
	(Dashed line)	109

4.47	Variation with respect to (a) g (b) w_{g1} (c) l_{g1}	109
4.48	(a) Measured and simulated S-parameters of proposed filter without slot. (b)	
	Measured and simulated S-parameters of proposed filter after bandwidth en-	
	hancement	111
5.1	Top view of unit cell geometry of (a) Case I (b) Case II (c) Case III (d) Case IV.	116
5.2	Simulated absorptivity of three structures, Case I (-Solid line), Case II (-	
	dashed line) and Case III (dot dashed line)	116
5.3	Simulation set up of unit cell in HFSS	117
5.4	Current density plot on top and bottom surfaces of Case I unit cell at 3.35 GHz.	118
5.5	Current density plot on top and bottom surfaces of Case II unit cell at (a) 5.4	
	GHz, (b) 12.8 GHz, (c) 17.15 GHz	119
5.6	Current density plot on top and bottom surfaces of Case III unit cell at 9.4 GHz	119
5.7	Absorptivity of final unit cell geometry (Case IV)	120
5.8	Current density plot on top and bottom surfaces of Case IV unit cell at (a) 3.35	
	GHz, (b) 5.1 GHz, (c) 9.5 GHz, (d) 11.55 GHz, (e) 16.9 GHz	121
5.9	Electric field distribution plot of the proposed unit cell at the absorption fre-	
	quencies	121
5.10	Equivalent circuit of the proposed metamaterial absorber	123
5.11	Reflection coefficient response due to circuit and design simulation	125
5.12	(a) Variation of (a) real value and (b) imaginary value of effective permittivity	
	and permeability with respect to frequency.	126
5.13	(a) Variation of (a) real value and (b) imaginary value of normalized impedance	
	with respect to frequency	127
5.14	Simulated absorptivity response of structure under (a) various polarization an-	
	gles (b)oblique incidence for TE polarization (c) oblique incidence for TM	
	polarization	127

3.13	(a) Faoricated sample of proposed structure with its emarged portion snown in	
	(b)	130
5.16	Experimental environment for measurement of proposed absorber	130
5.17	Measured reflections from the proposed metamaterial absorber	131
5.18	Measured and simulated absorptivity of proposed metamaterial absorber	132
5.19	Top view (a) and side view (b) of the proposed unit cell	133
5.20	Stepwise evolution of the proposed unit cell	135
5.21	Normalized impedance of the proposed unit cell	136
5.22	Material parameters of the proposed unit cell	136
5.23	Surface Current distribution of the proposed unit cell (a)Top, (b) Bottom	137
5.24	E-field distribution of the proposed unit cell	137
5.25	Equivalent circuit of the proposed metamaterial absorber	138
5.26	Simulated reflection coefficient of the proposed unit cell and its equivalent	
	circuit model	139
5.27	Simulated absorptivity response of structure under (a) various polarization an-	
	gles (b)oblique incidence for TE polarization (c) oblique incidence for TM	
	polarization	139
6.1	(a) Schematic of the proposed metamaterial absorber unit cell. (b) Simulation	
	set up of the proposed MA unit cell	144
6.2	Absorptivities of different metamaterial absorber shapes	145
6.3	(a) Material parameters of metamaterial absorber (b) Normalized impedance	
	of the metamaterial absorber	145
6.4	(a) Surface current density plot of MA at 5.5 GHz (Top view and Bottom view)	
	(b) Volume current density plot of MA at 5.5 GHz	147
6.5	Simulated S-parameters with and without the proposed MA along with 3D	
	view of the proposed MIMO antenna with flower shaped MA	148
6.6	Surface current distribution at 5.5 GHz (a) without MA, (b) with MA	149

6.7	MIMO antenna far field radiation pattern at 5.5 GHz with (-solid line) and	
	without (-dashed line) MA on (a) xz-plane (b) yz-plane (c) xy-plane	150
6.8	Peak gain and radiation efficiency plot of MIMO with and without MA	150
6.9	Simulated ECC and DG of MIMO antenna with MA	151
6.10	Simulated and measured TARC of MIMO antenna with MA	152
6.11	Measured and simulated S-parameters with fabricated prototype of proposed	
	structure	153

LIST OF ACRONYMS

BW Bandwidth

BPF Bandpass Filter

BSF Bandstop Filter

CP Circular Polarization

CPW Coplanar Waveguide

CRLH Complementary Right Left handed Transmission Line

CLS Capacitance loaded strips

CST Computer Simulation Software

CSRR Complimentary Split Ring Resonator

CELC Complementary Electric inductive capacitive resonator

CSTR Complimentary Split Triangle Resonator

D-CRLH Dual-Complementary Right Left handed Transmission Line

DGS Defected Ground Structure

DPS Double Positive media

DNG Double negative media

DG Diversity Gain

DML Defected Microstrip Line

DSRR Double Split Ring Resonator

ENG Epsilon negative media

EM Electromagnetics

ELC Electric inductive capacitive resonator

ECC Envelope Correlation Coefficient

EMI/EMCElectromagnetic Interference/ Electromagnetic Compatibility

ERR Electric Ring Resonator

FCC Federal Communication Commission

GSM Global System for Mobile communication

FEM Finite Element Method

HFSS High Frequency Structure Simulator

IL Insertion Loss

IEEE Institute of Electrical and Electronics Engineers

JC Jerusalem Cross

LTE Long Terms Evolution

LH Left Handed

LPF Low Pass Filter

LTCC Low Temperature Co-fired Ceramic

MNG Mu negative media

MIMO Multiple Input Multiple Output

MA Metamaterial Absorber

MSRR Modified split ring resonators

NRI Negative Refractive Index

NRW Nicolson-Ross-Weir

OCSRR Open Complimentary Split Ring Resonator

OSSRR Open Slot Split Ring Resonator

PCB Printed Circuit Board

PEC Perfect electric

PMC Perfect magnetic

RH Right handed

RF Radio Frequency

RCS Radar Cross Section

SRR Split Ring Resonator

SSRR Single Split Ring Resonator

SMA Sub Miniature Version A

TSRR Triangular Split ring resonator

TL Transmission Line

TARC Total Active Reflection Coefficient

TE Transverse Electric

TM Transverse Magnetic

UWB Ultra Wideband

UCSRR U-shaped Complimentary Split Ring Resonator

UMTS Universal Mobile Telecommunications Service

VNA Vector Network Analyser

VSWR Voltage Standing Wave Ratio

WLAN Wireless Local Area Network

WiMAX World-wide interoperability for Microwave access

Wi-Fi Wireless Fidelity

CHAPTER 1

INTRODUCTION

1.1 INTRODUCTION

1.2 BASIC OVERVIEW

In past few decades, metamaterials have emerged as a new technology in the area of microwave communication engineering. Wide research is being carried out on metamaterials to develop such microwave structures which can provide more advanced and efficient ways of communication.

Most of the isotropic materials existing in nature have positive values of permittivity (ε) and permeability (μ) greater than unity, so, they are considered as double positive (DPS) materials. These recently developed class of structures called metamaterials are materials that are typically engineered with novel or artificial structures, made by unit cells of dimensions much smaller than the wavelength. These unit cells are periodically arranged and tend to exhibit electromagnetic properties that are difficult or unusual to be found in nature. Such properties comprise of a simultaneous negative permeability and permittivity that render into a negative refractive index; since,

$$n = \pm \sqrt{\varepsilon_r \mu_r},\tag{1.1}$$

where, ε_r and μ_r are relative permittivity and relative permeability of medium and n is refractive index. There are four possible combinations in the pair (ε, μ) i.e. (+, +), (-, +), (+, -), (-, -), as shown in Fig. 1.1 The first three combinations are well known conventional materials. First one is Double positive structure (DPS), having positive value of ε and μ , also called right handed materials. Second quadrant gives epsilon negative (ENG) metamaterials having permittivity less than zero and permeability more than zero (ε < 0, μ > 0). Many plasmas display these characteristics in certain frequency ranges. Infinitely long parallel wires arranged in square matrix are also known to have this characteristic. Third combination gives μ -negative (MNG) materials have permittivity greater than zero and permeability less than zero (ε > 0

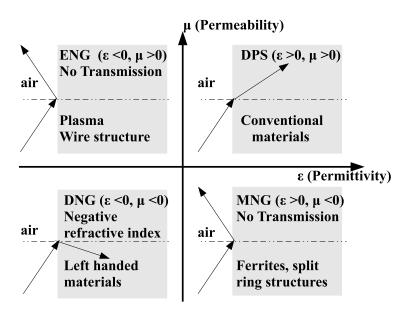


Figure 1.1: $\varepsilon - \mu$ diagram

, μ < 0). Some gyrotropic material presents these characteristic in certain frequency ranges. Split ring structures also exhibit MNG behaviour. Fourth quadrant shows materials having simultaneously negative permittivity and negative permeability called double negative structures (DNG), that are not available in nature. These are also termed as Left handed materials (LHM), negative refractive index media (NRI) or backward wave media. Various ENG and MNG structures can be combined to exhibit DNG behaviour. This type of structures offers a wide scope of research in this area.

Metamaterials can be incorporated with conventional microwave devices such as antennas, filters, absorbers, lenses, matching networks, or sensors to provide exceptional improvement in properties. Electromagnetic properties of metamaterial devices can be engineered by changing the geometry of its unit cells. Subsequently, transmission is altered by adjusting the shape, size, and configurations of the unit cells. This results in control over material parameters known as permittivity and magnetic permeability.

LH materials are called so because they followed a left-hand rule for the wave propagation instead of right-hand rule for the wave equation formed by the E (electric field), H (magnetic

field) and β (propagation constant) vectors. They are observed to have anti-parallel Pointing vector(S) and propagation constant (β) as shown in Fig. 1.2. This behaviour is opposite to that of conventional or right handed materials (RHM) which show parallel direction of S and *beta*. Due to anti-parallel S and β , LHM are observed to have backward wave propagation, which is another unique property shown by metamaterials.

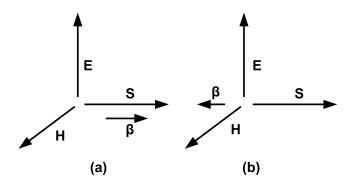


Figure 1.2: (a) Right handed material (b) Left handed material

The above theory can be explained with the help of Maxwell's equation. Let us consider loss-less medium in regions without sources. In case of right handed (RH) medium, ε , $\mu > 0$ and therefore,

$$\beta \times E = +\omega \mu H \tag{1.2}$$

$$\beta \times H = -\omega \varepsilon E \tag{1.3}$$

which forms the familiar right-handed triad (E, H, β) shown in Fig. 1.2(a). Whereas, in case of LH medium, ε , μ < 0, and therefore, since $|\varepsilon| = -\varepsilon > 0$ and $|\mu| = -\mu > 0$,

$$\beta \times E = -\omega |\mu| H \tag{1.4}$$

$$\beta \times H = +\omega |\varepsilon| E \tag{1.5}$$

which builds the left handed triad (E, H, β) shown in Fig. 1.2(b). Since, phase velocity varies

inversely with β , given by,

$$v_p = \omega/\beta, \tag{1.6}$$

Therefore, in LH medium, phase velocity is opposite to that in RH medium.

The values of permittivity and permeability in a material are frequency dependent. There are various models available to describe the frequency response of permittivity and permeability in a material, however, the *Lorentz* model is one of the most popular ones. It is derived by a description of the electron motion in terms of a driven, damped harmonic oscillator. With a time harmonic incident electric field, the equation of motion of free electron is given by:

$$\frac{d^2x}{dt^2} + \gamma \frac{dx}{dt} + \omega_c^2 x = \frac{qE}{m}$$
 (1.7)

where, x is the displacement caused by the incident electric field, m is the mass of electron, γ is the damping coefficient of the oscillations and ω_c is the characteristic resonance frequency. The first term of the Eq. 1.7 accounts for acceleration, second term accounts for dissipation due to collisions or damping, the third term accounts for restoring force and the term on the right hand side accounts for driving electric force experienced by the electrons. For N number of free electrons per unit volume with dipole moment p=qx, the polarization is given as:

$$P = Np = Nqx \tag{1.8}$$

Now, the equation for polarization is give as:

$$\frac{d^2P}{dt^2} + \gamma \frac{dP}{dt} + \omega_c^2 P = \varepsilon_0 \omega_p^2 E \tag{1.9}$$

where, ω_p is the plasma frequency at which the density of electron gas oscillates, given

by:

$$\omega_p = \sqrt{\frac{Nq^2}{\varepsilon_0 m}} \tag{1.10}$$

For a time harmonic incident electric field, the polarization is also time harmonic, $P = P_0 e^{-j\omega t}$. Now the polarization is given by:

$$(\omega_c^2 - \omega^2 - j\omega\gamma)P = \frac{Nq^2}{m}E\tag{1.11}$$

Comparing the above equation with $P = \varepsilon_0 \chi_r E$, where χ_r is the relative susceptibility, we get following expression for relative permittivity:

$$\varepsilon_r = 1 + \frac{\omega_p^2}{\omega_c^2 - \omega^2 - j\omega\gamma} \tag{1.12}$$

Drude model and *Debey* model are the special cases of Lorentz model. In absence of restoring force, ω_c =0, and the Lorentz model reduces to Drude model:

$$\varepsilon_r = 1 - \frac{\omega_p^2}{\omega^2 + j\omega\gamma} \tag{1.13}$$

When the accelerating term is very small, $(\omega_c^2 + j\omega\gamma) >> \omega^2$, the Lorentz model reduces to Debey model.

$$\varepsilon_r = 1 + \frac{\omega_p^2/\omega_c^2}{1 - j\omega(\gamma/\omega_c^2)} \tag{1.14}$$

From the above equations only the Lorentz and Drude models can yield negative permittivity. Since, the Lorentz model is resonant in nature, it yields negative permittivity for a small range of frequency whereas, Drude model yields negative permittivity over a wide range of frequencies.

Similarly, the magnetic response models are realized by the corresponding values in the

above expressions. The permeability function is given by following expression:

$$\mu_r = 1 - \frac{F\omega^2}{\omega^2 - \omega_m^2 + j\omega\gamma} \tag{1.15}$$

Here F is the fractional volume of the unit cell and ω_m is the magnetic resonance frequency.

1.3 REALIZATION OF LEFT-HANDED METAMATERIALS

In 1967, a Russian physicist Viktor Veselago [1] came up with an idea of "Substances with simultaneously negative values of ε and μ ". 30 years later his theory was experimentally demonstrated and the first left handed material was introduced. Pendry *et. al.* demonstrated that an array of wire strips causes negative permittivity [3] and the split ring resonators exhibit negative permeability [2]. Later on the two structures were combined to develop a LH media.

1.3.1 Negative permittivity in the medium using metal wire geometry

From eqn. 1.10, it is clear that the plasma frequency of materials is dependent upon the number of free electrons which is of the order of 10^{23} cm^{-3} in case of metals. Therefore, the plasma frequency lies in the visible and near UV region of the spectrum, below which the effective permittivity is negative, resulting in a Drude type response. Pendry *et. al.* proposed method to reduce the plasma frequency to the far infrared or even GHz band by using periodic sets of metallic wires [3]. Metallic wires reduce the density of free electrons and increase the effective electron mass, thus reducing the plasma frequency. Fig. 1.3 shows the geometry for the periodically placed wire strips and the variation of the real part of the electric permittivity as a function of frequency.

The effective permittivity can be represented by a Drude dielectric function which varies as a function of frequency and can be controlled by geometry of the wire. The plasma frequency

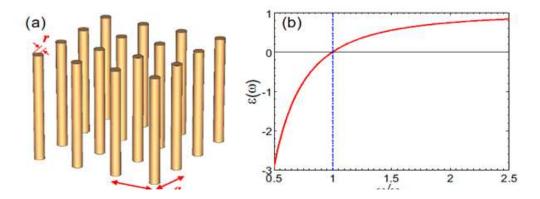


Figure 1.3: (a)Geometry for a medium with metallic wire strips, (b) Variation of real part of electric permittivity as a function of frequency.

of the wire structure used in the designing of a composite material is given as:

$$\omega_p^2 = \frac{2\pi c^2}{a^2 \ln(a/r)} \tag{1.16}$$

Here r is the radius of the wire structure, a is the spacing between the wire strip and c is the speed of light in free space, i.e. 3×10^8 m/s.

1.3.2 Negative permeability in the medium using split ring resonators

At very high frequencies, there is no physical meaning of magnetic permeability, so we usually set μ =1. Pendry *et. al.* demonstrated that a method to improve the magnetic response of a material at high frequencies is to introduce current carrying loops that generate magnetic dipole moment. Fig. 1.4 shows the sub-wavelength sized split ring resonators, made from non-magnetic conducting sheets. It was found that when such structures are periodically arranged and a time varying magnetic field is incident on them normally, a circulating current is produced, generating a opposing magnetic flux. The effective permeability (μ_{eff}) of the split ring resonator can be expressed using eqn 1.15.

The variation of the permeability for the split ring resonator over a range of frequency is shown in the Fig. 1.5.

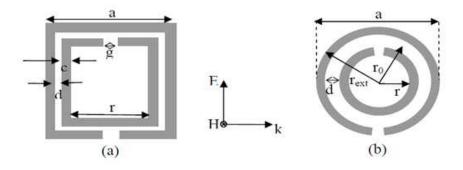


Figure 1.4: Split Ring Resonator (SRR) Configurations. (a) Square split ring resonator (b) Circular split ring resonator

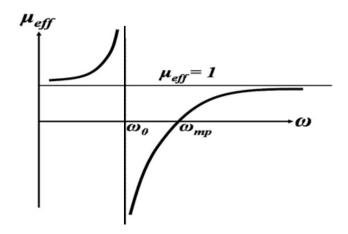


Figure 1.5: Variation of effective permeability as a function of frequency

1.4 ADVANTAGES AND APPLICATIONS

These days, demand of high performance systems is increasing in various domains like sensing, satellite communication (Satcom) and telecommunication, aerospace and defence, optics (terahertz and infrared), and medical instrumentation. Metamaterials can be incorporated with conventional devices and just manipulating their shape, size, orientation, geometry and arrangement enables them to change the behaviour of electromagnetic waves. This provide benefits that are beyond the scope of conventional materials. Few applications of metamaterials

are described below, however, major focus is given to antennas, filters and absorbers.

1.4.1 Metamaterial as Antennas

Metamaterial concepts are widely being used in designing small size patch antennas with better performance [4]. Use of metamaterial helps in improving various properties and drawbacks of patch antennas, such as miniaturizing the antennas, increasing radiation efficiency, reducing radiator size, improving antennas bandwidth and enabling multiband operation. Metamaterials usually reduce the size of antenna to one-fifth of the wavelength by shifting the resonant frequency to lower sides. Metamaterial coatings have been used to increase the directivity, enhance the radiation and matching properties of electrically small electric and magnetic dipole antennas. Metamaterial can enhance the gain, bandwidth and return loss of a patch antenna. Metamaterial based antennas are also known to have reduced mutual coupling when used as an array employing multiple input multiple output (MIMO) systems.

Metamaterial, high-impedance ground planes can also be used to improve the axial ratio and radiation efficiency performance of circularly polarized low profile antennas. Using metamaterials, both the forward and backward waves can be used in leaky wave antennas to increase the beam scanning range. Various metamaterial antenna systems can be employed to assist communication links, navigation systems, surveillance sensors, command and control systems.

1.4.2 Metamaterial as filter

The metamaterials based filters are generally designed by combining a host transmission line with a resonant type metamaterial [5]. Such type of structure offers controllable propagation characteristics. These structures may consist of either one, two or multiple sub-wavelength resonator unit cells. A single cell can not be describes as a metamaterial medium, however, it could be seen that the filtering characteristics observed are due to the metamaterial properties exhibited by the cell. Use of metamaterial in designing filters results in compact size, sharp

roll off, high out of band rejection levels and multiple frequency operation.

1.4.3 Metamaterial as Superlens

There is a diffraction limit in conventional optical materials because only the propagating components are transmitted from a light source while the non-propagating components, also called the evanescent waves, are not transmitted. High-index materials can be used to enhance the resolution, however, there availability is limited. Metamaterials can be used to enhance the refractive index, thus providing a route to the super lens. It has the capability to extensively improve and also recover the evanescent waves that carry very small scale information. This help to achieve resolution beyond diffraction limits [6].

1.4.4 Metamaterial as Absorber

A metamaterial absorber manipulates the loss components of metamaterials' permittivity and magnetic permeability, to absorb large amount of electromagnetic radiations [7]. This is a useful feature for radar cross section reduction, photo-detection and solar photovoltaic applications. When a wave strikes on the surface of the absorber, it may be reflected, transmitted, scattered or absorbed. If we assume negligible scattering due to roughness, then the absorbance $(A(\omega))$ relationship can be given as:

$$A(\omega) = 1 - R(\omega) - T(\omega) \tag{1.17}$$

Where, $R(\omega)$ = Reflectance, obtained as $|S_{11}|^2$ $T(\omega)$ = Transmittance, obtained as $|S_{12}|^2$ Now, for the structure to absorb the EM wave completely, the reflectance $(R(\omega))$ and Transmittance $(T(\omega))$ need to be zero. To get zero $T(\omega)$, the bottom side of the structure is completely covered with copper, which prohibits further propagation of the wave. Now to get zero reflectance the relative permittivity (ε_r) and permittivity (μ_r) of the structure must be equal since the re-

flectivity is given by following relation:

$$r = (1 - \sqrt{\mu_r \varepsilon_r}) / (1 + \sqrt{\mu_r \varepsilon_r})) \tag{1.18}$$

By altering the dimensions of the metamaterial unit cell, one can suitably obtain equal values of (μ_r) and (ε_r) . When the values of μ_r and ε_r becomes equal, the input impedance of the structure becomes equal to free space impedance i.e. 377 Ω , since,

$$Z = \sqrt{\frac{\mu_0 \mu_r}{\varepsilon_0 \varepsilon_r}} \tag{1.19}$$

Therefore, impedance matching takes place between the free space and the absorber structure due to which wave does not reflect back from the surface of absorber. Thus, to obtain a near-perfect absorption, one expects to obtain impedance matching condition in which case the effective permittivity and permeability are required to be equal. However, such requirement is not met by any of the available natural material, therefore, artificially engineered structures also referred to as metamaterials are needed to be considered. Using metamaterials, one can artificially alter the electromagnetic properties of the wave by changing the characteristics of the structure in terms of the macroscopic parameters such as permittivity and permeability just by manipulating the dimensions and size of the metamaterial unit cells.

1.4.5 Metamaterial as cloaks

A cloak has the property to deflect the microwave beams such that they flow around a object with minimum distortion, due to which it appear almost as if there was nothing at all [8]. Metamaterials form the basis for attempt to builds a practical cloaking device. Cloaking can be achieved by cancellation of the electric and magnetic field generated by an object or by guiding the electromagnet wave around the object which means transforming the coordinate system in such a way that electromagnetic field inside the hollow cloak will be zero which results in disappearance of the area inside the shell.

1.4.6 Metamaterial as sensor

Metamaterials enables the significant enhancement of the resolution as well as sensitivity of the sensors [9]. Metamaterial sensors are used in biomedical, agriculture, etc. In agriculture, the sensors are based on resonant material and to gain better sensitivity they employ split ring resonators (SRR) type structures.

1.4.7 Metamaterial as Phase compensator

Phase compensator [10] is an important application of metamaterials which can be constructed by placing a DPS (double positive) slab followed by a DNG (double negative) slab. When the wave passes through a DPS slab having positive phase shift and then a DNG slab having opposite phase, the resultant phase of the wave that exit the DNG slab has the total phase difference equal to zero.

1.5 OTHER TERMINOLOGIES RELATED TO METAMATERIALS

1.5.1 Backward waves

A complex signal is composed of two or more frequency components. The carrier wave travels with the phase velocity (v_p) , whereas the envelope i.e. wave shape travels with group velocity (v_g) . In dispersive medium, velocities of carrier and envelope are different. Depending on nature of dispersion waves can be forward wave or backward wave. If medium has normal dispersion i.e. v_p and v_g are in same direction called the forward wave. However, in case of the anomalous dispersive medium, v_p and v_g are in the opposite directions forming backward wave. Thus, backward waves are simply a normal phenomenon that can occur with dispersive propagation.

Fig. 1.6(a) and (b) show the transmission line equivalents of forward and backward supporting waves respectively. Forward wave line, as shown in Fig. 1.6(a) has series inductance and shunt capacitance, but no resistive losses, due to either a series resistance or a shunt

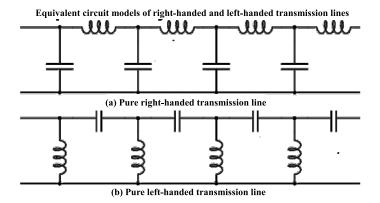


Figure 1.6: (a) Forward wave supporting RH transmission line (b) Backward wave supporting LH transmission line

conductance. It represents a low pass filter type LC line. Here, $Z=j\omega L$ and $Y=j\omega C$. since, $\gamma=j\beta=\pm\sqrt{ZY}, \ \beta=\omega\sqrt{LC}$. When ω is plotted as a function of β , it is a straight line of constant slope as shown in Fig.1.7(a).

$$v_p = \omega/\beta = 1/\sqrt{(LC)} \tag{1.20}$$

$$v_g = d\omega/d\beta = \omega/\beta = 1/\sqrt{(LC)}$$
 (1.21)

so $v_p = v_g$, representing forward wave.

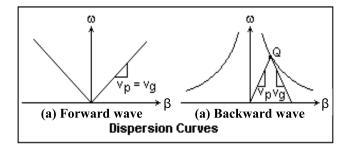


Figure 1.7: Dispersion diagram (a) Forward wave line (b) Backward wave line

Fig. 1.6(b) shows a backward wave supporting line. It is a high pass line consisting

of series capacitance and shunt inductance. Here, Z=1/j ω C and Y=1/j ω L. since, $\gamma = j\beta = \pm \sqrt{ZY}$, $\beta = 1/\omega \sqrt{LC}$. This gives the dispersion relation of backward wave supporting line.

$$v_p = \omega/\beta = \omega^2 \sqrt{(LC)} \tag{1.22}$$

$$v_g = d\omega/d\beta = -\omega^2 \sqrt{(LC)}$$
 (1.23)

Thus, phase and group velocity are in opposite direction to each other i.e. $v_p = -v_g$. This kind of waves are called backward waves. The dispersion relation of backward wave supporting line is plotted in the Fig.1.7 (b). The phase velocity is given by the slope of the line from the origin to a point on the dispersion curve, while the group velocity is given by the slope of a tangent to the dispersion curve. If the dispersion curve has only tangents in the same direction as the radius from the origin, then the phase and group velocities are in the same direction, and all the waves are forward. If the slope of the tangents are opposite, then there are backward waves.

1.5.2 Electromagnetic band gap structures

The unloaded planar lines support the continuous spectrum of wave motion; whereas the reactively loaded 1D periodic lines, also reactively loaded 2D periodic surfaces, exhibit discrete spectrum of wave motion by means of alternate passband - stopband phenomena. The stopband frequency region inhibits the wave propagation; thus creating the electromagnetic frequency band - gap. So the periodic structures are called the electromagnetic band - gap (EBG) structures. These are also sometimes called as the photonic band - gap (PBG) structures, using the terminology from optics. The periodic lines and surfaces, also known as the artificial lines and artificial surfaces, support the Bloch wave propagation. The EBG surface has the following interesting features:

1. Creation of alternate passband - stopband in otherwise a continuous RF spectrum that is also useful for the development of filters and other components.

- Suppression of the surface waves on the planar surface and creation of the high impedance
 or artificial magnetic conductor i.e. AMC surfaces (AMC) to improve the performances
 of the planar antennas.
- 3. Supporting the slow waves propagation. It is useful to develop compact, i.e. miniaturized, microwave devices.
- 4. Supporting the fast waves propagation leading to Cherenkov type radiation. It is useful to design the leaky wave antenna.
- Supporting backward waves propagation. It helps to develop transmission line base metamaterials.
- 6. Creation of the frequency selective surfaces (FSS) used in the antenna technology.

1.6 MOTIVATION

As the demand for advanced wireless communication has exploded, the requirement of novel highly efficient and miniaturized devices has increased in the areas like satellite communication, wireless telecommunication, spacecraft, aircraft etc. Conventional devices offer various challenges in terms of large size, low bandwidth, tedious installation, etc. Different methods were used to overcome these challenges but the come along with compromise on other properties like efficiency, gain, radiation performance, complex designing etc.

Metamaterial are novel structure that work based on manipulating the electromagnetic waves on the structure by changing the basic properties of the structure such as permittivity and permeability. **Metamaterial is an active area of research due to their exceptional properties beyond the scope of conventional structures.** By properly designing and optimizing their size, geometry and dimension, they can provide negative values of permittivity and permeability over a certain frequency range which is not found in nature, thus, extending the range of achievable effective permittivity and permeability values. Therefore, the use of

metamaterials will broaden the use of a device to various applications and also open up gates for new research objectives.

Use of metamaterials or 'artificial dielectric' to overcome the drawbacks of conventional structures is a wide area of research. They are an effective way to provide large bandwidth, miniaturization, ease of fabrication and installation without compromising the efficiency and gain of the device. Therefore, the present research is based on developing and utilizing such structures in improving the performance of conventional devices.

1.7 CHALLENGES IN DESIGN

- 1. Metamaterials are a basis for further miniaturization of microwave devices, with efficient power and acceptable bandwidth.
- 2. Using metamaterials in design of antennas is an emerging research area. A lot of work has been done in the past to improve the gain and efficiency of the antenna using metamaterials but at the cost of size so further improvements can be made.
- 3. Self-tuning property of a meta-material can be utilized to achieve high-fidelity beam steering and minimize side-lobe generation. This is critical for the emerging technologies of portable communications technologies associated with metamaterial.
- 4. Metamaterials can be researched upon many exciting configurations such as tunable reflectors, reconfigurable absorbers, superlenses etc.
- 5. Metamaterials can be used in modelling of filters with high rejection level in the stop band.
- 6. Extraction of lumped parameters and modelling of devices with the help of circuit parameters has been quite an issue and most of the literature follow hit and trial approach.
- 7. Use of metamaterials in achieving the so called "perfect absorption" is an active area of research.

- 8. Demand for achieving multiple band operation in a single device can be fulfilled using proper modelling techniques. Scaling metamaterial unit cells is quite useful to excite a completely different resonating frequency..
- 9. Multiple metamaterial cells can be incorporated on the multiple bends of a meandered line antenna in order to achieve higher efficiency, radiation resistance and bandwidth.
- 10. Metamaterials can be used to minimize the mutual coupling between antennas when used as antenna array in multiple input multiple output systems (MIMO). Lot of work has been done in this area, however, use of metamaterial absorbers for mutual coupling reduction have not been explored much.

1.8 RESEARCH PROBLEM STATEMENT

The major objectives of present research are listed below:

- 1. To perform an in-depth analysis of the theory and properties along with equivalent circuit models of novel metamaterial structures.
- 2. To perform a detailed analysis of various metamaterial structures available in literature and study their characteristics and the material property enhancement provided by them.
- 3. To realize and study different characteristics of novel metamaterial based devices that could be integrated within modern and future communication systems using suitable design tools such as High frequency structural simulator (HFSS) or Computer simulation Technology (CST) microwave studio.
- 4. To design highly efficient and miniaturized devices using metamaterials for optimum operation in various wireless communication applications.
- 5. Use of metamaterial absorbers for mutual coupling reduction in MIMO antennas.

6. To perform a comparative analysis of devices with and without metamaterials and check for the improvement in properties of a metamaterial based device with respect to the conventional device.

1.9 THESIS ORGANISATION

This thesis presents design and analysis of the metamaterial based microwave components i.e antenna, filters and absorbers. The organisation of thesis is summarized as follows.

In chapter one, introduction of the thesis is presented. This chapter gives a brief introduction to metamaterials and describes their basic theory of operation along with their areas of application and advantages of using them. This chapter also provides a brief review of the relevant work done by various researchers in the respective areas of application.

In chapter two, the latest work done in the areas of metamaterial based antennas, filters and absorbers is discussed.

In chapter three, a (CPW)-fed metamaterial inspired dual band microstrip antenna is presented for WLAN application. A triangular split ring resonator (TSRR) is used along with an open ended stub to achieve the dual band characteristics. The metamaterial characteristics of the proposed TSRR are observed and it is shown that the dual band achieved by the antenna is due to the metamaterial characteristics of the TSRR. The antenna is practically fabricated and tested to show good agreement with the simulated results.

In chapter four, the design of two metmaterial based filters is discussed. The first one is a low-profile Band Stop Filter (BSF) designed using Complimentary Split Ring Resonator (CSRR) on the ground plane and microstrip transmission line on the top. A methodology for equivalent circuit extraction is also presented which is validated in further sections by extracting equivalent circuits of other filters presented in literature. Moreover, a comparison based study is also presented to help the user choose the optimum configuration for desired specification. The second one is a Band Pass Filter (BPF) based on balanced Dual Composite Right/Left Handed (D-CRLH) Transmission Line (TL). A bandwidth enhancement technique

is also discussed in this case.

In chapter five, design of a novel multiband metamaterial absorber is presented and discussed. Multiple geometries are used within a compact dimension (one within the other), each geometry is either a single resonant structure or multi resonant structure, that combinedly resulted in a penta-band response. The structure is ultra thin and exhibits polarization independence as well as wide-angle absorption. Further, a simple closed meander line shaped metamaterial absorber is also presented operating at 3.5 GHz which is also analysed using equivalent circuit.

In chapter six, the use of metamaterial absorber (MA) to achieve high isolation between two patch antennas in a 2-element MIMO system is presented. The antennas as well as the absorber structure are designed to operating at 5.5 GHz resonant frequency useful for WiMAX application.

In chapter seven, conclusions drawn from the simulation, experimental and theoretical investigations are discussed. Some improvements that can be applicable in the proposed antenna designs are suggested as well as some recommendations about future work that can be done in the area is presented.

1.10 SUMMARY

This chapter begins with introduction of metamaterials. Subsequently, it lays insight into the evolution of metamaterials in the last decades. Further, the electromagnetic properties displayed by the absorbers are discussed and the advantages and applications of the metamaterials are illustrated. Brief emphasis is laid on the motivation of the present research work carried out. Problem statement and thesis organization is presented in the subsequent sections. To sum up, this chapter highlights the research work carried out in this thesis, further a literature review of the past work is carried out in the next chapter.

CHAPTER 2

LITERATURE REVIEW

Contents of this chapter are published as:

- 1. **Priyanka Garg** and Priyanka Jain, "Metamaterial-based Patch Antennas-Review" *Advances in System Optimization and Control*, vol. 509, pp 65-81, 2019.
- Priyanka Garg, Shruti Awasthi and Priyanka Jain "A Survey of Microwave Bandpass
 Filter Using Coupled Line Resonator Research Design and Development", Proceeding
 of International Conference on Sustainable Energy, Electronics and Computing Systems
 (SEEMS), October 27-28, 2018.
- Priyanka Garg and Priyanka Jain, "A Review of Multiband Metamaterial Absorbers" presented in National Conference on Microwave Absorbing Materials (VAMMAM-2020), Aug 23-24, 2020, Roorkee, India.

Antennas, filters and absorbers are the most basic microwave components that form an important part of any microwave system. Antennas and filters are the basic components of any communication system whereas, absorbers are necessary for electromagnetic compatibility (EMC) and electromagnetic interference (EMI) problems. Therefore, present work deals with understanding, analysing, and improving the properties of these components using metamaterials. In this chapter a brief review of the work done in these areas in last few years is presented.

2.1 ANTENNAS

There has been numerous advancements in this area since its inception. The most recent advancement are discussed below on the basis of the type of metamaterial unit cell they have utilized.

Epsilon negative metamaterials ($\varepsilon < 0$)

Epsilon negative (ENG) metamaterials are the materials having permittivity less than zero as well as permeability more than zero (ε < 0, μ > 0). Many plasmas display these characteristics in certain frequency ranges. The first known structure that gave ε -negative behavior is the one having infinitely long parallel thin metal wires, connected in square matrix form and are embedded in a dielectric medium (Fig. 2.1(a)) [2]. Few years later in 2004 [11], complementary split ring resonators (CSRRs), shown in Fig 2.1(b), have been proven to exhibit negative permittivity. Now, CSRR structures are being used for several applications like mutual coupling reduction [12], beam steering [4], size reduction [13, 14] and many more. Fig. 2.1(c) shows a double CSRR-loaded antenna which can be used for both positive and negative beam steering [4] minimize antenna size and improve bandwidth, complementary split-ring resonators (given in Fig. 2.1(d)) is placed horizontally between the bottom ground plane and the top patch [14]. An interdigital capacitor on the top side, as shown in Fig 2.1(e), with a complementary split-ring resonator (CSRR) slot on the bottom ground plane is presented in [15] for

mode hybridization. It also provides 55% patch size reduction as compared to a conventional patch antenna. More recently, a slot combined complementary split ring resonators (SC-SRR), shown in Fig 2.1(f), offering ε -negative behavior is also introduced in [12] to minimize mutual coupling between two elements of densely packed antenna array. The SC-SRR structure is placed in middle of the two patches to reduce mutual coupling with comparatively small separation distance. Other techniques employing EBG for coupling suppression are affected either by complicated fabrication process or by large antenna separation distance [16].

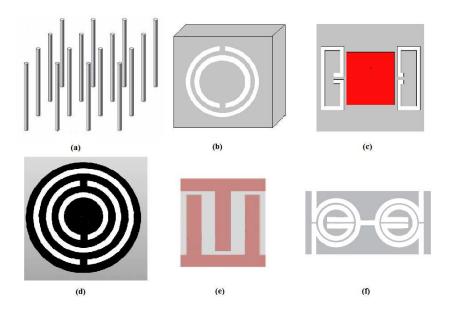


Figure 2.1: Structures offering -negative behaviour.

Mu-negative metamaterials (μ < 0)

 μ -negative (MNG) materials have permittivity greater than zero and permeability less than zero ($\varepsilon > 0$, $\mu < 0$). Some gyrotropic material presents these characteristic in certain frequency ranges. The first μ -negative metamaterial introduced was split ring resonator (SRR). Due to the presence of artificial magnetic dipole moments provided by ring resonator, SRR structure possesses a magnetic response despite the fact that it does not include magnetic conducting materials. Various SRR structures are presented in [5, 17–21], used for different

applications and property enhancement.

The SRR is a well known metamaterial unit structure; however, conventional planar SRRs have a drawback of narrow resonance band and require large dimension at low frequency. In order to resolve this problem, a compact nested tri-dimensional SRR is presented in high-permittivity low temperature co-fired ceramic (LTCC) medium [18]. Fig. 2.2(a) shows the tri-dimensional SRRs unit cell used for enhancement of gain. It provides an increase in gain of antenna to 6.93 dBi from 5.37 dBi compared to conventional antenna but with a compromise on substrate losses also making the fabrication process more tedious. An alternative approach is introduced in [19] by employing composite multi-band resonators where bandwidth of MNG could be enhanced with easier fabrication approach. It gave a comparative analysis of different SRRs and found that co-directional SRR (Fig. 2.2(b)) is the best choice to reduce mutual-coupling while taking into account different inner-ring rotation angles. Another planar antenna is introduced in [17], which presents a row of nine SRRs (basic unit cell shown in Fig. 2.2(c)) kind of structure, embedded on lower section of antenna. It provides about 1/3rd size reduction compared to conventional antenna with the same impedance bandwidth characteristics.

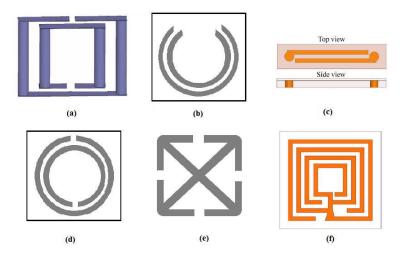


Figure 2.2: Various available SRR structures.

SRR metamaterial also have filtering characteristics which can be used to reduce surface waves. In [5], an SRR, as shown in Fig. 2.2(d), is presented for band reject filter application. It was observed by Gupta et. al. [5], as the number of SRRs increases; the rejection level in the stop band of the filter also increases. Another application of planar SRR structures is emerging in THz frequencies [20]. Since, using simple dielectric substrate leads to shock waves at air substrate inter-face, SRR metamaterials provide an effective way to direct the radiations from surface to free space. By using SRRs-CS (cross-shaped) substrate, as shown in Fig. 2.2(e), the gain enhancement of 6.24 dB as compared to 5.15 dB for the single SRR substrate is obtained in [20]. SRRs can also exhibit circular polarization property. A modified square split ring resonator (MSSRR) to show circular polarization is presented in [21]. MSSRR unit cell (Fig. 2.2(f)) composed of thin strips in which each of them produce negative refraction index.

Other than SRRs, the complementary electric inductive capacitive (CELC) structure, which is a dual counterpart of the electric inductive-capacitive resonator (ELC), has been known to deliver a resonant magnetic response i.e., negative magnetic permeability in the proximity of resonance [22]. [23] Demonstrates the complementary meander line (CML), as shown in Fig. 2.3(a) as a typical CELC structure. It has very low cross polarization and quite high radiation efficiency. Another CELC structure is demonstrated in [24], which is a fractal based hilbert-shaped complementary electric inductive capacitive resonator (HCELC), shown in Fig. 2.3(b). It helps in reducing mutual coupling more than 9.7 dB. Also, a slot-loaded ELC on the ground plane (Fig. 2.3(c)) is presented in [25] to offer a peak realized gain of 2.63 dB and efficiency of 86 %.

Double negative metamaterials ($\varepsilon < 0, \mu < 0$)

Double negative indexed materials are having both permittivity and permeability less than zero $(\varepsilon < 0, \mu < 0)$. This DNG class of materials is artificially tailored structures. These materials are not available in nature. The first experimental DNG structure consists of thin wires and SRRs, introduced by team UCSD (University of California, San Diego) [26], as shown in Fig.

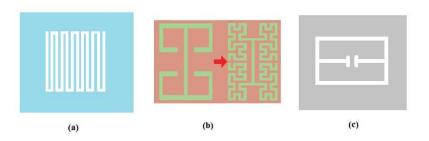


Figure 2.3: Different CELC structures.

2.4(a).

Mutual coupling between antennas can be reduced by using DNG structures in an antenna array. The use of conventional metamaterial structures i.e. thin wire and SRR involves bulky formations or multilayer structures. Such structures are difficult to miniaturize and less costefficient, so a wire loaded spiral resonators (SR), shown in Fig. 2.4(b) is introduced in [27] to reduce mutual coupling in an efficient manner. Using this, the mutual coupling of better than -28 dB is achieved. Another disadvantage of SRR based metamarterial is that the structural rotation influences the properties of these unit cells. This drawback has been overcome by cross type structures [28]. Further, Jerusalem Cross (JC) structures have been represented as replacement of SRR in [29]. Idea of JCs has been implemented through 3×3 array of crisscross structure to enhance gain (achieved gain =4.61 dB) and bandwidth (improved by 86.66% compared to conventional antenna) of antenna, shown in Fig. 2.4(c) [30].

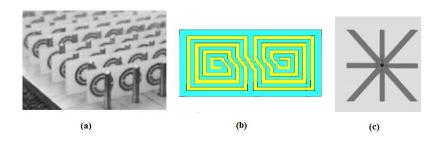


Figure 2.4: SRR structures for reduction of mutual coupling.

DNG structures can be used for antenna miniaturization as well. Miniaturization of antenna is done in [31], by partially loading metamaterial ring into an annular ring patch resonator, shown in Fig 2.5(a). It was demonstrated that the resonant frequency can be made as small as desired by adjusting the width of metamaterial ring. To construct a DNG metamaterial, modified split ring resonators (MSRRs) and metal strips are used in [32], shown in Fig. 2.5(b). Physical dimensions reduction from 0.5λ to 0.17λ and the bandwidth expansion to 17.56% are achieved through DNG filling.

Various other structures are also available for bandwidth enhancement [33–35]. The metamaterial unit cell made of meander lines (Fig. 2.5(c)) showing both permittivity and permeability negative simultaneously is presented [33] providing compactness and improved bandwidth of 600 MHz with 23.81% fractional bandwidth. A superstrate of double H-shaped metamaterial structure (Fig. 2.5(d)) is also used for bandwidth enhancement [34] giving efficiency improvement from 57.3% to 80.2% and bandwidth improvement from 70 to 220 MHz. A fishnet based metamaterial unit cell [35], shown in Fig. 2.5(e) is another DNG unit cell used for bandwidth improvement (8.2% bandwidth enhancement).

Most of the structures use either square or circular geometry. Use of triangular split ring resonator (Fig. 2.5(f)) is quite rare which is presented in [36], in which the cantilever MEMS switches are kept along the arms of the triangle to make splits. When the switch is in ON state it offers DNG behavior. Triangular structures are more compact compared to the circular and square geometries. These structures can be easily coupled side-by-side and have axial symmetry.

Various DNG structures are developed by combining two structures having SNG behavior independently [37–39]. One MSRR between two pairs of capacitance loaded strips (CLSs), shown in Fig. 2.6(a), is demonstrated in [37]. Here, MSRR exhibits response like magnetic material and produces negative permittivity, while the CLS exhibits response like strong dielectric and produces the negative permeability. Similarly, [38] demonstrates the effect of combining the use of capacitive gap on top substrate and CSRR on the bottom ground plane

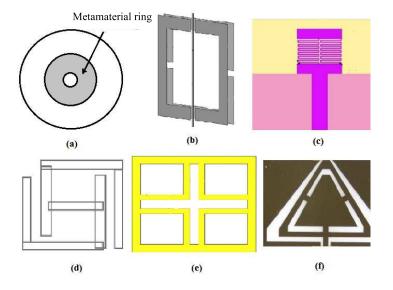


Figure 2.5: Variants of DNG structures.

(Fig. 2.6(b)). The double-layered CSRRs provide negative permittivities, whereas, in the longitudinal direction, capacitive gap exhibits the negative permeabilities, producing a DNG structure. The structure provided continuous frequency-scanning capabilities from backward 29° to forward 72°. In [39], a novel DNG structure was developed by combining CSSRR, offering negative permittivity, and CELC cells, offering negative permeability (Fig. 2.6(c)). It provides band pass filter characteristics with good upper band skirt performance.

This section discussed briefly the work done on metamaterial based antennas. Now, in the coming section, the literature review of metamaterial based filters is presented.

2.2 FILTERS

Microwave filter design is an important area of research from the very beginning of microwave engineering. Basically, filters are divided into four catagories: highpass, lowpass, bandpass, and bandstop. Bandpass filters with low insertion losses are essential components of all kinds of modern communication devices because of both their band selecting an image and spurious rejecting capability. Microwave Filters are passive, two-port, reciprocal, linear device that are

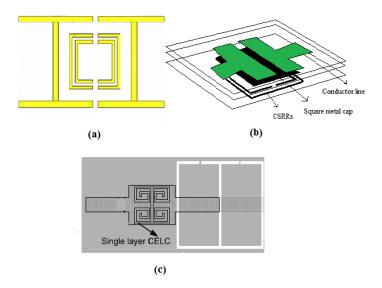


Figure 2.6: DNG structures developed by combining SNG structures.

used to allow the transmission of a range of signal frequencies while rejecting the unwanted frequencies, thus providing control over frequency response. Filters are used to protect the receivers from interference with the signals outside the desired band and to confine the radiation from high-power transmitters within assigned frequency range. To satisfy the specifications of the modern communication system, designing of microwave and millimeter-wave devices requirement of accuracy and high-performance has increased.

Before discussing the advancement in metamaterial based filters let us discuss various filter metrics.

2.2.1 Filter Metrics:

This section describes the various parameters required for designing a Bandpass Filter, which is as follows:

A) Insertion Loss: Insertion loss measures loss incurred by insertion of filter between input/output ports which is represented mathematically as,

$$Insertionloss(dB) = 10\log(P_{lr}) \tag{2.1}$$

Where P_{lr} is the power loss ratio which is the inverse of the filter transfer function normalized to the zero frequency value of gain. It measures the power reduction due to impedance mismatch. Within the filter passband, the insertion losses are less than 3dB irrespective of the order of filter in Butterworth filter whereas Insertion losses are sensitive to passband ripples in Chebyshev. Chebyshev insertion loss is less dramatic than the Butterworth filter within the passband.

b) Return Loss: It measures the relative amount of power reflected by an input signal. Mathematically,

$$Returnloss(dB) = -10\log\left[\frac{VSWR + 1}{VSWR - 1}\right]$$
 (2.2)

where VSWR is the voltage standing wave ratio. In a perfect transmission line, Return Loss is infinite. In a perfectly reflective circuit, it is zero. c) Bandwidth: The width of the passband expressed as the difference between lower and higher relative 3dB attenuation points. d) Quality Factor: In a bandpass filter, loaded Q" is used to define the ratio of center frequency to 3dB bandwidth expressed as

$$LoadedQ = \frac{CenterFrequency}{3 - dBbandwidth}$$
 (2.3)

2.2.2 Metamaterial inspired filters

Metamaterial inspired filters generally consists of one or more than one unit cells designed on the top coupled along the sides of a microstrip transmission line, metamaterial loaded on the TL as a defected microstrip transmission line (DML) or as a defected ground structure (DGS). Various coplanar waveguide (CPW) configurations of the filters have also been proposed. These are analysed as a composite left/right handed (CRLH) transmission line (TL), since the unit cell loaded on the transmission line introduces an LC tank circuit either in series or in shunt with the conventional right handed transmission line.

Composite left/right handed (CRLH) metamaterial

Caloz and Itoh *et. al.* [40] introduced the concept of metamaterial transmission lines (TL) in 2002. These TL metamaterials typically exhibit a LH band at lower frequencies and a right-handed (RH) band at higher frequencies and are termed as Composite Right/Left Handed Transmission lines (CRLH TL). CRLH metamaterials are more general form of metamaterials. The model for a loss-less CRLH transmission line (TL) is shown in Fig 2.7. It consist of a per-unit length impedance $Z(\Omega/m)$ constituted by RH per unit length inductance L_R (H/m) in series with LH times-unit length capacitance C_L (F-m) followed by a per unit length admittance Y (S/m) constituting RH per unit length capacitance C_R (F/m) in parallel with a LH times-unit length inductance L_L (H-m). Value of impedance Z and admittance Y are given in 2.4.

$$Z = j(\omega L_R - 1/\omega C_L) \tag{2.4}$$

$$Y = j(\omega C_R - 1/\omega L_L) \tag{2.5}$$

If LH immittances are zero for $C_L = \infty$ and $L_L = \infty$, only RH immittances remain and the

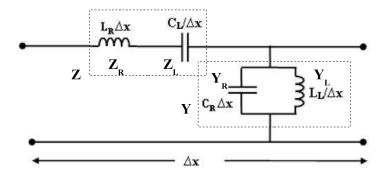


Figure 2.7: Equivalent circuit model for the ideal CRLH TL

model reduces to conventional RH TL model. In contrast, if RH immittances are zero for $C_R = 0$ and $L_R = 0$, only LH immittances remain and the model reduces to LH TL model. LH TL

cannot exist physically because parasitic series inductance and shunt capacitance effect will unavoidably occur due to current flowing in the metallization and voltage gradients developing between metal patterns of the trace and ground plane.

Metamaterial coupled TL filter

Such type of filters consists of a transmission line on top of the substrate with one or more metamaterial unit cells aligned on either or both the sides of the TL. [41] demonstrates a cut band filter having SRRs etched on both the sides of the transmission line to achieve stopband response. Fig. 2.8(a) shows the filter configuration with the stopband response obtained by the filter. It was found that on increasing the number of SRRs on both the sides, the sharpness of the band increases. In [42], multiple hexagonal mushroom resonators are placed on one side of the transmission line to obtain dual-stopband characteristics (Fig. 2.8(b)). Further, to achieve tunability, varactor diodes are introduced between the TL and SRR in [43], as shown in Fig. 2.8(c). On increasing the capacitance of the varactor diode, the resonant frequency is shifted from 4.17 GHz with a 10 dB bandwidth of 3.6% to 3.73 GHz with a 10 dB-bandwidth of 14.4% also increasing the rejection level from 21 dB to 48 dB. A dual-band bandpass filter is constructed by loaded open loop resonators (OLR) [44]. The feed line is grounded using two via holes to convert the bandstop characteristics to bandpass response, shown in Fig. 2.8(d). Fig. 2.8 (e) shows single metamaterial unit cell placed on one side of the TL to obtain passband with high Q-factor [45]. The unit cell used is a μ - near zero metamaterial designed using an interdigital hair-pin resonator and meanderline.

Defected Microstrip line

In these structures, one or more metamaterial unit cells are loaded in the middle of conventional microstrip line. The unit cell is either connected to the 50Ω line or coupled to the line from both sides. Fig. 2.9 shows various configurations of such filters. In [46], Fan *et. al* presented two electrically coupled SRRs, each fed by a $50-\Omega$ transmission line to exhibit dual

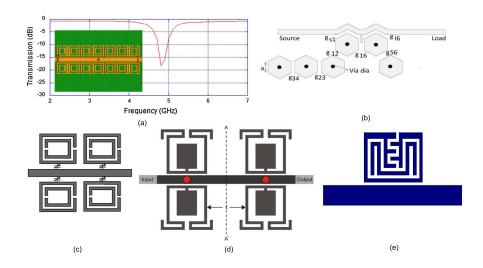


Figure 2.8: Metamaterial coupled TL filter

band bandpass filter characteristics. A 0° feeding structure is used to improve the selectivity of the filter, shown in Fig. 2.9(a). A broadside coupled triple split-ring resonator, exhibiting LHM characteristics is placed between two $\lambda_g/4$ transmission lines to achieve bandpass filter response, as shown in Fig. 2.9(b) [47]. The series $\lambda_g/4$ TL was then replaced by an equivalent T-shaped line for second harmonic reduction. Fig. 2.9(c) shows a wideband bandpass filter with excellent band rejection levels [48]. The interdigital capacitor and the meander line forms a series LC resonator whereas the open complementary split ring resonator (OCSRR) forms the parallel LC tank circuit. The parasitic capacitances introduced by both the geometries result in two additional resonances, leading to a fractional bandwidth of 94%. Another bandpass filter is designed using a shorted spiral structure, shown in Fig. 2.9(d), which is an artificial magnetic resonator [49]. A cascaded quadruplet of the shorted spiral structure is used which resulted in 80% size reduction compared to the conventional open loop resonator. Fig. 2.9(e) shows a CRLH-TL based bandpass filter [50]. A dielectric slot is introduced at the bottom surface, which caused frequency tuning based on the position of the slot with respect to the CRLH-TL.

In [51] compact bandpass filter is realised using two metamaterial inspired resonator place in between two $\lambda_g/4$ transmission lines (Fig. 2.9(f)). Such structure do not require any match-

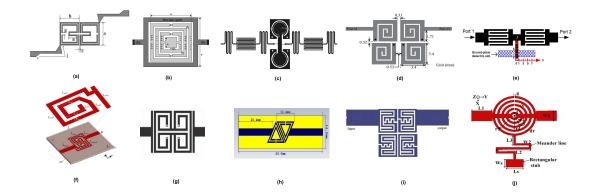


Figure 2.9: Defected Microstrip line filter

ing network thus reducing the physical size of the structure. Fig. 2.9(g) shows grounded spiral resonator to design compact, highly selective bandpass filter with high Q factor [52]. The reduced radiation losses and high Q factor are obtained using specific arrangement of the proposed grounded spiral geometry. In [53], two edge coupled dual triangular split ring resonators are used to obtain the passband characteristics (Fig. 2.9(h)) whereas in [54] a combination of hair-pin, inter-digital capacitor, and meander-line resonators is used to realise a bandpass filter (Fig. 2.9(i)). More recently, a wideband bandpass filter is designed using split circular rings and rectangular stub, as shown in Fig.2.9(j) [55]. The split circular rings provide series capacitance and a meander line along with a rectangular stub gives shunt inductance and capacitance. This structure provides a fractional bandwidth of 80.48%.

Defected Ground structure

In these filters, one or more metamaterial unit cells are etched out of the ground plane, thus calling it as a defected ground structure. In [56], Falcone *et. al* introduced a complementary split ring resonator (CSRR) which is a counter part of an SRR. It was proposed that a microstrip transmission line incorporated by CSRR on the ground plane shows bandstop characteristics, further, on loading the microstrip line with capacitive gaps, the bandstop behaviour switches to bandpass one. Fig. 2.10(a) shows an SRR etched out of the ground plane, this structure is termed as a complementary split ring resonator (CSRR). In [57], the CSRR shown

in Fig. 2.10(a) is placed on the bottom ground plane with a stepped impedance transmission line on the top to realize a sharp cutoff low pass filter (LPF). The CSRR's negative ε -property helps in improving the roll-off performance of the filter with no ripples. It also provides high selectivity of 32 dB/GHz and 16% smaller size compared to conventional LPF. Another LPF is realized by etching out a hilbert-shaped resonator (H-CRR) from the ground plane instead of a conventional CSRR, as shown in Fig. 2.10(b) [58]. By integrating the H-CRR with the TL, a substantial increase in the selectivity was observed. The fractal geometry leads to miniaturization of size as compared to conventional CSRR. In [59], both SRR and CSRR are used to achieve dual-band rejection characteristics. The SRRs are inductively coupled to the transmission line on top of the substrate while the CSRR is used as a DGS which is capacitively coupled to the transmission line, shown in Fig. 2.10(c). Fig. 2.10(d) presents a CRLH TL using capacitively loaded transmission line on top and a complementary spiral resonator on bottom [60]. This configuration yields high pass filter characteristics. Fig. 2.10(e) shows the top and bottom surfaces of an ultrawide band (UWB) bandpass filter with a highly selective band notch [61]. Three complementary two turns spiral resonator (CSR2) on the bottom are responsible to generate the desired stop band characteristics. Each CSR has different dimension due to which they provide three different resonances, which widens the bandwidth and enables sharp rejection skirt performance.

Various other DGS configurations have been investigated in order to improve the performance of filters with compact dimensions. Such as, in [62], a complementary moore curve fractal-shaped spiral resonator has been presented (Fig. 2.10(f)), which forms a CRLH TL and provides 49% size reduction as compared to other geometries. In [63], the CSRR is fed with parallel coupled feed line instead of the conventional series coupled line to design BPF (Fig. 2.10(g)), which lead to compact size and simpler design procedure compared to the conventional CSRR BPFs. Further, a complementary electric LC resonator (CELC) is investigated in [64], as shown in Fig. 2.10(h). The CELC is an ε -negative type of unit cell, it is further integrated with a short circuited stub which makes it an LH unit cell, providing a bandpass

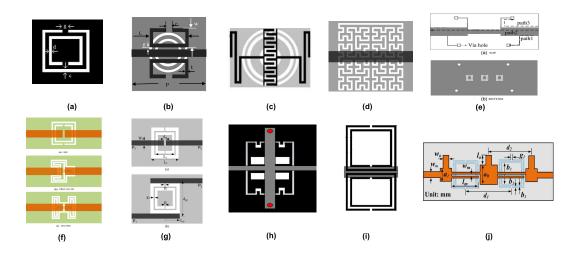


Figure 2.10: Defected Ground structures

filter response. In [65], a pairs of Coupled CSRRs are used to load the line instead of single CSRR (Fig. 2.10(i)), due to which dual transmission zeros are observed since, the use of two different CSRRs lead to a dual-band ENG metamaterial transmission line. Fig. 2.10(j) shows the design of a wide bandstop filter [66], the CSRRs are again used to improve the selectivity and improve the stop band bandwidth of the filter by introducing a transmission zero near the passband.

Coplanar Waveguide Filters

Martin et al. in 2003 [67] introduced a coplanar waveguide line coupled with SRRs and periodically loaded with narrow wires, as shown in Fig. 2.11(a). The SRRs provide negative permeability and the narrow wires provide essential negative permittivity, thus making it an LH medium which enables the left handed wave to propagate in the vicinity of resonant frequency. Various other configurations were also investigated later (Fig. 2.11). In [68], open split ring resonators (OSRR) and complementary OSRRs are used on each side of the CPW line, as shown in Fig. 2.11(b). This configuration provides passband with improved out-of-band response. Fig. 2.11(c) shows another configuration that uses a combination of OSRR and OCSRR [69] to design a CRLH TL. In this case, OSRR is coupled to the microstrip

and OCSRR is coupled to CPW and it was concluded that its performance comparable to the CL-loaded approach. This idea was further extended to order-7 band pass filter with 53% bandwidth [70]. In [71], a combination of double series gaps and shunt strips are periodically loaded on the CPW line with SRR on the bottom (Fig. 2.11(d)). Double shunt strips provide LH media whereas series gaps provide RH media. It provides excellent out-of-band performance and better selectivity.

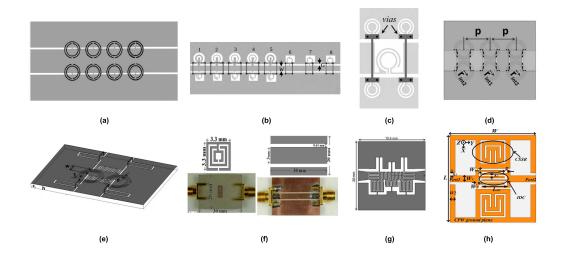


Figure 2.11: Coplanar Waveguide Filters

Fig. 2.11(e) shows a CPW line loaded with two SRR providing negative permeability, two wide shunt inductances (metallic strips) providing negative permittivity, two series capacitances (interdigital capacitors), and four shunt capacitances (implemented through openended stubs) which allow to control the left and right handed bands [72]. The structure forms a compact balanced CRLH TL to provide wideband bandpass filter response. [73] presents a modified SRR bent to form a closed loop, shown in Fig. 2.11(f). This geometry provides various advantages over conventional SRR such as distributed capacitance and inductance can be calculated accurately using simple TL theory, it enables tuning of distributed elements separately and only one dimension is needed to be controlled to tune the resonance frequency. In [74] a π -T generalised NRI TL is introduced. Fig. 2.11(g) shows a CPW filter based on the π -T TL which exhibits triple bandpass characteristics with only 1 dB insertion loss and 13

dB attenuation in the stop band. Fig. 2.11h shows a recently developed CPW based dual-band bandpass filter [75] which consist of a modified CSRR etched out off the CPW ground plane and an interdigital capacitor loaded on the microstrip line. Each of the geometry is responsible for one of the passbands.

Through the above survey it can be concluded that metamaterials can be combined with different configurations of the filters such as DGS, DML, CPW etc, according to the requirement of the users to fulfil given specifications. Further, in the next section, the review of different types of metamaterial based absorbers is presented.

2.3 ABSORBERS

Electromagnetic absorbers are used to restrict the transmission and reflection of electromagnetic wave from their surface within a certain frequency range. They are widely used in various applications such as radar cross section reduction of antennas, radome, EMI/EMC applications, antenna side lobe reduction, sensing and so on. Conventional electromagnetic absorbers like Salisbury screen and Jaumann absorbers are thick and bulky. Therefore metamaterial absorbers have been an active area of research in the past decade. They overcome the disadvantages of conventional absorbers by providing ultrathin thickness and near perfect absorption. Metamaterial absorbers are generally two dimensional metasurfaces consisting of $n \times n$ array of unit cells whose impedance is matched to the free space impedance by manipulating the dimensions of unit cell. When the wave strikes the surface of metamaterial absorber, the electric and magnetic resonances takes place at a particular range of frequency which leads to absorption of wave at that frequency. Since the introduction of first metamaterial based absorber in 2008 [7], various narroband, multiband and broadband absorbers have been reported in literature and investigated for polarization insensitivity and wide angle absorption.

2.3.1 Narrowband metamaterial absorber

Landy et. al. [7] introduced the first 'perfect metamaterial absorber' in 2008, shown in Fig. 2.12 (a). The structure consists of an Electric Ring Resonator (ERR) on the top and a cut wire on the bottom of an FR-4 substrate, providing an absorptivity of 96% at 11.65 GHz. As the wave strikes the surface of structure electric and magnetic resonances takes place at the 11.65 GHz. Electric resonance occurs due to the strong coupling of incident electric field on the structure in the form of dielectric losses and magnetic resonance occurs due to the anti-parallel currents flowing on the top and bottom surfaces of the structure, leading to a circulating current. It was observed that this cut wire design at the bottom leads to some amount of transmission which could be avoided by laminating the bottom surface completely with copper. An electric-field-coupled-LC (ELC) resonators with metal laminated ground plane is introduced in [76], shown in Fig. 2.12(b). It was observed to have zero transmission with minimum reflection and 96.7% absorptivity at 9.92 GHz. Later, various modifications of ELC resonator were investigated for narrowband and multiband applications [77, 78].

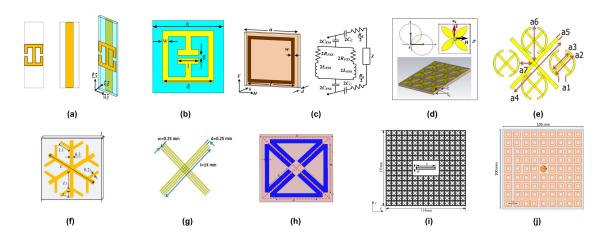


Figure 2.12: Narrowband metamaterial absorbers

A square loop is the simplest geometry used for absorption. Ghosh *et. al* [79] presented the analysis of an ultra thin square ring shaped metamaterial absorber using equivalent circuit model with the help of coupled line theory. Furthermore, various other geometries like flower

shaped, ring and cross wire resonator, snowflake [80] and metal wire strips were also designed (shown in Fig. 2.12(d-g)) where the absorptivity of more than 99% was observed at 13.2 GHz, 2.76 GHz, 11.28 GHz and 3.42 GHz respectively. In addition, all of them were reported to show polarization insensitivity along with wide angle absorbance. Another four-fold geometry was proposed in [81] to provide 99.6% absorptivity at the frequency of 8.65 GHz, shown in Fig. 2.12(h).

Metamaterial absorbers can be used for RCS reduction [82, 83] and sensing [9]. In [82] a cross shaped resonator is used for monostatic and bistatic RCS reduction of a waveguide slot antenna, whereas in [83], dual square ring structure is used for RCS reduction of circular patch antenna.

2.3.2 Multiband metamaterial absorber

Since the conventional absorbers like Salisbury screen and Jaumann become thick and bulky when they are required to perform absorption at multiple or broadband frequencies, therefore, metamaterial absorbers are used which can help in absorbing multiple frequencies within an ultrathin thickness. This is the reason metamaterial absorbers have gained extensive popularity among the scientific community. Various techniques are used to exhibit multi-frequency absorption, such as use of multiple resonant structures or scaled or rotated versions of the same geometry, use of layered design, use of different resonant structures in single geometry that resonate at different frequencies, use of multiple resonant structures and generation of higher order modes. The first two techniques lead to increased size of the unit cell. Therefore, use of different geometries in a single structure along with multiple resonant structures is preferred over other technique for multi-frequency absorption.

Fig. 2.13(a) shows a unit cell with different scaled versions of the flower shaped structure [84]. Each scaled version is operating at different frequency so providing four absorption peaks, however, the symmetry of the overall structure is lost. Therefore, these structures are polarization sensitive. To avoid this, [85, 86] presents two different geometries placed

alternatively (Fig. 2.13(b,c)). [85] provides dual band characteristics at 9.02 GHz and 11.85 GHz with absorptivity of 99.3% and 99.4% respectively. [86] provides triple band response with absorption peaks at 5.22 GHz, 7.44 GHz, 9.96 GHz, and 10.48 GHz with absorptivities of 97.1%, 91.3%, 98.3%, and 90.7%, respectively. In [87–89] 90° rotated versions of the same geometry is used to provide multiple absorption peaks (Fig. 2.13(d, e, f)). It was observed in [87] that electric and magnetic resonance arise at completely different frequency when the ELC structure is rotated by 90°.

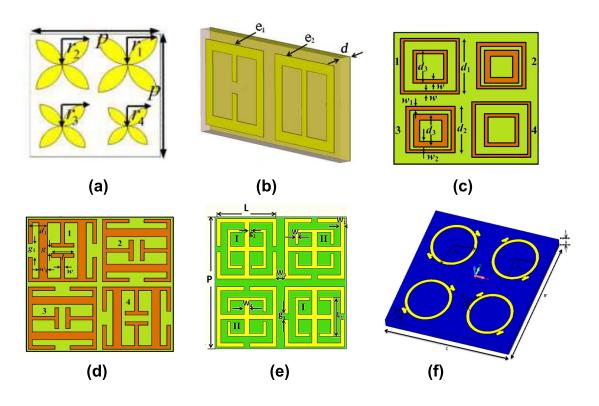


Figure 2.13: Unit cell with scaled versions of flower shape (a) Use of different resonant structures (b,c), Rotated versions of unit cell (d,e,f)

Use of multiple structures has the drawback of increasing the overall size. Which was reduced by using multiple scaled versions of a geometry within the same structure (smaller one within the bidder one), as shown in Fig. 2.14. In such cases, each scaled geometry resonate at different frequency, the smaller structure produced absorption at higher frequency and larger one at lower frequency. [90] and [91] presents three concentric circular rings and stars

(Fig. 2.14(a,b)) respectively producing three different resonant peaks. Whereas, in [92], two scaled square geometries (Fig. 2.14(c)) were used which resulted in dual band response. This techniques helps in size reduction of unit cell which was observed in earlier cases, however, it is difficult optimize the dimensions to avoid the mutual coupling among the adjacent scaled geometries. Therefore, multiple resonant structures are introduced.

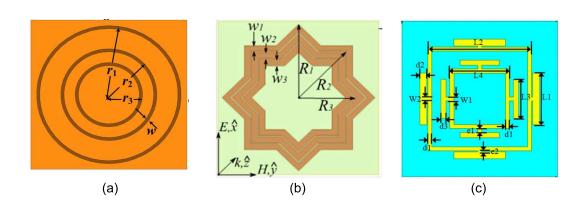


Figure 2.14: Scaled unit cells one within the other

Fig. 2.15 shows different multi-resonant structures i.e. single geometry exhibits absorption at multiple frequencies. Fig.2.15(a) [93] presents a tri-band absorber with absorption peaks at 3.07GHz, 5.65GHz, and 8.11GHz with absorption rates 99.87%, 99.98%, and 99.99%. In [94] and [95], a spiral resonator (Fig. 2.15(b)) and a snow-flake structure (Fig. 2.15(c)) respectively are used to exhibit triple band response whereas in [96], a Chinese coin shaped structure (Fig. 2.15(d)) is used to achieve penta-band response. Another structure to deliver penta-band response is investigated in [97], as shown in Fig. 2.15(e). It was designed to exhibit five absorption peaks at frequencies 3.52, 8.24, 9.69, 14.12, and 17.48 GHz with peak absorptivity values of 96.1%, 97.4%, 91.9%, 99.5%, and 98.8%, respectively. A dual band structure is presented in [98](Fig. 2.15(f)). These structures definitely are responsible for multiple absorption peaks within a compact unit cell dimension, however, individual tuning of each frequency is rather difficult.

In order to overcome this drawback, unit cells with combination of different geometries

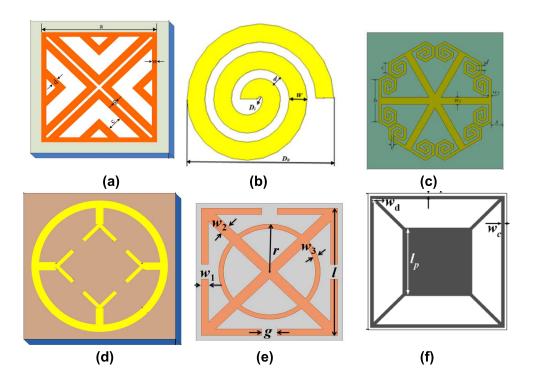


Figure 2.15: Multi resonant structures

(one inside the other) are used, such that individual geometry is responsible for each absorption peak, thus enabling tuning of each frequency by manipulating the dimensions of corresponding geometry. Fig. 2.16(a-e) shows some of these type of structures reported in literature. Fig. 2.16(a) also shows a combination of three geometries leading to the three absorption peaks [99]. In [100], an ELC resonator is combined with four square geometry (Fig. 2.16(b)) to exhibit three absorption peaks, one at 4.2 GHz which is due to the ELC, the second peak at 7 GHz is due to the four square structure, and the third peak arises due to coupling between the two structures. [101, 102] presents dual band metamaterial absorbers shown in Fig. 2.16(c,d) respectively. [101] presents dual band response using an ultra thin structure with a thickness of $\lambda_0/126$ at 9.5 GHz, offering neglegible degradation when applied to a curved surface. Such structures are prone to complexity once the number of absorption peaks are required to be increased, therefore, these structures can be combined with multiple resonant structures, shown in Fig. 2.16(f-j), with some trade off. Fig. 2.16(h) [103] shows a combination of three ge-

ometries conductive cross dipoles providing three absorption peaks, conductive cross dipoles loaded with SRR and conductive cross dipoles rotated by 45° each providing one absorption peaks, leading to a penta-band response.

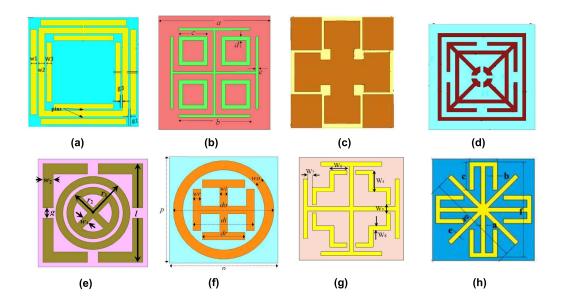


Figure 2.16: Unit cells with different resonant structures

2.3.3 Broadband Absorbers

Broadband absorbers operate on a wide range of frequencies. Till date various broadband absorbers have been proposed. Most popular techniques used for broadband absorption include the use of multi-layered structures, use of multiple scaled versions of same geometry on one unit cell, use of lumped elements and multi resonant structures. [104] presents a multi-layerd structure (Fig. 2.17(a)). It consists of three different loop type structures separated by dielectric layers of Rogers and top layer is covered with Teflon achieving more than 90% absorptivity for a bandwidth of 12.63 GHz. [105] presents vertically stacked metal-dielectric layers where each metallic patch is cross shaped (Fig. 2.17(b)) with different dimensions to achieve broadband response. Fig. 2.17(c) shows another layered structure where each layer consist of resistive sheets, enabling Ultra wide band (UWB) absorption [106]. However, the

thickness of these structures is beyond the practical limit and proper alignment of the layers is also difficult which leads to the demand of ultra thin mono-layered structures.

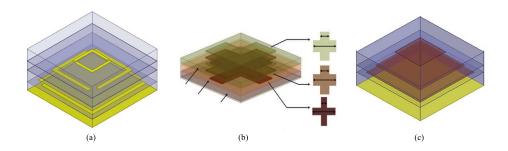


Figure 2.17: Unit cells with multi-layered structures

In [107] multiple square patches with different dimensions (Fig. 2.18(a)) are used in a unit cell such that the absorption peaks due to each geometry blend together to result in a broadband response. The thickness of this structure is only 0.4 mm. Another such approach to provide enhanced absorption band is presented in [108], where the unit cell comprises of 90° rotated versions of E-shaped geometry, shown in Fig. 2.18(b). Each rotated geometry results in a different absorption peak but close to the each other, resulting in enhanced bandwidth. In these structures the overall size of the unit cell increases, causing limitation in practical application. So to design compact size unit cells, lumped components are used. Fig. 2.18(c) shows a double octagonal rings loaded with eight lumped resistances [109]. The resistances used on the structure manipulate the electric and magnetic field at different frequencies causing a broadband response and the thickness is 3 mm, but the structure is polarization sensitive. [110] also shows design of another metamaterial broadband absorber based on fractal geometry using lumped resistors (Fig. 2.18(d)). It provides >90% absorptivity for 4-8.12 GHz frequency range and also offers polarization insensitivity by at an expense of 5 mm thickness. Various other such structures have been reported [111-113]. They result in compact geometry compared to the earlier case, however, the fabrication overhead increases due to mounting of the lumped components. Further, multiple resonant structures as shown in Fig. 2.18(e,f) [114,115] or scaled versions of same geometry (Fig. 2.18(g) [116]) are used, one within the other, to

design compact and ultra thin wideband absorbers.

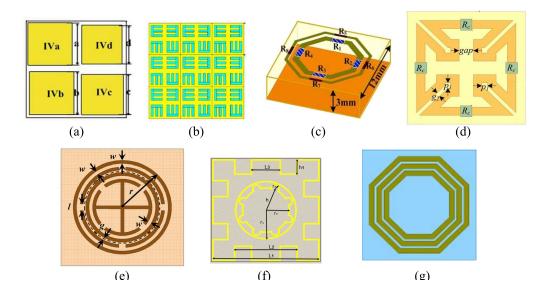


Figure 2.18: Unit cells with mono-layered structures

In this section different configurations of the metamaterial based absorbers is discussed along with their advantages and disadvantages. In the coming chapters different metamaterial based microwave components are designed and analysed.

CHAPTER 3

METAMATERIAL INSPIRED DUAL BAND ANTENNA FOR WLAN APPLICATION

Contents of this chapter are published as:

Priyanka Garg and Priyanka Jain, "Design and Analysis of a Metamaterial inspired dual band antenna for WLAN application" *International Journal of Microwave and Wireless Technologies*, vol. 11, no. 4, pp. 351-358, 2019.

With emerging technology of wireless communication, microstrip antennas have gained large interest due to their compact size, light weight, ease of fabrication and integration on small scale electronic devices. Using microstrip planar technology also provides an efficient way to achieve multiband operation on a single device which is very useful to access several wireless services, such as, WLAN, WiMAX, LTE etc., which are widely used in wireless communication devices. Various microstrip antennas are available in literature that offer dual band and triple band characteristics such as asymmetric M-shaped antenna [117], H-shaped slot antenna [118]. Defected ground structure (DGS) antennas are also presented for dual band application [119]. These conventional microstrip antennas offer several challenges in terms of miniaturization, multiple frequency operation, bandwidth enhancement, gain and efficiency improvement etc. This led to the emergence of artificially engineered structures called metamaterials which exhibit exclusive electromagnetic properties that are not found in nature. Such metamaterials can be utilised in planar technology to overcome various challenges of microstrip antennas.

Various authors have demonstrated the use of metamaterials in planar antennas for the purpose of antenna miniaturization, multi-band operation, gain and bandwidth improvement. A triple band monopole antenna is presented in [120], that uses single cell metamaterial loading along with DGS ground plane to achieve tri-band operation. Ref. [121] presented a metamaterial unit cell comprising an interdigital capacitor and a complementary split-ring resonator (CSRR) slot. This antenna offers wideband operation and high efficiency up to 96 %. Further, a metamaterial inspired patch antenna is presented for miniaturization [122]. To reduce antenna size and improve bandwidth, a complementary split-ring resonator (CSRR) is placed horizontally between the bottom ground plane and the top patch. However, size reduction after a certain limit led to reduction in radiation efficiency and fractional bandwidth which is undesirable. A compact antenna with enhanced bandwidth is presented in [123]. The size of antenna is reduced by using an epsilon negative transmission line (ENG TL). [124] also presented a metamaterial inspired antenna for GSM/UMTS/LTE/WLAN wireless communication

systems. The antenna shows a bandwidth enhancement of 40.2 % by using a resonant ring as compared to conventional antenna. Recently, the use of interdigital capacitor is presented in [125] to enhance bandwidth. By properly designing the interdigital capacitor, Q-factor of the resonant antenna can be reduced, thus, improving the bandwidth.

Metamaterials are also used for mutual coupling reduction in MIMO antennas such a closely spaced metamaterial MIMO antenna with high isolation is presented in [126]. A simple defected ground structure is used in between two antennas to limit the surface waves and provide mutual coupling better than -45 dB.

Most of the structures found in the literature consist of either circular or square geometries, using triangular geometry is quite rare. Triangular structure offer relatively compact size and easy side-by-side coupling. Therefore, in this chapter a dual band compact sized antenna utilizing triangular double split ring resonator is presented. The proposed antenna covers entire spectrum of WLAN (Wireless Local Area Network) bands. The operating bands for this technology is assigned by IEEE 802.11 are 2.4 GHz(2.4-2.484 GHz), 5.2/5.8 GHz (5.15-5.35 GHz/5.725-5.825 GHz). The proposed antenna operates on the following bands: 2.4-2.48 GHz and 4.7-6.04 GHz, thus, offering dual band characteristics to cover WLAN bands. Simulations are performed using ANSYS High frequency structure simulator (HFSS).

3.1 MATERIAL PARAMETER EXTRACTION

Fig 3.1 shows the schematic of proposed modified triangular split ring resonator unit cell. The proposed metamaterial unit cell is designed on FR-4 dielectric substrate having dielectric constant (ε_r) = 4.4 and loss tangent ($tan\delta$) = 0.02 with dimensions $16 \times 12 \times 1.6 \ mm^3$. The structure comprises a double triangular split ring resonator having splits on the opposite arms and an open ended stub connected at a distance of 0.8 mm below the outer ring. The width of each split ring is 0.9 mm with split gap of 1 mm. The average length of outer ring is 35.87 mm and that of inner ring is 19.03 mm. In order to extract the material parameters i.e, effective permittivity (ε), permeability (μ), refractive index (n) and wave impedance (z), the structure

is placed inside a waveguide medium (Fig. 3.1). The waveguide ports are assigned along the x-axis and excited by the electromagnetic wave along x-direction. The perfect electric (PEC) and perfect magnetic (PMC) boundaries are assigned to y-axis and z-axis respectively.

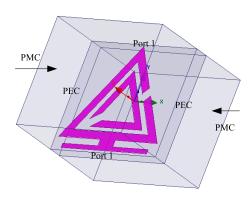


Figure 3.1: Simulation setup of proposed metamaterial unit cell.

Now, effective medium parameters are extracted from the simulated complex scattering parameters using the modified Nicolson-Ross-Weir (NRW) relations presented in [127]. Taking two arbitrary variables given by following equations:

$$V_1 = S_{21} + S_{11} \tag{3.1}$$

$$V_2 = S_{21} - S_{11} \tag{3.2}$$

Complex normalised wave impedance(z) can be obtained by following equations:

$$z = \sqrt{\frac{(1+S_{11})^2 - S_{21}^2}{(1-S_{11})^2 - S_{21}^2}}$$
 (3.3)

Now, permeability(μ_r), permittivity(ε_r) and refractive index(n) are obtained simply by us-

ing the equations given below:

$$\mu_r = \frac{2}{ikd} \cdot \frac{1 - V_2}{1 + V_2} \tag{3.4}$$

$$\mu_r = \frac{2}{jkd} \cdot \frac{1 - V_2}{1 + V_2}$$

$$\varepsilon_r = \frac{2}{jkd} \cdot \frac{1 - V_1}{1 + V_1}$$
(3.4)

$$\varepsilon = n/z \tag{3.6}$$

$$\mu = nz \tag{3.7}$$

Fig. 3.2 (a)-(c) shows the real part of extracted parameters i.e. permeability (μ_r) , permittivity (ε_r) and

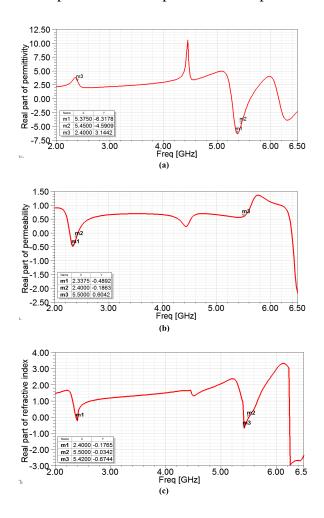


Figure 3.2: Real part of permittivity (a), real part of permeability (b), and real part of refractive index (c).

refractive index(n), as a function of frequency along with their respective values at the desired

frequencies. From the Fig. 3.2 (a)and(b), it can be observed that negative effective permittivity and negative effective permeability are obtained at 5.45 GHz and 2.4 GHz respectively. Thus, the structure shows single negative (SNG) behaviour at the two desired resonant frequencies. Table 3.1 gives the values of permittivity, permeability and refractive index at the desired resonant frequencies.

Table 3.1: Real values of ε, μ, n .

Resonant frequency [GHz]	$Re(\varepsilon)$	Re(µ)	Re(n)
2.4	3.14	-0.186	-0.1765
5.45	-4.59	0.5746	0.3991

In the next section, the design and simulation results of a dual band antenna using the proposed unit cell is discussed.

3.2 ANTENNA DESIGN AND SIMULATION APPROACH

The geometry and dimensions of the proposed dual-band antenna using metamaterial inspired triangular SRR are illustrated in Fig. 3.3. It is fabricated using an FR-4 dielectric substrate of thickness = 1.6 mm. The proposed antenna has a compact size of only 20 mm×24 mm or $0.163\lambda_0\times0.196\lambda_0$ where, λ_0 is the lower resonant frequency of antenna i.e. 2.45 GHz. We employ $50\text{-}\Omega$ coplanar waveguide (CPW) and square ground plane to feed the antenna. Thus, the proposed metamaterial inspired antenna uses double triangular split ring resonator, an open circuited stub and square ground plane to excite the dual band operation at the desired frequencies.

Table 3.2 gives the design parameters of proposed antenna structure shown in Fig. 3.3.

The two resonant frequencies at 2.45 GHz and 5.45 GHz are achieved with the help of the triangular SRR. Since, electrically small antennas have a disadvantage of poor impedance matching, an open circuited stub is used in order to overcome this problem. It also helps in bandwidth enhancement of the antenna at higher frequency band. The open circuited stub is etched just below the triangular SRR, as shown in Fig. 3.3.

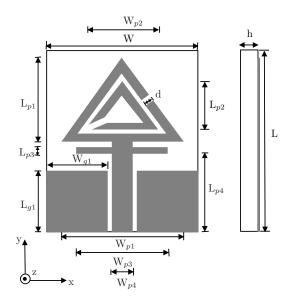


Figure 3.3: Schematic configuration of the proposed dual band antenna.

Table 3.2: Design parameters of the proposed antenna

Parameters	Unit (mm)	Parameters	Unit (mm)	
W	20	L	24	
\mathbf{W}_{p1}	15	L_{p1}	9.8	
W_{p2}	9	L_{p2}	6.9	
W_{p3}	13	L_{p3}	0.5	
W_{p4}	2.25	L_{p4}	10.5	
\mathbf{W}_{g1}	8.5	L_{g1}	8.5	
d	0.9	h	1.6	

Now, Fig. 3.4 shows a step wise procedure to obtain the required frequency band. It demonstrates the effect of including triangular SRR and open circuited stub on the reflection coefficient of the antenna. The figure shows that in the case I when we have a simple triangular patch geometry, the band obtained with reflection coefficient > -10 dB is beyond 5 GHz. The frequency of operation (f_r) of triangular patch in dominant mode of operation is governed by following relation:

$$f_r = \frac{2c}{3L_{eff}\sqrt{\varepsilon_{reff}}}\tag{3.8}$$

where c is the speed of light in vacuum, L_{eff} is the effective length of the patch which is calculated as:

$$L_{eff} = w_{p1} + \frac{h}{\sqrt{\varepsilon_{reff}}} \tag{3.9}$$

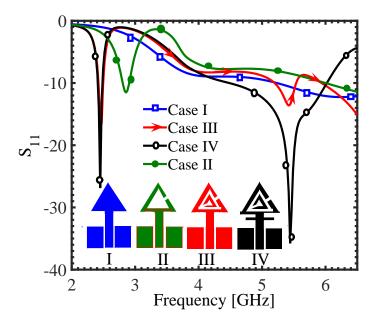


Figure 3.4: Stepwise evolution procedure of the proposed antenna.

and $arepsilon_{reff}$ is the effective dielectric constant of the substrate obtained by following relation

$$\varepsilon_{reff} = \frac{\varepsilon_r + 1}{2} + \frac{\varepsilon_r - 1}{4} \left[1 + 12 \frac{h}{w} \right]^{\frac{-1}{2}}$$
(3.10)

where *h* is the hight of substrate and *w* is the width of the patch. Using the above equations, the resonant frequency is obtained to be 6.9 GHz. As soon as the conventional triangular shape is replaced with the metamaterial inspired single triangular split ring geometry (case II), the band shifts towards lower side near 2.6 GHz. Further adding another split ring inside the previous one (case III) displays dual band characteristics. Two resonant frequencies are obtained, one at 2.45 GHz and other at 5.45 GHz, achieving structure miniaturization by nearly 2.5 times. But still the antenna does not show a good amount of impedance matching. For improving the impedance matching, an open circuited stub is etched just below the triangular SRR as shown in Fig 3.4 (case IV). It improves the impedance bandwidth at higher frequency band. Thus, we observe dual band characteristics with quite good impedance matching covering entire WLAN band.

Further, the simulated surface current distributions are plotted at the sample frequencies

of 2.45 and 5.45 GHz, respectively as shown in Fig. 3.5. From Fig. 3.5 (a), one can find that

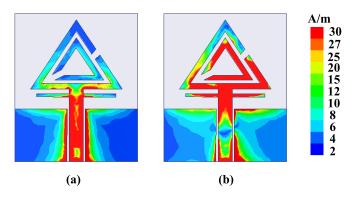


Figure 3.5: Simulated surface current distributions at (a) 2.45 GHz and (b) 5.45 GHz

strong surface currents concentrate on the outer ring of the triangular SRR. Therefore, we can conclude that the 2.45 GHz WLAN band resonance occurs mainly due to the outer ring of the triangular SRR while the open circuited stub is responsible for impedance matching at this band. For the 5.45 GHz operation [see Fig. 3.5(b)], it can be seen that the current density is maximum on both the rings of triangular SRR, hence, that is responsible for resonance at 5.45 GHz. Thus, from the current distribution it can be concluded that the proposed antenna can provide dual band operation covering the 2.4/5.2/5.8 GHz WLAN.

In the next section, different simulated performance parameters such as impedance, reflection coefficient, radiation pattern, and gain are calculated for the proposed antenna.

3.3 RESULTS AND DISCUSSION

3.3.1 Impedance Performance

For a practical antenna system, it is required to have a reflection coefficient better than -10 dB for the desired band operations. This implies acceptable amount of radiated power from an antenna. Fig. 3.6 shows the simulated reflection coefficient of the proposed metamaterial antenna. It shows operates in the desired frequency bands ranging from 2.40-2.48 GHz with 27 dB return loss at resonant frequency 2.45 GHz and 4.7-6.04 GHz with 36 dB return loss

at resonant frequency 5.45 GHz, which covers the entire WLAN band spectrum (2.4/5.2/5.8 GHz).

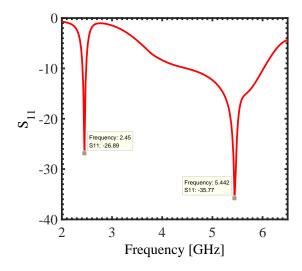


Figure 3.6: Simulated S-Parameters against frequency for the dual band antenna

3.3.2 Radiation Performance

The 2D simulated radiation characteristics in terms of directivity of the proposed antenna for E-plane and H-plane at the two resonant frequencies i.e. 2.45 and 5.45 GHz, are shown in Fig 3.7. The E-plane corresponds to azimuth angle $\phi = 0^{\circ}$, 90° for all values of θ (Fig. 3.7 (a),(b),(e),(f))) and H-plane corresponds to the value of elevation angle θ = of 0° , 90° (Fig. 3.7 (c),(d),(g),(h))). The radiation is symmetric and bidirectional in the main plane, however, seems to be radiating in all directions in orthogonal plane. Thus, the proposed antenna gives nearly omnidirectional radiation pattern. Also, the radiation seems to nearly stable across the frequency band.

Fig. 3.8 shows the simulated peak gain and total efficiency for the operating bands. Results show that 62.53 % efficiency at 2.45 GHz and 93.25 % efficiency at 5.45 GHz is achieved. The gain observed is 3.129 dBi to 1.435 dBi for 2.4-2.48 GHz band and 2.319 dBi to 2.907 dBi for 4.7-6.04 GHz band. Thus, a good amount of gain and high radiation efficiency have been achieved at the two frequency bands of the metamaterial inspired antenna.

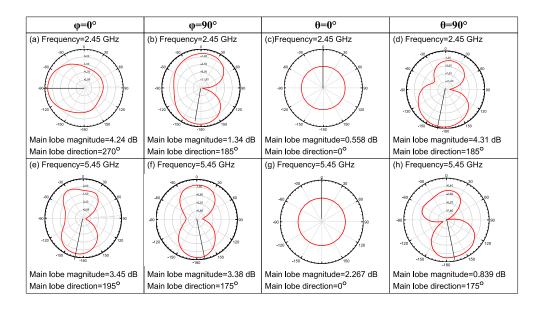


Figure 3.7: The simulated radiation pattern at frequencies 2.45 GHz (a), (b), (c), (d) and 5.45 GHz (e), (f), (g), (h)

3.3.3 Performance Comparison

Various metamterial unit cells have been proposed in literature for miniaturization of antenna. Table 3.3 Gives a brief performance comparison of the proposed antenna with other previously reported metamaterial based antennas along with their respective unit cell configuration. It can be seen that, as compared to most of the well known configurations such as interdigital capacitor with CSRR, meander line, defected ground structure (DGS), resonant ring and modified electric coupled resonator (M-ECL), the proposed unit cell provides smaller size of the substrate along with dual band response.

Table 3.4 gives a performance comparison of proposed metamaterial inspired antenna with previously proposed dual band antennas covering WLAN band spectrum in terms of various antenna properties. From the table 3.3 and 3.4 we can conclude that the proposed antenna offers comparatively large amount of return loss and small size along with wide impedance bandwidth at the higher frequency band. However, gain can be further improved at the higher order band.

Finally, the proposed antenna is fabricated on a $20mm \times 24mm \times 1.6mm$ FR-4 substrate and

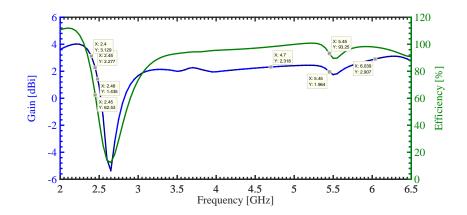


Figure 3.8: Efficiency and gain plots of the metamaterial antenna

Table 3.3: Performance comparison of the proposed antenna with other reported antennas.

Reference	Size	Metamaterial Unit Cell	Operating
	(mm×mm)		Bands (GHz)
[121]	40×35	Interdigital capacitor	3.67-3.93
		and CSRR	
[123]	40×40	Meander line	5.1-6
[126]	23.6×26	Defected ground structure	5.75-5.84
[124]	50×30	Resonant ring	1.67-2.51
[125]	20×32.2	Interdigital capacitor	0.75, 2.16
[128]	45×40	Modified electric coupled	1.30, 2.40-2.93
		resonator	
Proposed	20×24	Triangular split ring	2.4-2.48, 4.7-6.04
		resonator	

measurements are performed. The measured results are discussed in the next section.

3.4 EXPERIMENTAL RESULTS AND DISCUSSION

Measurements of various parameters of the antenna such as return loss, VSWR and impedance bandwidth are done using Keysight N9914A vector network analyzer. Fig. 3.9 shows the fabricated prototype of the proposed antenna. Fig. 3.10 shows the snapshots of the measured reflection coefficient (S_{11}) and VSWR on the Keysight N9914A vector network analyzer. Fig. 3.11 shows the measured and simulated return loss (dB) characteristics of the proposed antenna simultaneously. Both the measured and simulated results match fairly well. From Fig. 3.11 it is clear that the antenna shows the measured bandwidth of 160 MHz (2.34-2.50 GHz)

Table 3.4: Comparative analysis of proposed antenna and previously proposed antennas operating on WLAN band

Reference	Overall Size (mm ²)	Operating bands(GHz)	Return loss (dB)	Peak Gain(dBi)	Impedence bandwidth
[129]	20×35	2.45, 5.5	25, 32	1.7, 3.2	-
[130]	60×70	2.4 to 2.49 (2.45), 5.51 to 6.8 (5.94)	28, 30	2.36, 6.08	90 MHz, 1.26 GHz
[131]	30×33	2.56, 5.2	30, 20	-	14 and 8.5%
[132]	60×45	2.3 to 2.53 (2.45),5.05 to 6.31 (5.3)	18.3, 23.2	2.55, 3.65	230 MHz, 1.26 GHz
[133]	50×50	2.45, 5.14	25.9, 22.6	-3.5, 6.6	135, 583 MHz
[134]	40×30	2.39 to 2.5 (2.44), 5 to 6.06 (5.5)	25, 30	1.66, 4.8	-
[135]	20×40	2.37 to 2.41 (2.4), 5.752 to 5.88 (5.8)	16.1, 12.1	0.4, 1.6	40, 128 MHz
Proposed	20×24	2.4-2.48 (2.45), 4.7-6.04 (5.45)	27, 36	2.277, 1.964	80 MHz, 1.34 GHz

at lower frequency band and 1.97 GHz (4.45-6.42 GHz) at upper-frequency band covering the desired WLAN frequency spectrum.

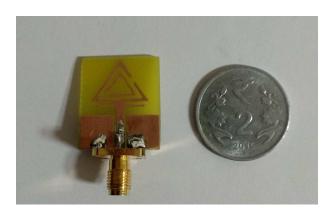


Figure 3.9: Fabricated prototype of antenna.



Figure 3.10: Measurement of (a) Return loss (b) VSWR on Keysight N9914A vector network analyzer.

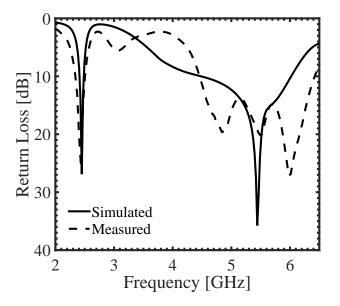


Figure 3.11: Measured and simulated Return loss.

3.5 SUMMARY

A metamaterial inspired, CPW-fed antenna has been designed fabricated and tested. Dual band characteristics have been observed at 2.45 GHz and 5.45 GHz operating frequencies with a gain of 1.9 dBi to 2.41 dBi and 2.2 dBi to 2.5 dBi respectively. The two bands are originated from the metamaterial used in the antenna consisting two triangular split rings and impedance matching is achieved using open circuited stub. Nearly omnidirectional radiation patterns are observed at both frequencies. The experimental results have a good agreement with the simulated results. Thus the proposed antenna supports 2.4/5.2/5.8 GHz WLAN bands which offers wide range of application in wireless communication systems.

In this chapter after studying a metamaterial inspired, CPW-fed dual band microstrip antenna for miniaturization, in coming chapter metamaterial based filters are studied.

CHAPTER 4

METAMATERIAL BASED FILTERS

Contents of this chapter are published as:

- Priyanka Garg and Priyanka Jain, "Design and analysis of Complementary split ring resonator backed microstrip transmission line using equivalent circuit model" *Journal* of Communication Technology and Electronics, vol. 63, no. 12, pp. 1424-1430, 2018.
- Priyanka Garg and Priyanka Jain, "Extraction of equivalent circuit parameters of metamaterialbased bandstop filter," *Applications of Artificial Intelligence Techniques in Engineering*, vol. 697, pp. 173-179, 2019. (SCOPUS)
- 3. **Priyanka Garg** and Priyanka Jain "Comparative analysis of transmission line based bandstop filters using different metamaterial unit cells operating at 3 GHz" presented in *International Conference on Signal Processing, VLSI and Communication Engineering* (ICSPVCE-2019), March 28-30, 2019, New Delhi, India.
- 4. **Priyanka Garg** and Priyanka Jain, Design and Analysis of a Bandpass filter using Dual Composite Right/Left Handed (D-CRLH) Transmission Line showing bandwidth enhancement, *Wireless Personal Communication*. (Communicated).
- Priyanka Garg and Priyanka Jain, "Analysis of metamaterial based bandstop filters: A
 Brief Review" presented in 5th International Conference on Microelectronics, Computing & Communication Systems (MCCS-2020), July 11-12, 2020, Advanced Regional
 Telecom Training Centre, BSNL, Ranchi, Jharkhand, India.

4.1 COMPLIMENTARY SPLIT RING RESONATOR BACKED MICROSTRIP TRANS-MISSION LINE USING EQUIVALENT CIRCUIT MODEL

Filters form an essential element in various RF, microwave and other communication system for either accepting or rejecting a band of frequency. Bandstop filters are used in various applications for suppressing undesired frequency bands. Various band stop filters have been proposed using planar technology. Most of the band stop filters are realised by etching slots on the structure. [136] presented a broad band-stop filter using periodic L-shaped stubs with defected ground plane for X-band applications. These defects are realised by etching slots in the ground plane. [137] proposed a band stop filter with defected mirostrip structure (DMS) by etching M-shaped slots on the microstrip. Slot shape and size determine the stopband characteristics of the filter.

Although, utilizing planar technology, at some point the design suffer from the drawback of large dimensions. Use of metamaterials in such cases has proven to exhibit exceptional reduction in dimensions. Metamaterials are artificially engineered structures that provide extraordinary characteristics such as negative permittivity (ε) and permeability (μ). Split ring resonators (SRR) have been shown to exhibit negative permeability around resonant frequency [138]. Complementary Split Ring Resonator (CSRR), is the counter image of SRR which shows negative permittivity for a particular band of frequencies [139]. CSRR etched on the ground plane at the back of a microstrip line is a well known technique to realise filters. [140] presented a CSRR based high pass filter utilizing C-shaped coupling. An Open Complementary Split Ring Resonator (OCSRR) with 80 % fractional bandwidth at central frequency 5 GHz is designed by [141]. A wideband bandpass filter with CSRR loaded microstrip transmission line is presented by [142] utilizing Evolution Strategy (ES) method for parameter optimization..

In this chapter a compact sized bandstop filter utilizing Complementary Split Ring Resonator (CSRR) is proposed. The proposed filter is designed to suppress 2.4 GHz frequency band. The main objective is to demonstrate a methodology for selection of suitable equiva-

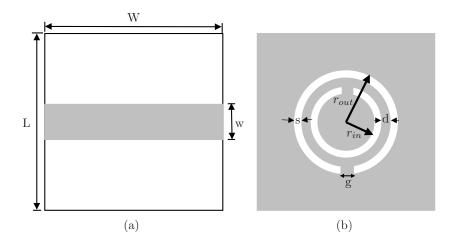


Figure 4.1: (a)Top microstrip line (b) CSRR etched bottom ground plane.

lent circuit arrangement based on simulated results of the filter i.e. transmission coefficient and impedance curve, in order to study the electrical behaviour of the design. [143] presented the extraction of equivalent circuit model, however using the methodology presented in this paper, we have found that the number of lumped elements used can be reduced further. A stepwise simplified mathematical approach for parameter extraction of the equivalent circuit is also presented. All the design and circuit simulations are performed using Computer Simulation Tomography Microwave Studio [144] and Computer Simulation Tomography Design Studio [145]. Finally the design is fabricated and measured.

4.1.1 Design and Circuit Simulation Approach

Fig.4.1 illustrates the geometry and dimensions of the proposed bandstop filter with a 50- Ω microstrip line on top side and CSRR etched on the bottom ground plane. It is designed using FR-4 dielectric substrate with relative permittivity = 4.3, and thickness = 1.6 mm. The proposed BSF has a compact size of only 27 mm×20 mm. The dimensions of microstrip line are chosen to deliver 50- Ω characteristic impedance.

The design parameters of proposed bandstop filter are given as: L=20mm, W=27mm, w=3.1mm, r_{out} =5mm, r_{in} =2.85mm, g=0.6mm, s=0.7mm and d=0.75mm. In an SRR, each ring can be modelled as an inductor and the gap between the rings can be modelled as ca-

pacitor. CSRR, being the dual of SRR, shows complementary effect where the inductance is substituted by capacitance of the disk and the gap capacitance is substituted by inductance between the slotted rings [146].

The circuit equivalent of the proposed BSF can be realized by using the transmission coefficient (S_{21}) and impedance characteristics, shown in Fig. 4.3(a) and Fig. 4.3(b) respectively, obtained after design simulation. Since, the impedance curve shows inductive effect below resonant frequency and capacitive effect above it, so it is concluded that the circuit must contain a parallel resonant circuit. Further, S_{21} curve, as shown in Fig. 4.3(a), shows negative insertion loss (IL), given by,

$$IL = 10log_{10}|S_{21}(f)|^2 (4.1)$$

Thus, the circuit equivalent of the simulated bandstop filter is a series connected parallel resonant circuit. The proposed bandstop filter shows maximum transmission at 1.771 GHz and minimum transmission at 2.401 GHz. This can be illustrated through the power flow plot shown in Fig. 4.2. Fig. 4.2 (a) shows that the filter allows power flow from port 1 to port 2 at 1.771 GHz whereas in case of 2.4 GHz, as shown in Fig. 4.2 (b), most of the power flow is restricted around the resonator. Therefore, we can say that frequency band at the vicinity of 2.4 GHz is prohibited to pass through the filter.

Fig. 4.4 shows the equivalent circuit obtained on the basis of simulated results.

Consider f_1 be the maximum transmission frequency, f_2 be the minimum transmission frequency and f_3 be the frequency at which insertion loss is 3 dB such that $f_1 < f_3 < f_2$. f_3 is obtained at the intersection of reflection and transmission coefficient S_{11} and S_{21} respectively, since,

$$|S_{11}|^2 + |S_{21}|^2 = 1 (4.2)$$

and at the intersection point, $S_{11} = S_{21}$. Thus, $S_{11} = 1/\sqrt{2}$ or 3 dB insertion loss.

The stepwise parameter extraction method, considering the circuit to be lossless, is summarized below:

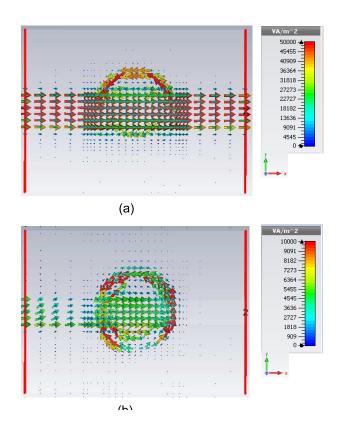


Figure 4.2: Power flow at (a)1.771 GHz (b)2.4 GHz.

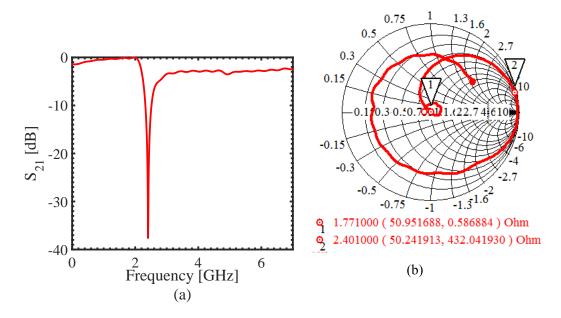


Figure 4.3: (a) Transmission coefficient obtained by design simulation. (b) Impedance curve obtained by design simulation

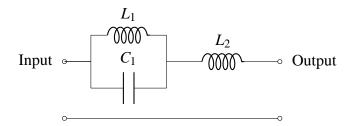


Figure 4.4: Equivalent circuit of the proposed Bandstop filter.

- 1. At the resonance condition of the parallel LC circuit i.e. f_2 , S_{21} leads to zero. This gives the equation for C_1 in terms of L_1 and frequency f_2 .
- 2. At the resonance condition of the whole tank circuit i.e f_1 , S_{11} leads to zero. This gives the relation for L_1 in terms of L_2 and frequencies f_1 , f_2 .
- 3. Finally, at 3 dB insertion loss with frequency f_3 , the third relation for L_2 in terms of frequency f_1 , f_2 and f_3 is obtained.

The S-parameter matrix of the series connected parallel LC resonator is given by,

$$\begin{bmatrix} S \end{bmatrix} = \begin{bmatrix} \frac{Y_0}{Y_0 + 2Y} & \frac{2Y}{Y_0 + 2Y} \\ \frac{2Y}{Y_0 + 2Y} & \frac{Y_0}{Y_0 + 2Y} \end{bmatrix}$$

where $Y_0=1/Z_0$, Z_0 is the characteristics impedance of the line which is 50- Ω and Y is the input admittance of the LC circuit. The mathematical approach for parameter extraction using above steps is summarized below:

1. Taking $S_{21} = 0$. Considering only parallel LC circuit (L_1, C_1)), the input admittance is expressed as,

$$Y = \frac{1 - \omega^2 L_1 C_1}{j\omega L_1} \tag{4.3}$$

From the S-parameter matrix,

$$S_{21} = \frac{2Y}{Y_0 + 2Y} = \frac{2\left[\frac{1 - \omega_2^2 L_1 C_1}{j\omega_2 L_1}\right]}{Y_0 + 2\left[\frac{1 - \omega_2^2 L_1 C_1}{j\omega_2 L_1}\right]} = 0$$
(4.4)

$$1 - \omega_2^2 L_1 C_1 = 0 \tag{4.5}$$

On solving above equation, we obtain,

$$C_1 = \frac{1}{4\pi^2 f_2^2 L_1} \tag{4.6}$$

2. Equating S_{11} to zero,

$$S_{11} = \frac{Y_0}{Y_0 + 2Y} = \frac{Z}{Z + 2Z_0} = 0 \tag{4.7}$$

Considering the input impedance of overall tank circuit,

$$Z = \frac{j\omega_2 L_1}{1 - \omega_2^2 L_1 C_1} + j\omega_2 L_2 \tag{4.8}$$

Substituting value of Z from eqn. 4.8 to eqn 4.7, we obtain,

$$\frac{j\omega_2 L_1}{1 - \omega_2^2 L_1 C_1} + j\omega_2 L_2 = 0 \tag{4.9}$$

On solving, we get,

$$L_1 + L_2 - \omega_1^2 L_1 L_2 C_1 = 0 (4.10)$$

substituting value of C_1 form eqn. 4.6,

$$L_1 + L_2 - \frac{\omega_1^2}{\omega_2^2} L_2 = 0 (4.11)$$

Solving for L_1 ,

$$L_1 = L_2 \left[\frac{f_1^2}{f_2^2} - 1 \right] \tag{4.12}$$

3. Now, the condition for 3 dB insertion loss is given as,

$$|S_{21}| = \frac{2Y}{Y_0 + 2Y} = \frac{2Z_0}{Z + 2Z_0} = \frac{1}{\sqrt{2}}$$
(4.13)

$$\frac{2Z_0}{\sqrt{\left[\frac{j\omega_3 L_1}{1 - \omega_3^2 L_1 C_1} + j\omega_3 L_2\right]^2 + 4Z_0^2}} = \frac{1}{\sqrt{2}}$$
(4.14)

Now, on substituting the value of C_1 from eqn (4.6) in above eqn. and solving, we get,

$$2Z_0 \left(1 - \frac{f_3^2}{f_2^2} \right) = \omega_3 \left[L_1 + L_2 \left(1 - \frac{f_3^2}{f_2^2} \right) \right]$$
 (4.15)

Substituting the value of L_1 from eqn. (4.12) in above eqn. and solving, we obtain,

$$L_2 = \frac{Z_0(f_2^2 - f_3^2)}{\pi f_3(f_1^2 - f_3^2)}$$
(4.16)

In the next section, the S-parameter response of the filter are discussed and circuit parameters are obtained.

4.1.2 Results and Discussion

From the results obtained after simulating the BSF design, we get $f_1 = 1.771$ GHz, $f_2 = 2.401$ GHz, $f_3 = 2.217$ GHz. Substituting all these values in Eqn. (4.6), (4.12), (4.16), we obtain the values of circuit parameters L_1 , C_1 , L_2 as 1.563 nH, 2.81 pF and -3.429 nH respectively. Using the values of L_1 , C_1 , L_2 , the equivalent circuit of BSF is designed and simulated in CST microwave studio and results are obtained. Fig. 4.5 shows the simulated reflection and transmission coefficient of the CSRR based BPF comparative to that of its circuit equivalent. Also, the Fig. 4.7(a) and Fig. 4.7(b) simultaneously shows the impedance curve of simulated

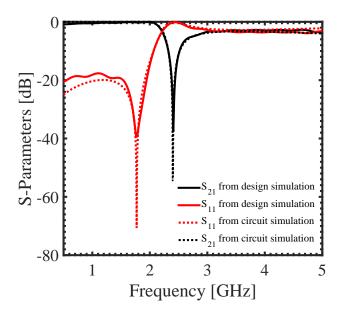


Figure 4.5: Transmission coefficient obtained by design and circuit simulation (solid lines show design simulated S-parameters and dashed lines show circuit simulated S-parameters)

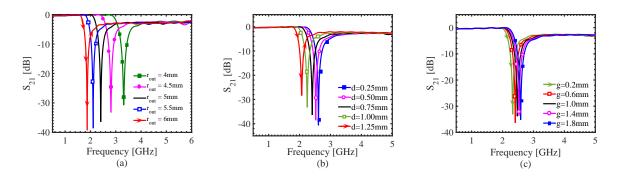


Figure 4.6: (a) Parametric analysis of (a) r_{out} (b) d (c) g.

design and circuit. Little mismatch in the impedance may be due to presence of losses in the design. Both the results show that the circuit is a close approximation of the proposed BSF.

Now, it is important to note that the value of inductance L_2 is a negative quantity. It can be explained as the presence of an equivalent capacitance, say C_2 ([147]).

$$X_L = -j\omega L_2 \tag{4.17}$$

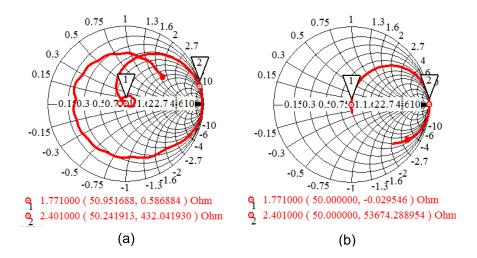


Figure 4.7: Impedance curve obtained by (a) design simulation, (b) circuit simulation

where negative sign indicates the negative nature of inductance L_2 .

$$X_L = \frac{1}{j\omega\left(\frac{1}{\omega L_2}\right)} \tag{4.18}$$

Thus,

$$C_2 = \frac{1}{\omega^2 L_2} \tag{4.19}$$

Since, there are two resonance phenomenon observed in the design, one is the parallel resonance occurring at f_2 and other is the weak series resonance occurring at lower frequency f_1 . At f_2 , resonance is due to the parallel resonant circuit L_1 and C_1 . At lower frequency, the parallel resonant circuit behaves as an inductor, say L_1 . Connecting C_2 in series with L_1 gives the weak series resonance at f_1 . From eqn. 4.19, C_2 at frequency f_1 is obtained as 2.35 pF. The simulated results after replacing the negative inductance L_2 by the equivalent positive capacitance C_2 is shown in Fig. 4.8.

Further, a parametric analysis of most significant dimensions is presented in the next section.

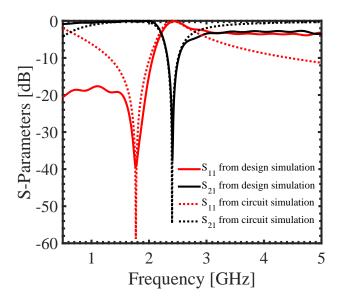


Figure 4.8: Transmission coefficient obtained by design and circuit simulation after replacing inductor L_2 shown in Fig. 4.4 by capacitor C_2 (solid lines show design simulated S-parameters and dashed lines show circuit simulated S-parameters)

4.1.3 Parametric Analysis

Three dimensions are selected for parametric analysis that exhibit major variation in the characteristics of BSF. First one is the radius of the split rings. Fig. 4.6(a) shows the variation in r_{out} keeping the dimensions s, d and g unchanged. It was observed that as r_{out} is increased from 4 mm to 6 mm, the resonant frequency shifts towards lower side.

Second dimension for parametric analysis is the distance between the two rings (d). Fig. 4.6(b) shows variation in d keeping other parameters unchanged. As the parameter d is increased from 0.25 mm to 1.25 mm, the frequency again shifts to lower values.

Finally, variation in the split gap (g) is performed. Fig. 4.6(c) shows, as the split gap of the rings is increased from 0.2 mm to 1.8 mm, the frequency shifts towards higher values. Thus, suitable dimensions of the CSRR can be selected to obtain the desired resonant frequency as per the required specification. Finally the filter is fabricated on FR-4 substrate and measurements are performed.

4.1.4 Experimental Results and Discussion

Fig. 4.9 shows the fabricated bandstop filter showing microstrip transmission line on top and CSRR etched on the bottom ground plane. Keysight N9914A vector network analyzer is used to carry out the measurements of various parameters of the fabricated CSRR based bandstop filter(BSF) such as reflection coefficient, transmission coefficient and 3-dB bandwidth. Fig. 4.10 shows the S-parameters as observed on the Keysight N9914A vector network analyzer. Fig. 4.11 simultaneously shows the measured, design simulated and circuit simulated values of S-parameters of the proposed BSF. The measured results shows a 3-dB stopband from 2.113 GHz to 3.088 GHz giving a 3-dB bandwidth 0.975 GHz. The occurrence of ripples in the measured results may be due cable losses. The measured results match well with the simulated results.

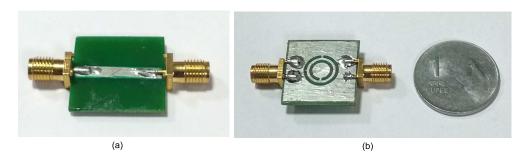


Figure 4.9: Fabricated BSF(a) Top view, (b) Bottom view

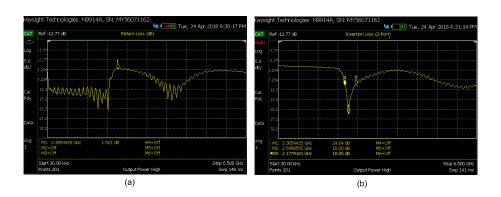


Figure 4.10: Snapshots of results on Keysight N9914A vector network analyzer (a) Return loss (b) Insertion loss

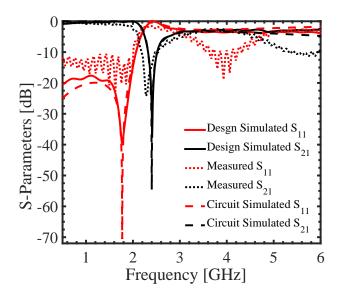


Figure 4.11: Measured and simulated S-parameters of proposed BSF

4.1.5 Summary

A complementary split ring resonator based bandstop filter has been designed and simulated. A stop band at the vicinity of 2.4 GHz is obtained. Based on the simulated results, the circuit arrangement is defined to be a series connected parallel resonant circuit followed by a series connected inductor. Simplified mathematical approach is described in detail to obtain the lumped circuit parameters. Only three lumped components are used to define the circuit model, thus reducing the circuit complexity. Further more, parametric variation of the split rings is analysed which displays frequency tuning capability by varying the dimensions of split rings. Finally, the filter is fabricated and measured to show fair agreement with the simulated results. The proposed bandstop filter shows good lower pass band performance. The high frequency pass band shows large reflections which may be improved further.

Here, a complementary split ring resonator based bandstop filter is successfully analysed and demonstrated. A detailed methodology for equivalent circuit extraction is also given which is further validated in the next section by utilizing it to extract the equivalent circuit of another bandstop filter presented in literature.

4.2 EXTRACTION OF EQUIVALENT CIRCUIT PARAMETERS OF METAMATE-RIAL BASED BANDSTOP FILTER

This section of the chapter presents the design and analysis of a metamaterial inspired Bandstop Filter (BSF) providing suppression of frequency at 3GHz. The overall size of proposed BSF is $20mm \times 20mm \times 1.6mm$. Further, the extraction of lumped parameters of the designed BSF using simulated results is presented and validation of the results using equivalent circuit simulation is also presented. The analysis is performed using transmission coefficient, reflection coefficient and impedance curve.

The objective of present work is the parameter extraction of the circuit of an Open Slot Split Ring Resonator (OSSRR). OSSRR was designed by Karthikeyan et al. in [148] and it was observed that OSSRR offers lower resonant frequency compared to the CSRR of similar dimensions. The work proposed in this section provides an extension by utilizing OSSRR to operate at 3 GHz, further study of electrical behaviour of OSSRR by extraction of equivalent circuit model. The simulated transmission coefficient and impedance curve are used to determine the lumped equivalent circuit and a mathematical model is described in detail for the extraction of circuit parameters (as discussed in the previous section). The design is further validated using circuit simulation results. The equivalent circuit extraction is important to study the electrical behavior of the planar design in order to provide ease of integration with any external electrical circuit. All the design and circuit simulations are carried out using Computer simulation Technology (CST) Microwave studio (MWS) [144] and CST design studio [149] respectively.

4.2.1 Design and circuit simulation

The proposed bandstop filter is designed using a 1.6mm thick FR-4 substrate (r=4.4) with dimensions $20\times20mm^2$. The substrate consists of a 50- Ω microstrip line on the top and an Open Slot Split Ring Resonator (OSSRR) on the bottom. Fig. 4.12 shows the design of the proposed band stop filter along with the port assignments.

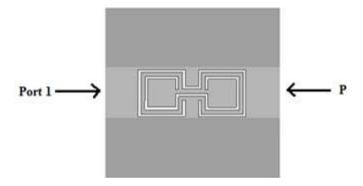


Figure 4.12: Design of proposed bandstop filter (light grey color shows 50 microstrip line on top and dark grey color shows OSSRR on bottom of substrate).

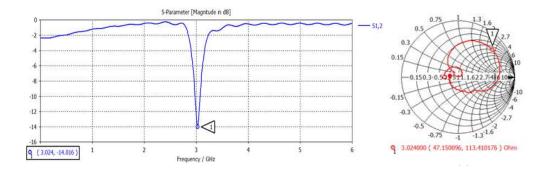


Figure 4.13: Simulated transmission coefficient and impedance curve of the proposed bandstop filter design.

The bandstop filter is designed and simulated in CST microwave studio and results are obtained. Fig. 4.13(a) shows the simulated transmission coefficient. The Fig. 4.13(a) shows that bandstop filter shows resonance at 3.024GHz, thus performing complete suppression of frequency at 3.024GHz. From the impedance curve, shown in Fig. 4.13(b), it was observed that the BSF shows inductive effect below the resonant frequency and capacitive effect above it. Thus, the equivalent circuit must contain a parallel resonant circuit. Since, the insertion loss is negative, shown in Fig. 4.13(a), we conclude that the equivalent circuit of proposed BSF is a series connected parallel resonator.

The resultant series connect parallel resonant circuit arrangement, assuming no losses, is

shown in Fig. 4.14. The values of L (inductor) and C (capacitor) is obtained using following

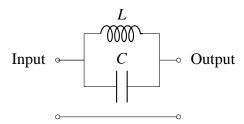


Figure 4.14: Equivalent circuit of the proposed Bandstop filter.

procedure:

- 1. At the resonant frequency, say f_2 , $|S_{21}|=0$.
- 2. At the intersection of $|S_{11}|$ and $|S_{21}|$, say at f1, $|S_{21}|=1/\sqrt{2}$ (Since, $|S_{11}|^2+|S_{21}|^2=1$).

For a series connected parallel resonator, S-parameter matrix is given as,

$$\begin{bmatrix} S \end{bmatrix} = \begin{bmatrix} \frac{Y_0}{Y_0 + 2Y} & \frac{2Y}{Y_0 + 2Y} \\ \frac{2Y}{Y_0 + 2Y} & \frac{Y_0}{Y_0 + 2Y} \end{bmatrix}$$

Using condition 1, $|S_{21}|=0$,

$$S_{21} = \frac{2Y}{Y_0 + 2Y} = \frac{2Z_0}{Z + 2Z_0} = 0 \tag{4.20}$$

From the circuit shown in Fig. 4.14, we obtain,

$$Z = \frac{j\omega_2 L}{1 - \omega_2^2 LC} \tag{4.21}$$

Putting in eq. 4.20, we get,

$$C = \frac{1}{\omega_2^2 L} = \frac{1}{4\pi^2 f_2^2 L} \tag{4.22}$$

Now, using condition 2, $|S_{21}|=1/\sqrt{2}$,

$$\frac{2Z_0}{\sqrt{\frac{\omega_1^2 L^2}{(1-\omega_1^2 LC)^2} + 4Z^2}} = \frac{1}{\sqrt{2}}$$
(4.23)

On solving above equation using eq. 4.22, we obtain,

$$L = \frac{Z_0}{\pi f_1^2} \left[1 - \frac{f_1^2}{f_2^2} \right] \tag{4.24}$$

The equivalent circuit parameters are obtained in the next section.

4.2.2 Results and Discussion

After the design simulations performed on CST Microwave Studio, it was obtained that the intersection of $|S_{11}|$ and $|S_{21}|$ occurs at frequency f_1 =2.88 GHz and resonance at f_2 =3.024 GHz is observed. Using eq. 4.22 and 4.24, we obtain the value of L and C as 0.5 nH and 5.549 pF respectively. The equivalent circuit is designed and simulated in CST design studio. The transmission and reflection coefficient obtained after design and circuit simulations are shown in Fig. 4.15 and 4.16 respectively. Design and circuit simulated impedance curves are also shown in Fig. 4.17 simultaneously. Fig. 4.15 and 4.16 show similar results. Little deviation in the impedance may be due to substrate losses. Thus, we conclude that the equivalent circuit is a close approximation of the proposed Open Slot Split Ring Resonator (OSSRR) based BSF.

4.2.3 Summary

Open Slot Split Ring Resonator (OSSRR) based bandstop filter has been designed and analyzed using equivalent circuit model. The BSF was designed to operate at 3.024 GHz. A methodology based on the simulated design transmission coefficient and impedance curve to select an appropriate circuit model for the BSF was also described. It was found that the proposed BSF could be represented as series connected parallel resonator. The LC lumped

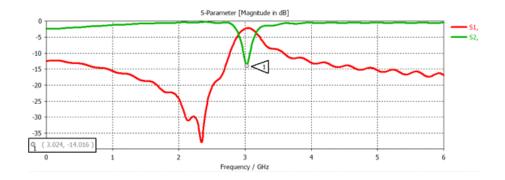


Figure 4.15: Reflection and transmission coefficient of simulated design.

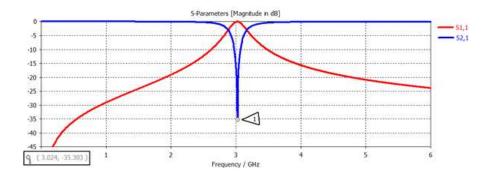


Figure 4.16: Reflection and transmission coefficient of simulated equivalent circuit.

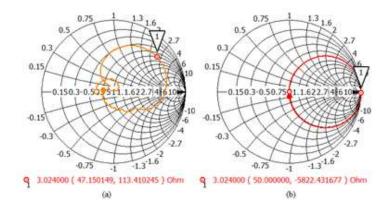


Figure 4.17: Impedance Curve (a) Design (b) Equivalent Circuit

parameters were obtained using suitable mathematical model. Further, the circuit equivalent was simulated and results obtained were comparable to the simulated design results. Thus, the obtained circuit could closely approximate the design.

Further, the next section presents a comparative study of various transmission line based bandstop filters present in literature having defected ground structure. The equivalent circuit approach is also validated in the coming section.

4.3 COMPARATIVE ANALYSIS OF TRANSMISSION LINE BASED BANDSTOP FILTERS USING DIFFERENT METAMATERIAL UNIT CELLS OPERATING AT 3 GHZ

The present work is a comparison based study of microstrip transmission line based bandstop filters taking different complementary resonators on the ground plane. Six metamaterial resonators unit cells have been investigated from the literature. The dimensions are optimized to operate at 3 GHz and then their comparative analysis is performed based on various properties of filters such as insertion loss, 3 dB bandwidth, quality factor (Q), shape factor, overall size, unit cell size and group delay. There are a number of metamaterial based resonators available in literature, so the objective of this section of the chapter is to provide a comparative analysis so that the user can point out the best configuration required while designing the bandstop filter that suits the desired specification and also helps in developing the future ideas by taking into account the advantages of the available structures. All the designing and simulations are performed on Computer Simulation Technology Microwave Studio (CST-MW) In this section, firstly the design of basic microstrip line and different metamaterial unit cells is discussed followed by the design of filter using the microstrip line and unit cells along with their equivalent circuits. Finally, a comparative analysis is presented based on the significant filter parameters.

4.3.1 Design and simulation approach

Basic microstrip transmission line design

A 50- Ω microstrip transmission line is designed on the top of an FR-4 substrate with thickness (h) = 1.6 mm, dielectric constant (ε_r) = 4.4 and loss tangent ($\tan \delta$) = 0.025 with bottom ground plane. Width (W_l) of the line is calculated by taking Z_0 =50 Ω and physical length (L_l) is subjected upon proper impedance matching. Fig. 4.18 shows the schematic of designed transmission line.

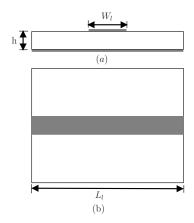


Figure 4.18: (a) Side view of the transmission line (b) Top view of transmission line

Metamaterial unit cells

Fig. 4.19 shows the configuration of metamaterial unit cells that have been investigated to exhibit filtering characteristics. Each of the unit cells is optimized to resonate at 3 GHz and provide negative effective permittivity or permeability or both in the vicinity of its resonant frequency. Fig 4.19(a) and Fig 4.19(b) shows two types of complementary electric inductive-capacitive (CELC) resonator, both of them are characterized by single-negative magnetic moment. CELC in Fig 4.19(a) is denoted as CELC-I [150] and that in Fig. 4.19(b) as CELC-II [151]. Fig. 4.19(c) shows an open slot split rig resonator (OSSRR) [152] which is formed by two connected concentric square slots having openings at the same side, it tend to exhibit electric resonance. Fig. 4.19 (d) depicts a Complementary Split Triangle Resonator (CSTR) [153] which exhibit simultaneous negative permittivity and permeability, thus showing both electric and magnetic resonances. Fig 4.19 (e) and Fig. 4.19 (f) shows the well known and most utilised single split ring resonator (SSRR) [154] and double split ring resonator (DSRR) [155] respectively. Both of them exhibit negative permittivity near resonance.

4.3.2 Design and simulation of metamaterial based filters

Metamaterial resonators are etched on the ground plane underneath the $50-\Omega$ transmission line in order to exhibit filtering characteristics. The length of transmission line, as stated earlier, is

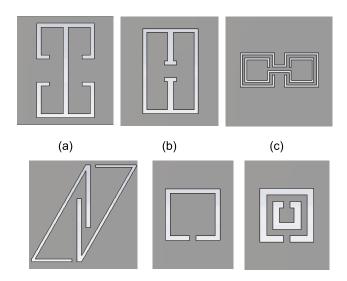


Figure 4.19: (a) CELC-I (b)CELC-II (c)OSSRR (d)CSTR (e)SSRR (f)DSRR

optimized to provide proper impedance matching and so the overall structure dimensions.

CELC-I based bandstop filter

Fig. 4.20(a) shows the schematic of the CELC-I based bandstop filter. Fig. 4.20(b-e) shows the simulated impedance curve, reflection coefficient (S_{11}), transmission coefficient (S_{21}), phase in degrees and group delay. Results shows that the filter operates at the resonant frequency 3 GHz. Along with 3 GHz, one more weak transmission zero can be observed at 5.67 GHz which can be optimised further according to desired specifications. Impedance curve shows that the schematic is capacitive below the resonant frequency and inductive above it so we can say that the equivalent circuit of the designed filter has to be a shunt connected series resonator as shown in Fig 4.21. Phase response shows that at 3 GHz phase changes from positive to negative exhibiting negative phase delay, which is the property of metamaterial. Results (Fig. 4.20(d)) also show a group time delay of -0.548ns. Now, the values of lumped circuit parameters i.e. L_1 and C_1 can be obtained by employing following procedure:

1. At the resonant frequency, say f_1 , $|S_{21}|=0$.

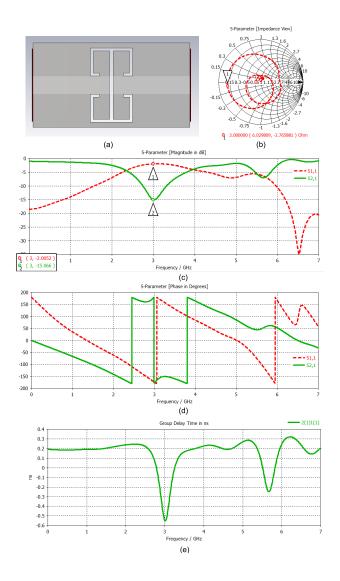


Figure 4.20: CELC-I based bandstop filter

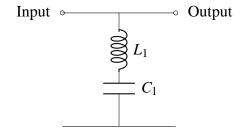


Figure 4.21: Equivalent circuit of the CELC-I bandstop filter.

2. At the intersection of $|S_{11}|$ and $|S_{21}|$, say at f_2 , $|S_{21}|=1/\sqrt{2}$.

The S-parameter matrix of the shunt connected series resonator is given by,

$$\begin{bmatrix} S \end{bmatrix} = \begin{bmatrix} \frac{-YZ_0}{2+YZ_0} & \frac{2}{2+YZ_0} \\ \frac{2}{2+YZ_0} & \frac{-YZ_0}{2+YZ_0} \end{bmatrix}$$

with Y being the admittance of series resonance circuit and Z_0 =50 Ω . On using the condition 1, as stated above,

$$|S_{21}| = \left| \frac{2}{2 + YZ_0} \right| = 0 \tag{4.25}$$

where Y is given by eqn. 4.26

$$Y = \frac{1}{j\omega L_1 + \frac{1}{j\omega C_1}}$$
 (4.26)

Now, putting the value of Y from eqn. 4.26 in eqn. 4.25 for frequency f_1 , we obtain,

$$L_1 = \frac{1}{4\pi^2 f_1^2 C_1} \tag{4.27}$$

and on using condition 2, we obtain following equation for C_1 in terms of f_1 and f_2 :

$$C_1 = \frac{1}{\pi f_2 Z_0} \left[1 - \left(\frac{f_2}{f_1} \right)^2 \right] \tag{4.28}$$

From the S-parameter results shown in Fig. 4.20(c), it is found that f_1 =3 GHz and f_2 =2.37 GHz. Therefore, using eqn. (4.27) and (4.28) we obtain, L_1 =2.79 nH and C_1 =1.01 pF. The equivalent circuit is designed and simulated in CST Design studio. Fig. 4.22 shows the simulated S-parameters of the extracted circuit model which is a close approximation to the design.

Fig. 4.23 demonstrates the power flow in the BSF at 3 GHz and 4 GHz. Fig. 4.23 (a) shows that at 3 GHz, most of the power flow is prohibited to travel from port 1 to 2, thus enabling stop band at 3 GHz, whereas at 4 GHz the power flow is allowed between the ports, as shown in Fig 4.23 (b), enabling passband at 4 GHz.

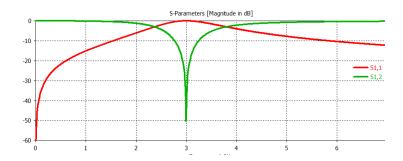


Figure 4.22: CELC-I circuit simulation

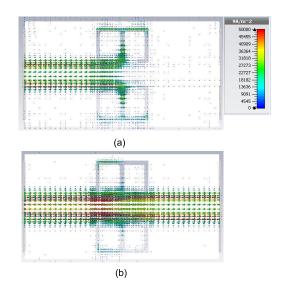


Figure 4.23: Power flow at (a)3 GHz (b)4 GHz

CELC-II based bandstop filter

Fig. 4.24 (a-e) depicts the schematic and simulated results of the CELC-II resonator based bandstop filter. Reflection and transmission coefficient curves, shown in Fig. 4.24(c) proves that it exhibit a transmission zero at 3 GHz, however, the filter also provides a stop band at higher frequencies (>5.5 GHz), which is not desirable in present case. It also provides two reflection zeros at 3.53 GHz and 4.53 GHz showing excellent passband characteristics. The impedance curve shows the similar behaviour as in the case with CELC-I so its equivalent circuit will also be a shunt connected series resonator and can be extracted in the similar

fashion as explained in the previous section. Further, the design is exhibiting a negative phase delay and a group delay time of -1.156 ns.

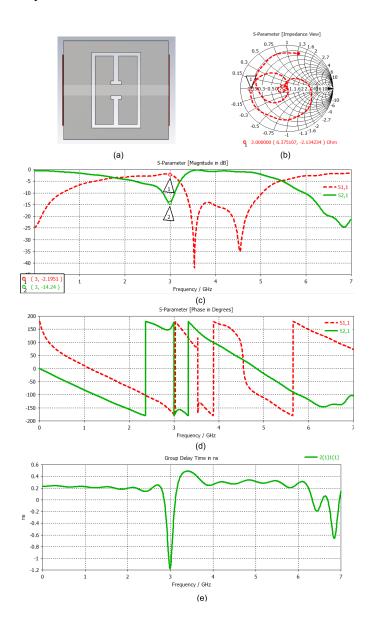


Figure 4.24: CELC-II based bandstop filter

OSSRR based bandstop filter

Fig. 4.25 (a-e) depicts the schematic and simulated results of the OSSRR based bandstop filter showing only one transmission zero at 3 GHz. However, it has a narrow bandwidth

of 0.272 GHz comparative to other configurations (discussed later). The equivalent circuit of OSSRR based BSF consist of series connected parallel resonator, since, the impedance curve (Fig. 4.25(b)) shows inductive nature below and capacitive nature above the resonant frequency. However, there is a reflection zero existing at the lower frequency 2.12 GHz, in order to incorporate it, a capacitor is added in series with the LC tank circuit, as depicted in Fig. 4.26. Fig. 4.25(d) and (e) also shows negative phase delay and group delay time of -9.97 ns. The values of lumped circuit parameters as shown in Fig. 4.26 are obtained by following

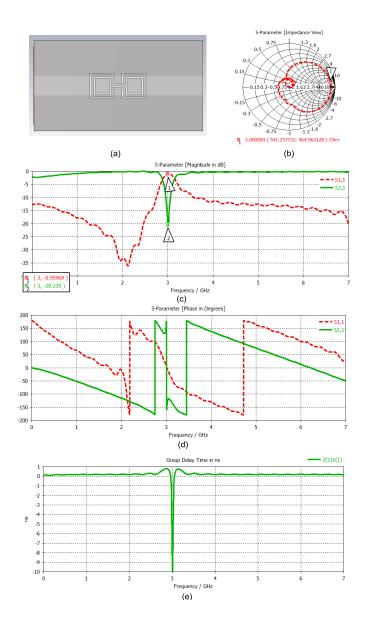


Figure 4.25: OSSRR based bandstop filter

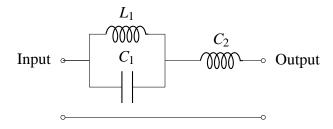


Figure 4.26: Equivalent circuit of OSSRR based bandstop filter.

the same procedure as mentioned in previous section. The equation for obtaining L_1 and C_1 is given as follows:

$$C_1 = \frac{1}{4\pi^2 f_1^2 L_1} \tag{4.29}$$

$$L_1 = \frac{Z_0}{\pi f_2} \left[1 - \left(\frac{f_2}{f_1} \right)^2 \right] \tag{4.30}$$

At lower frequencies, this circuit LC parallel circuit will behave like an inductor whose equivalent value at 2.12 GHz (lower reflection zero) is -1.23 nH, so the value of capacitor added in series with -1.23 i.e., C_2 is given by 4.57 pF. Fig. 4.27 shows the simulated S-parameters of the extracted equivalent circuit model of SSRR based bandstop filter.

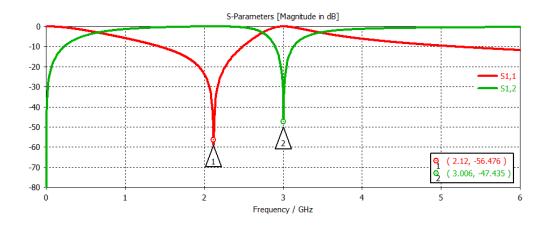


Figure 4.27: OSSRR BSF circuit simulation

SSRR based bandstop filter

Fig. 4.28 (a) shows the schematic of the designed bandstop filter having compact overall dimensions $(22 \times 20mm^2)$ as compared to aforementioned filters. This is one of the most utilised configurations. The equivalent circuit of this configuration would be a series connected paral-

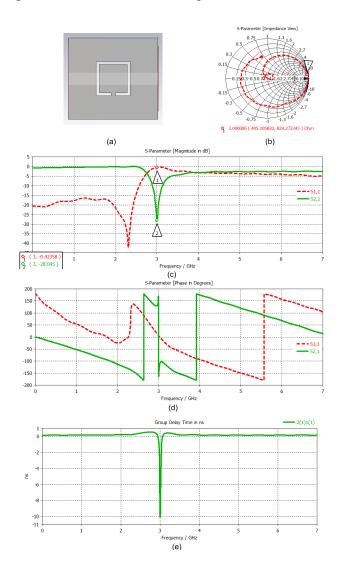


Figure 4.28: SSRR based filter

lel resonator, as depicted from impedance curve shown in Fig. 4.28(b). The S-parameters, in Fig. 4.28(c), shows a transmission zero at 3 GHz with wide 3 dB bandwidth and a reflection zero at 2.31 GHz providing excellent lower pass band characteristics. Because of the reflection zero, a weak series resonance is also observed at 2.31 GHz which is excited in the circuit

by adding an inductor in series with the LC tank circuit. Final circuit obtained is shown in Fig. 4.29 and the equivalent lumped parameters calculated according to the procedure mentioned above are given by, L_1 =1.42 nH, C_1 =1.98 pF, and L_2 =-3.49 nH.

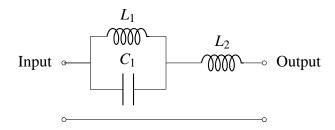


Figure 4.29: Equivalent circuit of the SSRR based bandstop filter.

Fig. 4.30 shows the simulated S-parameters of the extracted equivalent circuit model of SSRR based bandstop filter.

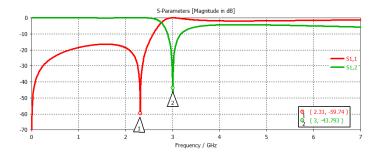


Figure 4.30: SSRR BSF circuit simulation

DSRR based bandstop filter

Fig. 4.31 (a) shows the schematic of the designed bandstop filter. The simulated results shown in Fig. 4.31 (a-e) are similar to that of a SSRR. Double split rings are introduced in order to improve the capacitive and inductive coupling. A double split ring resonator is similar to a single spit ring resonator if the mutual coupling is weak. If the gap between the rings is small or in other words, if the dimensions of two rings are almost same, the double SRR resonates at the frequency close to single SRR but with higher current density resulting into larger magnetic moment [156].

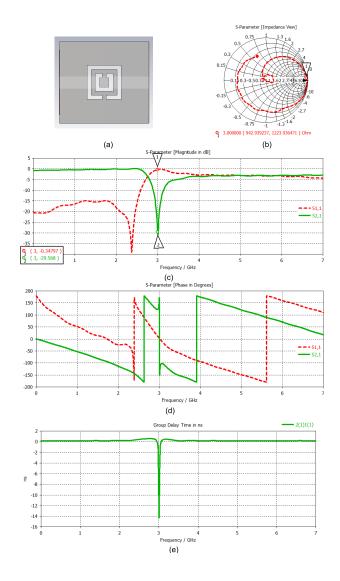


Figure 4.31: DSRR based bandstop filter

The equivalent circuit of DSRR based bandstop filter is also similar to SSRR based bandstop filter, however, the extracted lumped parameters are given as, L_1 =1.608 nH, C_1 =1.75 pF, and L_2 =-4.28 nH. Fig. 4.32 shows the simulated S-parameters of the extracted equivalent circuit model.

CSTR based bandstop filter

Geometrical configuration of CSTR based bandstop filter and its simulated results are illustrated in Fig. 4.33. The S-parameter response (Fig. 4.33(c)) shows that the filter is resonating

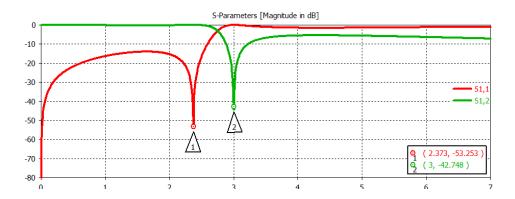


Figure 4.32: DSRR BSF circuit simulation

at 3 GHz along with two reflection zeros, one above the stop band at 3.43 GHz and one below it at 2.49 GHz, providing excellent out of band performance. However, at high frequencies, filter performance is distorted and the overall optimized dimension of the filter is also large $(38\times20mm^2)$. Impedance curve shown in Fig. 4.33(b) depicts that the equivalent circuit of the BSF is a shunt connected series resonator which can be extracted in the similar way as described above. Phase response in this case is also a negative value along with a group delay time of -0.088 ns.

4.3.3 Comparative Analysis

A brief comparative analysis of all the bandstop filters discussed above is given in the Table 4.1. The comparison is done based on different filter performance parameters such as:

- Insertion loss (dB): It is measured as the ratio of signal power delivered to the output terminal versus the signal power at input terminal.
- 3-dB bandwidth (GHz): It is the band of frequencies between the half power points, measured at the cross section of reflection coefficient(S_{11}) and transmission coefficient(S_{21}).
- Quality factor (Q): It is the ratio of energy stored in resonator to the energy supplied to it per cycle to keep signal amplitude constant at resonant frequency (f_r) . It can be

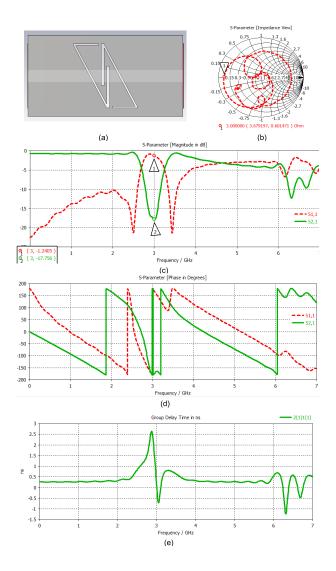


Figure 4.33: CSTR based bandstop filter

obtained using following mathematical definition.

$$Q = \frac{f_r}{Bandwidth} \tag{4.31}$$

- Shape factor: It is a term used to quantify the steepness of a filter's rolloff. Shape factor is the ratio of bandwidth measured using two different attenuation values. In our case we have calculated shape factor for 14/3 dB attenuation.
- Group Delay (ns): It can be defined as negative of change in phase with respect to

change in frequency. Group delay (τ) can be mathematically defined as follows:

$$\tau(\omega) = -\frac{\phi(\omega)}{\omega} \tag{4.32}$$

Negative group delay implies phase lead of the signal with respect to frequency.

Table 4.1: Performance comparison table

Tuble 1.11. I difformance comparison tuble							
Unit cell	Insertion	3-dB Bandwidth	Q-factor	Shape factor	Overall Unit cell	Group	
	loss (dB)	(GHz)	$(f_r/\mathbf{Bandwidth})$	(14/3dB)	size (mm^2) size (mm^2)	delay (ns)	
CELC-I	-15.06	1.62	1.85	0.125	26×14 7×12.3	-0.548	
CELC-II	-14.24	1.45	2.06	0.045	30×28 14×21.5	-1.156	
OSSRR	-20.24	0.272	11.02	0.238	26×14 8.75×3.83	-9.97	
CSTR	-17.75	0.55	5.45	0.467	38×20 15.75×15.75	-0.088	
SSRR	-28.045	1.09	2.75	0.128	22×20 8.4×8.4	-10.08	
DSRR	-29.56	1.68	1.78	0.086	22×20 8.4×8.4	-14.322	

4.3.4 Summary

Different metamaterial unit cells have been investigated and optimised to operate at 3 GHz frequency. Their performance as a bandstop filter is studied by etching out a metamaterial unit cell from the ground plane of the substrate having $50-\Omega$ transmission line on the top. Extraction of equivalent circuits was also performed and it was found that the method provided close approximate equivalent circuit models of the BSFs. Finally a comparative analysis is presented in terms of various performance parameters of the filter such as insertion loss, 3 dB bandwidth, quality factor (Q), shape factor, overall size, unit cell size and group delay. The comparative study is advantageous for the user in order to select the best suitable configuration for a desired application.

In the previous sections, the filters do not offer significant bandwidth, also, the dispersion characteristics have not been studied. In the next section, a novel complementary U shaped resonator based bandstop filter is proposed for wideband operation.

4.4 BANDPASS FILTER USING DUAL COMPOSITE RIGHT/LEFT HANDED (D-CRLH) TRANSMISSION LINE SHOWING BANDWIDTH ENHANCEMENT

A compact, low-profile, Band Pass Filter (BPF) based on balanced Dual Composite Right/Left Handed (D-CRLH) Transmission Line (TL) is presented in this chapter. A balanced D-CRLH TL can be used to provide wideband filter characteristics due to no frequency separation between the RH and LH frequency bands. The proposed D-CRLH TL is designed using U-shaped complementary split ring resonator (UCSRR). The extraction of equivalent circuit model of proposed UCSRR unit cell is also performed. Further, the bandwidth of the proposed filter is enhanced by using the concept of electric and magnetic coupling between the slot lines. The proposed via less BPF has a compact size of 15×15 mm² designed on an FR-4 substrate with dielectric constant(ε_r)=4.3. The design analysis of proposed bandpass filter is presented in terms of reflection coefficient, transmission coefficient, impedance curve, propagation constant and group delay.

Bandpass filters play an important role in various types of radio frequency (RF) and microwave systems in order to accept a particular band of frequencies. With recent advancement in wireless communication technology, requirement of highly efficient, miniaturised and low cost bandpass filter is also increasing. Several approaches have been investigated till date to design high performance filters. Amongst them microstrip technology offers the advantage of compact dimensions, easy integration with circuit elements as well as self tuning capabilities.

Most of the filters are realised by etching slots either on the ground plane or on the microstrip line termed as Defected ground structure (DGS) and Defected microstrip line (DML) respectively. In [157], CSRRs were etched on the microstrip line to achieve low pass characteristics. Bonache et. al designed bandpass filter by etching CSRR on the ground plane and interdigital capacitor on the microstip line to operate on K-band [158]. To provide further cost reduction and miniaturization, multifunctional tunable filters are of great interest these days. A SRR based tunable bandpass filter is presented in [159] realized using varactor diode loaded coplanar waveguide line (CPW). [14] also presents tunable band pass filter based on

capacitive loaded lines.

Caloz and Itoh *et. al.* [40] introduced the concept of metamaterial transmission lines (TL) in 2002. These TL metamaterials typically exhibit a LH band at lower frequencies and a right-handed (RH) band at higher frequencies and are termed as Composite Right/Left Handed Transmission lines (CRLH TL). Mirroring to conventional CRLH behaviour, a novel metamaterial with LC parallel-tank impedance and LC series-tank admittance, termed Dual-CRLH TL (D-CRLH) was proposed in 2006 [160]. Posadas *et. al.* [161] proved that the new structure results in larger bandwidth and lower losses compared to conventional CRLH TL. While, an unbalanced D-CRLH TL can be used to design dual band filters with high rejection between the pass bands [162], a balanced D-CRLH TL can be used to design a filter with wide transmission bandwidth and low losses [163]. In the case of a D-CRLH TL, the right handed passband (at lower frequency) is followed by the left handed passband (at higher frequency) without any frequency separation between them.

To the authors knowledge, few state of the art has been available that utilize D-CRLH TL as a balanced TL to design bandpass filters. In [163] Belenguer *et. al.* have designed a balanced dual-CRLH TL just by modifying the well known Split ring resonator (SRR) to show wider transmission bandwidth. In [164], Cano *et. al.* have extended the same work by enhancing the design to provide reconfigurable bandwidth and propagation characteristics. The present work deals with improving the design complexity as well as the passband bandwidth within a compact structure.

In this chapter a compact sized balanced D-CRLH TL based wideband bandpass filter utilizing U-shaped Complementary Split Ring Resonator (UCSRR) is proposed. The chapter starts with extraction of the material parameters and equivalent circuit parameters of the proposed USRR, followed by designing and analysis of D-CRLH TL bandpass filter. The proposed design is a yia less, D-CRLH TL based wideband bandpass filter designed to provide a 3 dB passband from 2.44 GHz to 5.58 GHz which further is increased from 1.43 GHz to 5.56 GHz on cutting a slot between the two U-shaped resonators (details are discussed in

later sections). This chapter demonstrates the bandwidth enhancement techniques using the concept of electric and magnetic coupling between slot lines. All the design simulations are performed using Computer Simulation Tomography (CST) Microwave Studio.

4.4.1 Design and Simulation Approach

Extraction of material parameters of UCSRR

The design of proposed bandpass filter is based on U-shaped complementary split ring resonator (UCSRR) which exhibits negative refractive index near its resonant frequency. This type of structure provides 180° rotational symmetry, thus avoiding cross polarization and also resulting in smaller electrical size as compared to conventional CSRR [165]. The extraction of material parameters is performed using time domain solver of CST Microwave studio. The initial dimensions of the UCSRR are taken to be according to the sub-wavelength rule of metamaterial i.e. less than $\lambda/4$. As the centre frequency is nearly 4 GHz for the intended band so the major dimension of the UCSRR is chosen to be 11.5 mm which is optimized further. The UCSRR is designed on a FR-4 substrate with relative permittivity = 4.3, and thickness = 1.6 mm, followed by assigning appropriate boundaries. The structure is designed along XY plane where electric boundary is assigned to x-axis, magnetic boundary to y-axis and z-axis is used to assign ports (direction of propagation). Fig. 4.34 illustrates the geometry and port assignment of UCSRR unit cell. Now, effective medium parameters are extracted from the scattering parameters using the modified NicolsonRossWeir (NRW) relations presented in [166]. Taking two arbitrary variables given by following equations:

$$V_1 = S_{21} + S_{11} \tag{4.33}$$

$$V_2 = S_{21} - S_{11} \tag{4.34}$$

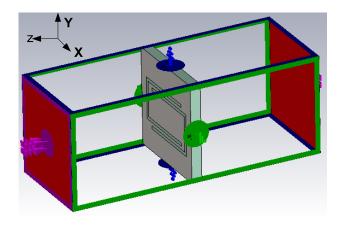


Figure 4.34: Geometry of UCSRR unit cell showing boundary assignment

Complex normalised wave impedance(z) can be obtained by following equations:

$$z = \sqrt{\frac{(1+S_{11})^2 - S_{21}^2}{(1-S_{11})^2 - S_{21}^2}}$$
(4.35)

Now, permeability(μ_r), permittivity(ε_r) and refractive index(n) are obtained simply by:

$$\mu_r = \frac{2}{jkd} \cdot \frac{1 - V_2}{1 + V_2} \tag{4.36}$$

$$\varepsilon_r = \frac{2}{ikd} \cdot \frac{1 - V_1}{1 + V_1} \tag{4.37}$$

$$\varepsilon = n/z \tag{4.38}$$

$$\mu = nz \tag{4.39}$$

where, *k* is the free space propagation constant and *d* is the unit cell dimension. Fig 4.35 and Fig. 4.36 respectively shows the real and imaginary part of the extracted material parameters. It can be observed that the proposed U-CSRR exhibits negative real effective permittivity and permeability in the common frequency range 4.3 GHz to 5.2 GHz, and positive value of imaginary permittivity and permeability for the same range. This results in negative refractive index which means that the proposed unit cell behaves as a left handed material (LHM) in the

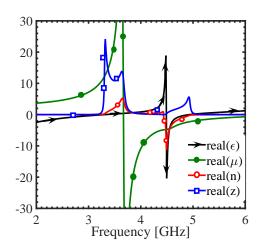


Figure 4.35: Real part of extracted material parameters.

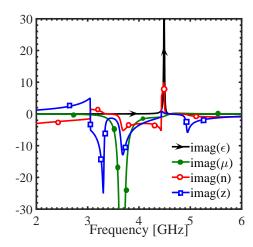


Figure 4.36: Imaginary part of the extracted material parameters.

frequency range 4.3 GHz to 5.2 GHz. Now, in the next section, the design of a bandpass filter using the above proposed UCSRR unit cell is presented

Design of D-CRLH TL Bandpass filter

Proposed D-CRLH TL based wideband bandpass filter is designed on an FR-4 dielectric substrate having compact dimensions $15 \times 15 \times 1.6$ mm². In [56], Falcone *et. al* presented that a microstrip transmission line incorporated by CSRR on the ground plane shows bandstop characteristics, further, on loading the microstrip line with capacitive gaps, the bandstop behaviour switches to bandpass one. Thus, the proposed structure of BPF consists of a 50- Ω

microstrip line with capacitive gap on top side and U-shaped CSRR etched on the bottom ground plane. The dimensions of microstrip line are chosen to deliver $50-\Omega$ characteristic impedance. Fig.4.37 illustrates the geometry and dimensions of the proposed bandpass filter. The slot, shown in Fig. 4.37(c) is introduced between the two U-shaped slots to improve the impedance bandwidth of the filter (discussed in Section III). Table 4.2 gives the design parameters of proposed bandpass filter shown in Fig. 4.37.

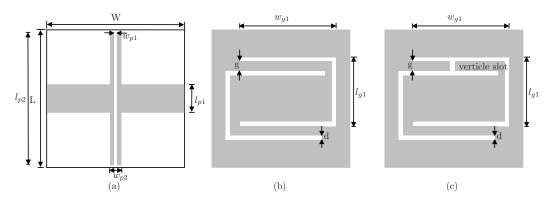


Figure 4.37: (a)Top capacitively loaded microstrip line (b) UCSRR etched bottom ground plane without slot (c) with vertical slot.

Table 4.2: Design parameters of the proposed BPF

Parameters	Unit (mm)	Parameters	Unit (mm)
L	15	W	15
l_{p1}	3	\mathbf{w}_{p1}	0.3
1_{p2}	14	\mathbf{w}_{p2}	0.8
l_{g1}	6.5	\mathbf{w}_{g1}	10.5
g	0.5	d	0.5

In the next section, the S-parameter response of the proposed filter along with the equivalent circuit analysis is illustrated. Further, a bandwidth enhancement approach is presented followed by dispersion characteristics which displays the dual-CRLH behaviour of the filter. Finally, the design synthesis equations are given based on parametric analysis.

4.4.2 Results and Discussion

Fig. 4.38 shows the S-parameters of the proposed BPF. It provides a 3 dB passband from 2.44 GHz to 5.58 GHz with a resonant frequency at 4 GHz. Also, two transmission zeros

can be observed, one in the lower stopband and other in the upper stopband region, therefore, increasing the selectivity of filter and providing good out-of-band rejection level.

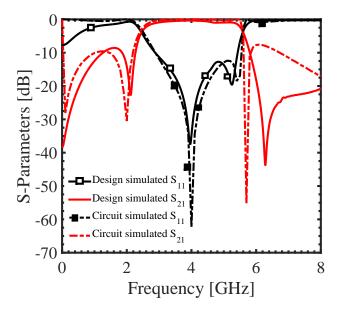


Figure 4.38: S-parameters of the proposed BPF without slot

Extraction of equivalent circuit of proposed filter

The equivalent circuit extraction is important to study the electrical behaviour of the planar design in order to provide ease of integration with any external electrical circuit. In a split ring resonator (SRR), each ring can be modelled as an inductor and the gap between the rings can be modelled as capacitor. CSRR, being the dual of SRR, shows complementary effect where the inductance is substituted by capacitance of the disk and the gap capacitance is substituted by inductance between the slotted rings [165]. The proposed design consists of U-shaped slots that can be modelled as an equivalent capacitor (C_c) whereas the copper between slots where the current flows can be represented as inductor (L_c). The capacitively loaded transmission line on the top of the substrate can be modelled as a series combination of an inductor (L_l) followed by a gap capacitor (C_g) and an inductor (L_l). The equivalent circuit model of proposed filter is shown in Fig. 4.39.

Here, the UCSRR equivalent L_c and C_c are divided into two LC tank circuits joined by

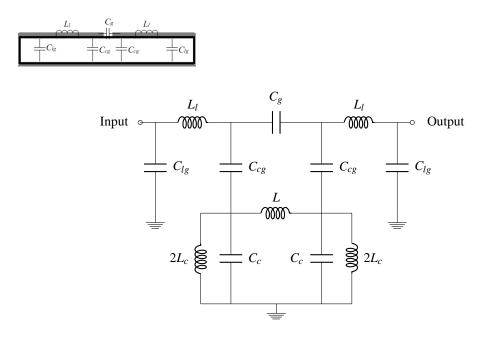


Figure 4.39: Equivalent circuit of the proposed UCSRR filter.

a weak inductance between the upper and lower halves of the structure (L). The parasitic capacitances C_{lg} and C_{cg} are due to the coupling of line with the ground and capacitive gap with the middle portion of the bottom structure respectively. The parameters are obtained using the procedure described in [163]. The approximate expression for the capacitance (C_c) is give by:

$$C_c = (a_{avg} - t/2)C_{pul}$$
 (4.40)

where a_{avg} is the average length of the U-shaped structure by considering it as a rectangular ring, t is the gap between the edges of the U-shaped structure and C_{pul} is the distributed capacitance per unit length and is obtained as:

$$C_{pul} = \frac{\sqrt{\varepsilon_e}}{c_0 Z_0} \tag{4.41}$$

where ε_e and c_0 are the effective permittivity of the medium and velocity of light in free space and Z_0 is the characteristic impedance of the CPW line. ε_e and Z_0 are obtained using the equations give in [167]. Now, the approximate expression for the inductance (L_c) is give

by [167]:

$$L_c = \frac{\mu_0}{2} \frac{b_{avg}}{4} \left[\ln \left(\frac{b_{avg}}{g} \right) - 2 \right] \tag{4.42}$$

where b_{avg} is the length of the line between the U-shaped slots whose thickness is represented as g in the Fig. 4.37. The circuit is designed in Advanced Design System (ADS). The parameters are optimised to match the simulation results as shown in Fig 4.38. The optimised value of parameters are: L_l =2.195 nH, C_g =0.625 pF, C_{lg} =0.33 pF, C_{cg} =1.124 pF, L=1.1 nH, L_c =1.88 nH, C_c =1.39 pF.

The out-of-band rejection level of the filter can be further improved by using a periodic arrangement of the single element. Fig. 4.40 indicates the S-parameter response obtained after using two and three elements of the filter, showing improved out-of-band rejection level as the number of elements are increased.

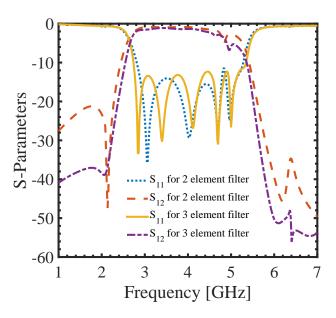


Figure 4.40: Simulated S-parameters obtained after periodic arrangement of the filter

Bandwidth enhancement

Now, the separation 'g' between the two U-shaped slots is varied in order to observe the coupling behaviour between the two adjacent slots. It was observed that on reducing the

separation distance 'g' between the two lateral slots, the passband bandwidth of the proposed filter is increased i.e. the lower cut-off frequency shifts more towards the lower side and the higher cut-off frequency shifts more towards the higher side, as illustrated in Fig. 4.41. Also, one can say that the separation between the two transmission zeros on the lower and upper stop bands increases with decrease in the distance between the two lateral slots which is due to increase in the inductance between them.

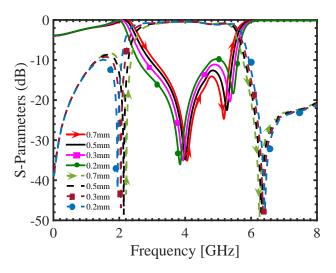


Figure 4.41: Parametric analysis of the separation between the two U-shaped slots i.e. g

Furthermore, when a vertical slot is introduced between the two lateral slots, the direction of propagation of current changes, as depicted in Fig. 4.42, specifically at 1.5 GHz (Fig. 4.42(c,d)). Initially (Fig. 4.42(c)), the current enters the port 1 and is equally distributed on the upper and lower half of the left U-shaped slot and is not allowed to propagate further. Whereas, after the introduction of a vertical slot (Fig. 4.42(d)), the current changes its path and concentrates on the lower half of the structure. The increase in concentration of current between the two lateral slots indicate an increase in effective inductance due to which the lower cutoff frequency shifts towards lower frequency side, thus increasing the passband bandwidth of the filter. Fig. 4.43 shows the simulated S-parameters of the filter after cutting the slot. The effective length (L_{eff}) of the path followed by the current at 1.5 GHz (Fig. 4.42(d)) can be

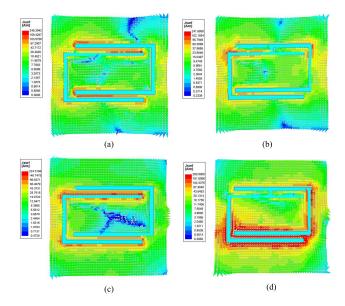


Figure 4.42: Surface current density plot at the bottom surface of proposed filter with slot and without slot respectively at 3.75 GHz ((a), (b)) and at 1.5 GHz ((c), (d))

calculated as,

$$L_{eff} = l_{g1}/2 + 3w_{g1} + l_{g1} + w_{g1}/4 = 43.87mm. (4.43)$$

Now, the frequency can be calculated as,

$$f = \frac{c}{2L_{eff}\sqrt{\varepsilon_r}} \approx 1.58GHz \tag{4.44}$$

The theoretically obtained value is close to the simulated value. Thus, the concept is validated.

So, now the effect of increase in effective inductance can also be incorporated in the equivalent circuit model to demonstrate bandwidth enhancement, as shown in Fig. 4.44. The value of inductance L_c obtained after tuning is 5.066 nH. So we conclude that the bandwidth of the proposed wideband filter can be increased further just by connecting the two U-shaped slots with a vertical slot. Using this technique, the 10 dB passband of the filter now includes the 2.4 GHz WLAN band also which was earlier confined to 3.5 GHz WiMAX band and 5.2 GHz WLAN band. Therefore, this results in the miniaturization of the structure by two times with

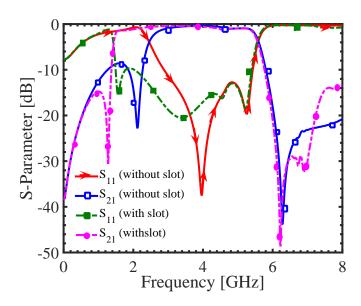


Figure 4.43: S-parameters of proposed design with (shown by solid lines) and without vertical slot (shown by dotted lines)

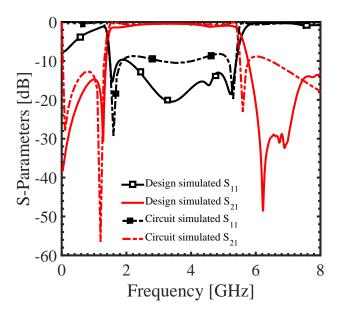


Figure 4.44: S-parameters of the proposed BPF with slot

respect to the lowest 10 dB cutoff frequency.

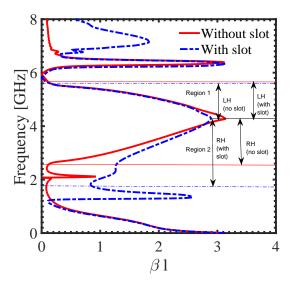


Figure 4.45: Dispersion Diagram of bandpass filter without slot (Solid line) and with slot (Dashed line)

Dispersion characteristics

Fig. 4.45 shows the dispersion diagram of proposed wideband bandpass filter with and without vertical slot. The propagation factor here is $\exp^{\gamma l}$ where l=15 mm is the period of the structure and $\gamma = \alpha + j\beta$ is the complex propagation constant in the direction of propagation given by eqn (4.45) [168].

$$\gamma = \frac{1}{l} \cosh^{-1} \left(\frac{(1 + S_{11})(1 - S_{22}) + S_{12}S_{21} + (\frac{Z_{01}}{Z_{02}})(1 - S_{11})(1 + S_{22}) + S_{12}S_{21}}{4S_{21}} \right)$$
(4.45)

Fig. 4.45 shows that the slope $(d\omega/d\beta)$ of dispersion curve is negative in region 1. This means that the wave has anti-parallel phase velocity (v_p) and group velocity (v_g) in this region. Whereas, region 2 shows positive slope of dispersion curve exhibiting parallel v_p and v_g . Therefore the proposed D-CRLH TL supports backward waves (LH mode) in region 1 (above the resonant frequency) and forward wave in region 2 (below the resonant frequency). A smooth transition is observed between the two regions at the transition frequency approximately 4.2 GHz in both cases, thus, it is said to be a balanced D-CRLH TL. Further, the filter characteristics are also studied in terms of group delay, as shown in Fig. 4.46. Proposed

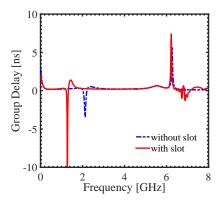


Figure 4.46: Group delay of proposed bandpass filter without slot (Solid line) and with slot (Dashed line)

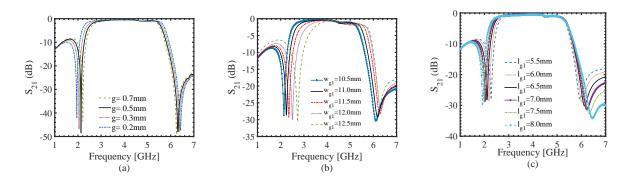


Figure 4.47: Variation with respect to (a) g (b) w_{g1} (c) l_{g1} .

bandpass filter exhibits a maximum delay time of 0.63 ns in the pass band.

Design synthesis and parametric analysis

The parametric analysis is done and design synthesis equations are presented with respect to the most significant dimensions of the filter (shown in Fig. 4.47) in order to help the designer choose the optimal dimensions for the filter to synthesize a filter with given specifications. On increasing g from 0.2 mm to 0.7 mm and keeping all the other dimensions constant, the transmission zeros shift away from each other increasing the operating bandwidth of the filter, as shown in Fig. 4.47 (a). Further, increasing l_{g1} from 5.5 mm to 8 mm again results in similar shift of transmission zeros (shown in Fig. 4.47 (c)) whereas, on varying w_{g1} from 10.5 mm to 12.5 mm, both the transmission zeros shift towards the upper frequency side.

Table 4.3 indicates the synthesis equations of the filter, where f_1, f_2, f_3 and f_4 indicate the frequency at first transmission zero, first 3-dB cut off, second 3-dB cut off and second transmission zero respectively. Using the equations given in table 4.3, one can obtain the dimensions of the filter according to given frequency of operation, however, minute tuning is required to be done.

Table 4.3: Synthesis Equations based on parametric analysis

Parameters	Values (mm)					Synthesis equations	
g	0.2	0.3	0.5	0.7	-	-	$0.55f_1 + 0.96f_2 + 1.985f_3 - 2.75f_4 + 3.236$
w_{g1}	10.5	11	11.5	12	12.5	-	$2.99f_1-0.62f_2+1.29f_3+1.185f_4-19.327$
l_{g1}	5.5	6	6.5	7	7.5	8	$-4.97f_1-1.86f_2-2.97f_3+1.011f_4+25.386$

4.4.3 Comparison with previously proposed BPF

Use of metamaterials based structures in planar technology provide exceptional properties that are generally beyond the scope of conventional structures. A comparative study is performed which shows better performance of the proposed metamaterial based bandstop filter as compared to previously proposed metamaterial based BPF as well as conventional bandstop filters available in literature, given in Table. 4.4. The comparison table shows that the proposed de-

Table 4.4: Comparative analysis of proposed BPF with previously proposed ones

Reference	Size	3-dB	Fractional	Insertion	Center
	(in terms of λ_g)	Bandwidth (GHz)	Bandwidth (%)	loss (dB)	Frequency (GHz)
[169]	0.12×0.22	> 2.64	80.48	0.35	3.25
[170]	0.3×0.1	2.5	55	1.2	4.2
[171]	0.26×0.30	-	3.5	2.3	2.45
[172]	0.48×0.24	1.33	60	0.6	2.05
Proposed BPF	0.15×0.15	4.4	125.7	0.45	3.25

sign provides wider band and compact sized filter as compared to the previously proposed ones. Now the measured results are presented in the next section.

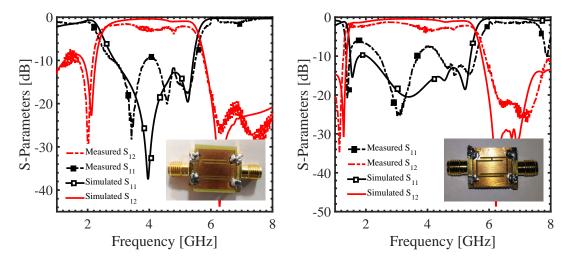


Figure 4.48: (a) Measured and simulated S-parameters of proposed filter without slot. (b) Measured and simulated S-parameters of proposed filter after bandwidth enhancement.

4.4.4 Experimental Results and Discussion

Both the designs are finally fabricated and results are measured using Keysight N9914A vector network analyser. Fig. 4.48(a) and Fig. 4.48(b) shows the measured and simulated Sparameters of the proposed filter before and after applying the bandwidth enhancement technique respectively. Simulated and measured results seem to match fairly well. The measured 3-dB passband bandwidth of the proposed filter is 3.29 GHz ranging from 2.33 GHz to 5.62 GHz which is increased to 4.4 GHz (1.3 GHz to 5.7 GHz) after applying the bandwidth enhancement technique i.e. joining the two U-shaped slots by etching out a vertical slot between them.

4.4.5 Summary

A dual composite right/left handed transmission line based bandpass filter with high stopband rejection level has been designed and simulated. Two closed coupled U-shaped resonators are used to fulfil the purpose. A slot is further introduced between the two U-shaped slots to increase the bandwidth on account of change in the direction of flow of current and increase in effective inductance of the design. The filter provided a 3 dB pass band from 2.44 GHz

to 5.58 GHz which further increased from 1.43 GHz to 5.56 GHz when the vertical slot was placed resulting in miniaturization of the structure by 2 times. The propagation characteristics of the filter have been studied that demonstrated the dual balanced CRLH line behaviour of the filter. Very small amount of group time delay (0.63 ns) is provided by the filter in the passband region. Also, a high return loss of 37.5 dB is achieved at the pass band resonant frequency.

In the present design bandwidth enhancement of the bandpass filter is successfully achieved. The most recent application of metamaterial is in the designing of absorbers so in the next chapter, design of metamaterial absorbers is proposed.

CHAPTER 5

METAMATERIAL ABSORBERS

Contents of this chapter are published as:

- Priyanka Garg and Priyanka Jain, "Novel ultrathin penta-band metamaterial absorber", *AEU - International Journal of Electronics and Communications*, vol. 116, p. 153063, 2020.
- 2. **Priyanka Garg** and Priyanka Jain, "Analysis of a novel metamaterial absorber using equivalent circuit model operating at 3.5 GHz", presented in *IEEE International Conference on Computational Electromagnetics (ICCEM-2020)*, Singapore, 2020.

5.1 NOVEL ULTRATHIN PENTA-BAND METAMATERIAL ABSORBER

5.1.1 Introduction

Electromagnetic absorbers are used to inhibit any reflection and transmission of radiations [173]. Such structures have widespread applications in the area of radar cross section (RCS) reduction [174], antenna side lobe reduction [175], prevention of health hazards by absorbing radiations at particular frequencies and other wireless communication applications. Conventional microwave absorbers are limited to certain applications due to their thickness [176], bulkiness and constant value of permittivity and permeability and frequency ranges. Therefore, in recent years, due to the extraordinary properties of metamaterials [177], metamaterial (MTM) based absorbers have drawn the attention of many research groups [178].

Landy *et al.*, presented one of the first metamaterial based absorber [7]. Metamaterial absorbers can be made compact and ultrathin due to their sub-wavelength nature [179–181]. They can provide near unity absorption over different frequency ranges. Multiple scaled versions of same geometry [182, 183] or different geometries [184, 185] can be combined to provide multiband and broadband [179] characteristics. Several metamaterial based absorbers have been proposed till date for different frequency bands such as microwave, terahertz [182, 183], mm for different applications such as radar [186], solar cell, photodetector, electromagnetic interference (EMI)/ electromagnetic compatibility(EMC) applications [187] etc. Metamaterial absorbers have been extensively investigated for improving their characteristics in terms of polarization sensitivity, oblique incidence, bandwidth enhancement and size reduction.

Although, extensive research has been done on metamaterial absorbers but achieving multiband characteristics with high absorptivity using single compact size structure is still rare and requires large area [186]. The paper presents a novel ultrathin metamaterial absorber with compact size unit cell of dimensions $10 \times 10 \times 1 mm^3$. The structure exhibit resonance at five distinct frequencies lying in S-, C-, X- and Ku-bands with absorption peaks at 3.35 GHz, 5.1 GHz, 9.5 GHz, 11.55 GHz and 16.9 GHz providing absorptivity of 99.59%, 95.49%, 97.5%, 99.25% and 93.89% respectively. Five bands with full width at half maxima (FWHM) bandwidth of 110 MHz (3.3-3.41 GHz), 210 MHz (4.98-5.19 GHz), 310 MHz (9.32-9.63 GHz), 340 MHz (11.37-11.71 GHz) and 440 MHz (16.68-17.12 GHz) are achieved by integrating three compact geometries on the same structure. Finally, the unit cell is arranged periodically in the form of a 2-D array of size 20×20 and fabricated on an FR-4 substrate of size 200×200 mm² with complete copper lamination on the back side, thereafter, measurements are performed inside anechoic chamber. All the design and simulations are done using Ansys High frequency structure simulator (HFSS) [188].

In the following section, the design evolution of the proposed absorber structure is illustrated.

5.1.2 Design and Simulation Approach

The unit cell of the proposed metamaterial absorber is designed on a low cost FR-4 dielectric substrate with dielectric-constant (ε_r) of 4.4 and loss-tangent (δ) of 0.02. The thickness of the substrate is 1 mm which corresponds to $\lambda/17.75$ where λ is the wavelength corresponding to the maximum resonant frequency of absorption. Top of the substrate consists of metallic patch with copper ($\sigma = 5.8 \times 10^7 S/m$) laminated ground plane on the bottom. The top layer is a combination of three geometries i.e. outer square ring, middle circular split ring with a square ring attached inside and an inner square ring shown as Design I, II and III respectively in Fig. 5.1. All the three geometries exhibit resonances at different frequencies (as shown in Fig. 5.2). The top view of proposed unit cell configuration is shown in Fig. 5.1 Design IV. The optimized geometrical dimensions of the final structure is given in Table 5.1. The absorber unit cell has a compact dimension of $0.11\lambda_0 \times 0.11\lambda_0$, where λ_0 is the lowest absorption peak wavelength.

The unit cell is simulated under periodic boundary conditions by applying master-slave boundaries in Ansys HFSS as shown in Fig. 5.3. The unit cell is excited using floquet ports

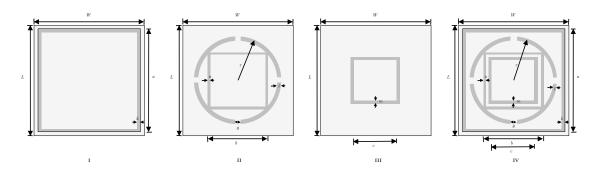


Figure 5.1: Top view of unit cell geometry of (a) Case I (b) Case II (c) Case III (d) Case IV.

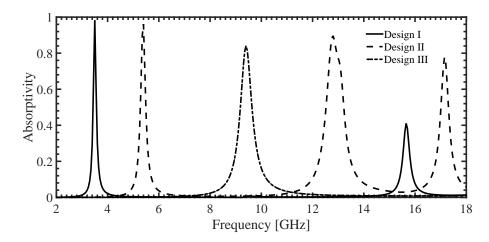


Figure 5.2: Simulated absorptivity of three structures, Case I (-Solid line), Case II (-dashed line) and Case III (.-dot dashed line).

providing electric and magnetic field along x and y axis and propagation vector (k) along z axis. The absorptivity $A(\omega)$ is obtained using Eq. 5.1

$$A(\omega) = 1 - |S_{11}(\omega)|^2 - |S_{21}(\omega)|^2$$
(5.1)

Where, $|S_{11}(\omega)|^2$ and $|S_{21}(\omega)|^2$ represents the reflectivity and transitivity respectively with respect to frequency ω . Considering, the bottom of the substrate is completely coated with copper having thickness of $0.35\mu m$ which is greater than the skin depth of copper at all the absorption frequencies, so further propagation of wave is restricted which indicates zero transmission, thus, $|S_{21}(\omega)|^2=0$. Therefore, Eq. 5.1 reduces to

$$A(\omega) = 1 - |S_{11}(\omega)|^2 \tag{5.2}$$

Table 5.1: Design parameters of the proposed unit cell

Parameters	Unit (mm)	Parameters	Unit (mm)	
W	10	L	10	
a	9.6	k	0.3	
b	5.8	1	0.35	
с	5	m	0.25	
g	0.5	n	0.15	
r	4.3			

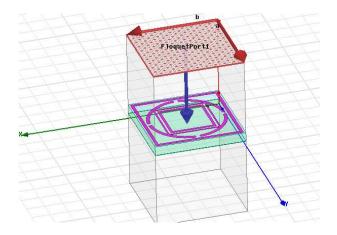


Figure 5.3: Simulation set up of unit cell in HFSS.

Thus, in order to obtain near unity absorption, Reflected power from the unit cell has to be minimized. The origination of all the five absorption peaks is well discussed in the following sections.

Case I: Outer square ring

Fig. 5.1(Design I) shows the unit cell comprising only the outer square ring. The optimised dimensions of the ring are given in Table 5.1. The structure is illuminated by a normal incident electromagnetic wave and absorptivity is obtained as shown in Fig. 5.2 (-solid lines). It is observed that this simple square geometry provides strong resonance with absorptivity of 98.25% at 3.5 GHz belonging to S-band along with a weak higher order resonance at 15.65 GHz belonging to Ku-band.

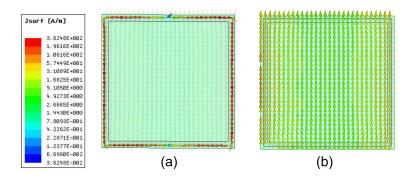


Figure 5.4: Current density plot on top and bottom surfaces of Case I unit cell at 3.35 GHz.

The current density plot for both top and bottom surfaces is depicted in Fig. 5.4(a) and (b) respectively. It is observed that left and right edges of the square ring provide surface current which is anti-parallel to the current at the bottom copper surface. This generates circulation current perpendicular to the applied magnetic field (horizontal direction), thus producing magnetic excitation in the design.

Case II: Circular split ring with square ring attached inside

The middle portion of final geometry comprises of a thin square ring attached inside a circular ring loaded with four symmetrical splits, shown in Fig. 5.1(Design II). The dimensions are given in Table 5.1. This unit cell is also simulated using periodic boundaries and absorptivity is obtained as a function of frequency shown in Fig. 5.2(- -dashed line). Three absorption peaks are obtained at 5.4 GHz, 12.8 GHz and 17.15 GHz belonging to C- and Ku-bands, with absorptivity 96.11%, 89.63% and 77.88% respectively.

Fig. 5.5 shows the surface current density plot on both top and bottom plane for all the three absorption peaks. Anti-parallel current density between top and bottom plane can be observed here also. It is also seen that different portions of the design are responsible for resonance at different frequencies. At 5.4 GHz, concentration of current is more on the left and right arm of the inner connected square ring, whereas at 12.8 GHz and 17.15 GHz, concentration of current is more on the corners and top bottom arms respectively.

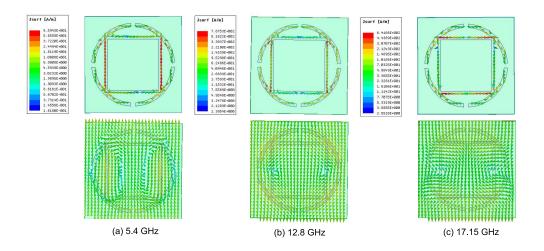


Figure 5.5: Current density plot on top and bottom surfaces of Case II unit cell at (a) 5.4 GHz, (b) 12.8 GHz, (c) 17.15 GHz..

Case III: Inner square ring

Fig. 5.1(Design III) shows a small square ring geometry providing absorption peak at 9.4 GHz lying in the X-band with absorptivity 88.34%. Fig. 5.6 indicates the current density distribution on top and bottom surface at the resonant frequency. It also shows anti-parallel current densities, thus showing magnetic resonance.

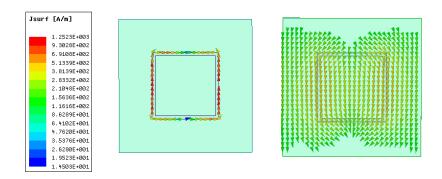


Figure 5.6: Current density plot on top and bottom surfaces of Case III unit cell at 9.4 GHz..

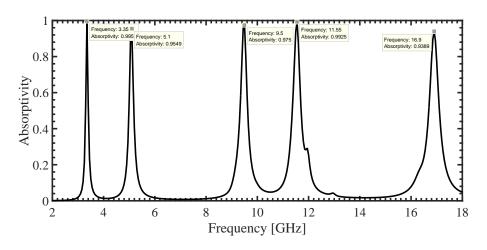


Figure 5.7: Absorptivity of final unit cell geometry (Case IV).

Case IV: Proposed final structure

Fig. 5.1(Design IV) shows the final structure of proposed metamaterial absorber which is obtained by integration of the three simple geometries discussed earlier. The optimised dimensions are given in Table 5.1. The design is simulated using periodic boundary conditions and absorptivity is obtained using S-parameters, as shown in Fig. 5.7. It shows absorptivity greater than 90% for five different frequencies, lowest one lying in S-band, second lying in C-band, third lying in X-band and highest two lying in Ku-band. The enhancement in absorption along with slight variation in the resonance peaks of the final geometry (shown in Fig. 5.7) as compared to the individual geometries (Fig. 5.2) is due to the mutual coupling between them.

The structure in Fig. 5.8 shows the surface current density for the five peak absorption frequencies. It can be seen that different regions of the designed structure are being excited by different frequencies. At 3.35 GHz, the current density is maximum on the outer square ring (Fig. 5.8(a)), at 5.1 GHz, it is maximum on the square ring attached to the split ring (Fig. 5.8(b)), whereas at 9.5 GHz, it is on the inner square ring (Fig. 5.8(c)). At 11.55 GHz and 16.9 GHz, most of the current density is concentrated on the middle geometry i.e. the split ring with square ring attached inside (Fig. 5.8(d),(e)). Therefore, the whole discussion for the integrated geometry fairly compliments the discussion made for individual geometries earlier.

Fig. 5.9 shows the electric field distribution of the final geometry. It shows that the induced

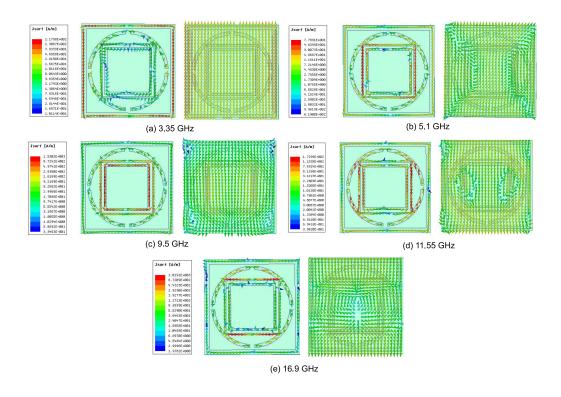


Figure 5.8: Current density plot on top and bottom surfaces of Case IV unit cell at (a) 3.35 GHz, (b) 5.1 GHz, (c) 9.5 GHz, (d) 11.55 GHz, (e) 16.9 GHz.

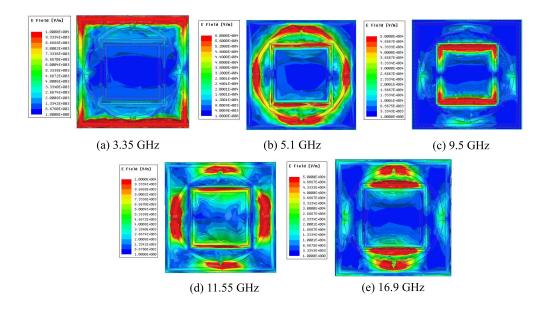


Figure 5.9: Electric field distribution plot of the proposed unit cell at the absorption frequencies.

electric field is highly concentrated along the direction of incident electric field (vertical direction in Fig. 5.9). This gives rise to electric excitation in the design. Thus the combination of electric and magnetic excitations result in strong magnetic absorption at 3.35 GHz, 5.1 GHz, 9.5 GHz, 11.55 GHz and 16.9 GHz. Furthermore, an important observation can be made from the surface current and electric field distribution plot at 16.9 GHz that the current loops are not prominent in the direction perpendicular to incident magnetic field (horizontal direction), however, a strong electric field do exist in the direction of incident electric field (vertical direction). Therefore, it can be concluded that the absorptivity at 16.9 GHz is observed as a result of electric coupling between the two geometries (inner square ring and outer circular split ring) of Design II of Fig. 5.1.

The next section discusses the equivalent circuit of the final absorber geometry in order to study the electrical behaviour of the structure.

5.1.3 Equivalent circuit analysis

To further analyse the absorption characteristics of the proposed metamaterial structure, an equivalent circuit model is presented in Fig. 5.10. Each resonance can be modelled as an equivalent RLC network based on the current density shown in Fig. 5.8, which is connected in parallel with a transmission line section indicating dielectric losses, terminated to ground. Due to the presence of copper laminated ground plane, the circuit is analysed as a single port network. The presence of current on the structure is modelled as inductor whereas the gaps are modelled as capacitors. The resistances represent the losses in the structure [189].

The network L_1 , R_1 indicates the equivalent model for the Case I which exhibits the lowest resonant frequency i.e 3.35 GHz. L_1 is the equivalent inductance arising due to the current propagating in the square ring by two paths, in the direction of applied electric field, as shown in Fig. 5.8(a). The capacitance between the two unit cells is represented by C_1 . The network in the dotted box represent the RLC equivalent for the middle geometry i.e Case II. The middle geometry is responsible for absorption at three distinct peaks i.e. 5.1 GHz, 11.55 GHz and

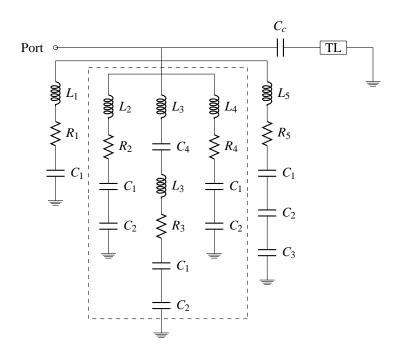


Figure 5.10: Equivalent circuit of the proposed metamaterial absorber.

16.9 GHz, which is depicted from the current density plot in Fig. 5.8. From the Fig. 5.8(b) it can be observed that the current first originates from the outer split ring then enters the left and right arm of the square ring and then again enters the outer split ring. In this case the current follows an uninterrupted path so it can be represented as an inductor L_2 . Now, at 11.55 GHz, the conduction current flows in the outer ring followed by displacement current due to the gap and then again the conduction current due to the arm of the outer ring (Fig. 5.8(d)). This results in an LC equivalent $2L_3$ and C_4 . C_2 is the capacitance between the middle and outer geometry. The inductance L_4 is due to the current in the square ring of middle geometry at 16.9 GHz (Fig. 5.8(e)). Further, at 9.5 GHz, the current is dominant on the inner square i.e. Case III (Fig. 5.8(c)), which is represented as the inductance L_5 . The capacitance C_3 is due to the coupling between inner and middle geometry. Finally, the circuit is simulated using Advanced Design System (ADS) and the parameters are optimized using curve fitting tool.

5.1.4 Results and Discussion

The final structure is simulated and results are obtained (Fig. 5.7). The simulated FWHM bandwidth, peak absorption frequencies along with the absorptivity obtained is indicated in Table 5.2.

Table 5.2: Simulated result of Proposed Unit cell

Peak Absorption	Absorptivity	FWHM	Frequency
frequncy (GHz)	(%)	Bandwidth	Band
3.35	99.59	110 MHz (3.3-3.41 GHz)	S-band
5.1	95.49	210 MHz (4.98-5.19 GHz)	C-band
9.5	97.5	310 MHz (9.32-9.63 GHz)	X-band
11.55	99.25	340 MHz (11.37-11.71 GHz)	Ku-band
16.9	93.89	440 MHz (16.68-17.12 GHz)	Ku-band

The equivalent circuit parameters obtained using curve fitting tool in ADS are given in table 5.3 and the response obtained after circuit simulation in shown in Fig. 5.11. It can be seen that the reflection coefficient obtained due to circuit simulation matches well with the structure response.

Table 5.3: Equivalent Circuit Parameters.

1401C 3.3. L	rable 3.3. Equivalent Chedit I diameters.							
Resistance (Ω)	Capacitance (fF)	Inductance (nH)						
$R_1 = 40$	$C_1 = 182.17$	$L_1=13.63$						
$R_2 = 50$	$C_2 = 165.02$	$L_2 = 11.8$						
$R_3 = 11.5$	$C_3 = 130.71$	$L_3=3.03$						
$R_4 = 5.8$	$C_4 = 360$	$L_4=1.15$						
$R_5 = 12$	$C_c = 280$	$L_5=5.75$						

To validate the operation of the proposed metamaterial absorber, material parameter such as effective permittivity (ε_{eff}), effective permeability (μ_{eff}) and normalised impedance are also studied. Furthermore, the effect of changing the polarization and angle of incident wave on the structure is also discussed in the following sections. Finally, a comparative analysis is given with previously reported absorbers.

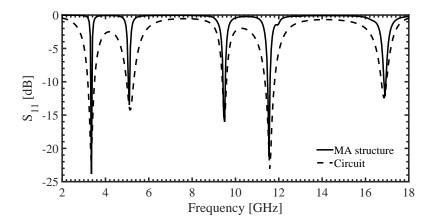


Figure 5.11: Reflection coefficient response due to circuit and design simulation.

Extraction of Material Parameters

Metasurfaces are better described in terms of surface susceptibilities, therefore, electric (χ_{es}) and magnetic susceptibilities (χ_{ms}) are obtained using the simulated reflection coefficient (S_{11}) given in Eq. 5.3, 5.4. Since, there exists a relation between χ_{es} (or χ_{ms}) and ε_{eff} (or μ_{eff}) [190] so, using the values of susceptibilities i.e. χ_{es} and χ_{ms} , effective material parameters i.e. ε_{eff} and μ_{eff} are obtained (Eq. 5.5,5.6).

$$\chi_{es} = 1 + \frac{2j}{k_0} \frac{S_{11-1}}{S_{11}+1} \tag{5.3}$$

$$\chi_{ms} = 1 + \frac{2j}{k_0} \frac{S_{11} + 1}{S_{11} - 1} \tag{5.4}$$

$$\varepsilon_{eff} = 1 + \frac{\chi_{es}}{d} \tag{5.5}$$

$$\mu_{eff} = 1 + \frac{\chi_{ms}}{d} \tag{5.6}$$

Fig. 5.12(a) and 5.12(b) shows the variation of real and imaginary part of ε_{eff} and μ_{eff} respectively with respect to frequency. Table 5.4 shows the values of each parameter at the absorption peaks and it is observed that the values of ε_{eff} and μ_{eff} is nearly equal which is the condition for a nearly perfect absorber. The reflectivity (R) from a medium for a normally incident electromagnetic wave is given by Eq. 5.7.

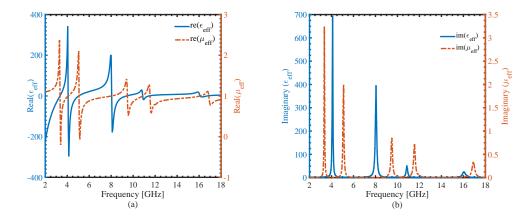


Figure 5.12: (a) Variation of (a) real value and (b) imaginary value of effective permittivity and permeability with respect to frequency.

$$R = \left| \frac{\mu_{eff} - n}{\mu_{eff} + n} \right|^2 \tag{5.7}$$

where, n is the refractive index of medium given by $\sqrt{\mu_{eff} \varepsilon_{eff}}$. When ε_{eff} and μ_{eff} are equal, reflectivity (R) is ideally zero.

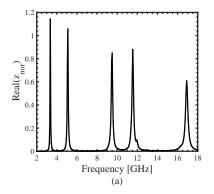
Further, normalized impedance of the absorber is also analysed, based on the relation given in Eq. 5.8 [191]

$$S_{11} = \frac{Z(\omega) - \eta_0}{Z(\omega) + \eta_0}$$
 (5.8)

Since, to have minimum reflections i.e. $S_{11} = 0$, the input impedance of the structure should be matched to impedance of free space (η_0). Fig. 5.13(a) and (b) respectively show that the real value of normalized input impedance for all the five absorption peaks is nearly equivalent to 1 and imaginary part is close to 0, as given in Table. 5.4, thus obtaining minimum reflections and maximum absorptivity.

Table 5.4: Values of retrieved parameters with respect to absorption peaks

Frequency	$\mathbf{Re}(\varepsilon_{eff})$	$\mathbf{Re}(\mu_{eff})$	$\operatorname{Im}(\varepsilon_{eff})$	$\mathbf{Im}(\mu_{eff})$	$\mathbf{Re}(z_{nor})$	$\mathbf{Im}(z_{nor})$
(GHz)						
3.35	1.025	0.9676	2.507	3.241	1.143	-0.0206
5.1	1.625	0.818	1.499	1.992	1.057	-0.35
9.5	1.324	0.745	1.086	0.854	0.86	-0.19
11.55	1.121	0.903	0.918	0.732	0.88	-0.108
16.9	1.108	0.959	0.916	0.344	0.62	-0.07



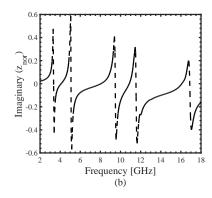


Figure 5.13: (a) Variation of (a) real value and (b) imaginary value of normalized impedance with respect to frequency.

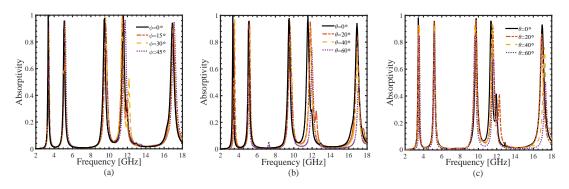


Figure 5.14: Simulated absorptivity response of structure under (a) various polarization angles (b)oblique incidence for TE polarization (c) oblique incidence for TM polarization .

Analysis for different polarization angles and oblique incidence

The structure is investigated for different angles of polarization (ϕ), as shown in Fig. 5.14(a). Due to the four-fold symmetry of the structure, the study is carried out only up to 45° of polarization angle. It was observed that the absorptivity obtained for all the angles is almost similar to the normal incidence case. Therefore, it can be seen that the suggested metamaterial absorber is insensitive to polarization.

Practically, electromagnetic waves are obliquely incident on the absorber so it is necessary that the designed structure is investigated for different angles of incidence (θ) of the EM wave for both TE and TM polarization. For TE polarization, the electric field vector is kept fixed and the magnetic field vector is rotated from 0° to 60° whereas, in case of TM polarization reverse approach is followed. The results shown in Fig. 5.14(b) and 5.14(c) illustrated that varying

the angle of incidence from 0° to 60° for both TE and TM polarization does not effect the resonant frequencies significantly. However, absorptivity tends to reduce at higher frequency bands due to increased mismatch with the free space.

Comparative Analysis

Table 5.5 gives a comparative analysis of the proposed metamaterial based absorbers with other previously reported metamaterial absorbers. The proposed absorber provides high absorptivity over five different frequencies using a compact, simple and symmetrical geometrical configuration.

5.1.5 Experimental Results and Discussion

Finally, the proposed metamaterial absorber is fabricated on a $200 \times 200 \times 1 mm^3$ FR-4 substrate consisting of 20×20 array of periodically arranged unit cells with copper laminated on the bottom side. The fabricated prototype is shown in Fig. 5.15. The measurements are carried out inside the anechoic chamber using Anritsu MS2038C vector network analyser which was initially calibrated using full 2-port calibration method. The free space reflection method was used to obtain the reflection coefficient of the fabricated structure. Fig. 5.16 shows the experimental setup to carry out the measurement. The metamaterial absorber sample is fixed on a Styrofoam box inside a microwave anechoic chamber. Two horn antennas capable to generate 1-18 GHz linearly polarized wave, one operating as transmitter and other as receiver, are placed in front of the absorber. The distance (d) between antennas and sample is kept approximately 1.5 m to meet the far-field condition, given by eq. 5.9.

$$d > \frac{2D^2}{\lambda} \tag{5.9}$$

where λ is the shortest operating wavelength and D is the diagonal length of the antennas. The transmitting horn impinges the electromagnetic wave and the receiving horn captures the

129

Table 5.5: Comparative analysis of proposed absorber with previously proposed ones

Ref.	Unit cell size	Unit cell size corresponding	No. of	Frequency of	Peak Absorptivity (%)	FWHM (MHz)
	(mm^2)	to lowest frequency (λ_0)	bands	absorption peaks (GHz)		
[187]	12×12×1	0.136×0.136×0.011	Four	3.4, 8.23, 9.89, 11.80	97.02, 94.07, 91.72, 98.2	160, 280, 300, 520
[181]	$8\times8\times0.8$	$0.11 \times 0.11 \times 0.011$	Three	4.19, 9.34, 11.84	99.67, 9948, 99.42	170, 350, 480
[184]	10×10×1	$0.122 \times 0.122 \times 0.0122$	Four	3.68, 8.58, 10.17, 14.93	96.15, 99.17, 99.75, 98.75	-
[185]	23×23×1	-	Four	3.91, 5.16, 7.10, 9.16	99.35, 98.04, 99.85, 99.78	-
[186]	14×14×1	$0.159 \times 0.159 \times 0.011$	Five	3.4, 8.34, 9.46, 14.44, 16.52	98.6, 96.6, 90.1, 97.8, 93.1	-
[192]	13.8×13.8×1	$0.2024 \times 0.2024 \times 0.0147$	Three	4.4, 6.2, 14.2	95.13, 97.41, 97.36	-
[193]	9.87×8.82×1	$0.19 \times 0.17 \times 0.019$	Three	5.8, 9.52, 11.97	96, 99, 95	-
[194]	24×24×1.6	$0.68 \times 0.68 \times 0.045$	Three	8.6, 10.2, 11.95	100, 93 and 83	-
Proposed	10×10×1	$0.11 \times 0.11 \times 0.011$	Five	3.35, 5.1, 9.5, 11.55, 16.9	99.59, 95.49, 97.5, 99.25, 93.89	110, 210, 310, 340, 440

reflections from the absorber sample. The scattering parameters are observed on the Anritsu MS2038C vector network analyser connected to the pair of horn antennas. The reflections

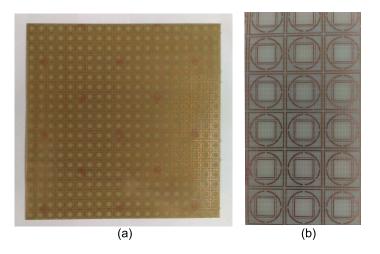


Figure 5.15: (a) Fabricated sample of proposed structure with its enlarged portion shown in (b).

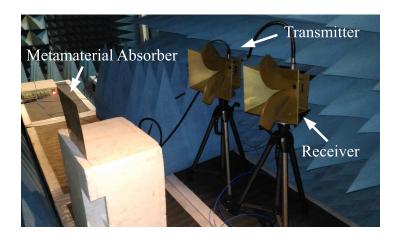


Figure 5.16: Experimental environment for measurement of proposed absorber.

obtained from the absorber are subtracted from the reflections obtained from copper sheet with the size same as that of the proposed absorber keeping its position inside the anechoic chamber unchanged. This is done in order to measure the actual reflections from the absorber by cancelling the effect of scattering losses, diffraction losses, edge reflections, etc.

Fig. 5.17 shows the measured reflections from the background, copper sheet and the ab-

sorber along with the actual reflections obtained from the proposed structure. Finally, the comparison of measured and simulated absorptivity is shown in Fig 5.18. The absorption peaks are fairly matched, however, incorporating out of band mismatches which are arising due to fabrication limitations and cable losses. The mismatch is more prominent at the higher frequencies which is due to the losses of horn antennas used for measurement.

The structure shows measured absorption peaks at 3.75 GHz, 4.98 GHz, 9.5 GHz, 12.2 GHz and 16.8 GHz with absorptivity of 94.75%, 92.76%, 95.43%, 99.86 %, and 96.86 % respectively. The measured FWHM bandwidth at the five operating frequencies are 126 MHz (3.66-3.786 GHz), 170 MHz (4.903-5.073 GHz), 489 MHz (9.204-9.693 GHz), 1.05 GHz (11.92-12.97 GHz), and 520 MHz (16.5-17.02 GHz).

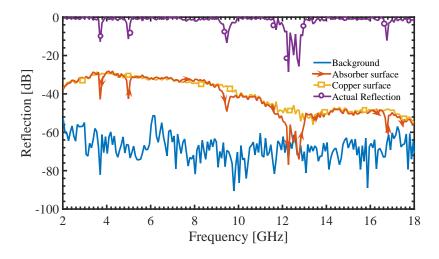


Figure 5.17: Measured reflections from the proposed metamaterial absorber.

5.1.6 Summary

The proposed ultra thin metamaterial based absorber exhibits penta-band behaviour despite the compact geometry of the unit cell. The penta-band obtained are as a result of the three simple geometries combined on a single $10 \times 10 mm^2$ FR-4 substrate. The dimensions of each geometry are optimised in order to obtain nearly perfect impedance matching and provide absorptivity greater than 90% for five bands lying in four different microwave bands i.e. S, C, X, Ku-band. The structure provides simulated absorption peaks at 3.35 GHz, 5.1 GHz,

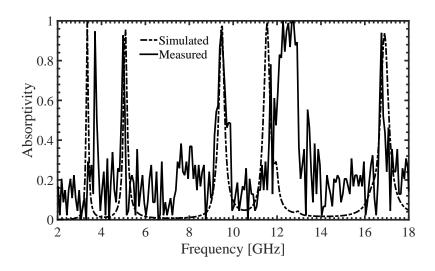


Figure 5.18: Measured and simulated absorptivity of proposed metamaterial absorber.

9.5 GHz, 11.55 GHz and 16.9 GHz with absorptivity 99.59%, 95.49%, 97.5%, 99.25% and 93.89% respectively. Further more, the four-fold symmetry of the structure enable polarization insensitivity and high absorption over different angle of incidence of electromagnetic wave for TE and TM polarization. The measured results shows absorption peaks at 3.75 GHz, 4.98 GHz, 9.5 GHz, 12.2 GHz and 16.8 GHz with absorptivity of 94.75%, 92.76%, 95.43%, 99.86%, and 96.86% respectively. A mismatch between measured and simulated results at high frequencies was mainly observed due losses in horn antenna. Radar cross section reduction can be done through the proposed metamaterial absorber. Also, it can be used in other FCC-defined airborne applications.

The next section presents a simpler metamaterial absorber geometry i.e. a closed meander line shaped metamaterial absorber operating at 3.5 GHz.

5.2 DESIGN AND ANALYSIS OF METAMATRIAL ABSORBER AT 3.5 GHZ US-ING EQUIVALENT CIRCUIT MODEL

This section of the chapter demonstrates a closed meander line shaped metamaterial absorber operation at 3.5 GHz WiMAX band. The proposed metamaterial absorber unit cell has a compact size of $0.11\lambda_0 \times 0.11\lambda_0$ design on an ultrathin FR-4 substrate with thickness $0.018\lambda_0$,

where λ_0 is the wavelength corresponding to operating frequency. The proposed absorber shows an absorptivity of 98.5 % at the intended frequency. The design is evolved from a simple square loop to a symmetrical meander line structure whose dimensions are optimized to operate at 3.5 GHz WiMAX band. An equivalent circuit model is also defined to depict the electrical properties of the structure. The proposed design also shows insensitivity to polarization as well as change in incident angle of the wave over a wide-angle (upto 60°) for both TE and TM polarization. The proposed structure is a good candidate for radar cross section reduction of an antenna.

5.2.1 Design and Simulation Approach

The proposed meander line shaped metamaterial absorber is designed on a 1.6 mm thick FR-4 substrate, having dielectric-constant (ε_r) of 4.4 and loss-tangent (δ) of 0.02, with unit cell dimensions of 10mm×10mm, as shown in Fig. 5.19. The top of the substrate consists of the closed meander line shape and bottom is completely laminated with copper. The design

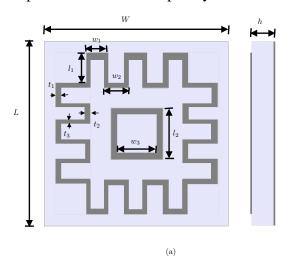


Figure 5.19: Top view (a) and side view (b) of the proposed unit cell.

parameters are given in table. 5.6.

The unit cell is simulated under periodic boundary conditions by applying master-slave boundaries in Ansys HFSS. The unit cell is excited using floquet ports providing electric and magnetic field along x and y axis and propagation vector (k) along z axis.

Table 5.6: Design parameters of proposed unit cell

Parameters	W	L	w_1	w_2	w ₃	l_1	l_2	t_1	t_2	t ₃	h
Unit (mm)	10	10	1.25	1.025	2.1	2.1	2.7	0.425	0.35	0.2	1.6

The absorptivity $A(\omega)$ is obtained using Eq. 5.10

$$A(\omega) = 1 - |S_{11}(\omega)|^2 - |S_{21}(\omega)|^2$$
(5.10)

Where, $|S_{11}(\omega)|^2$ and $|S_{21}(\omega)|^2$ represents the reflectivity and transitivity respectively with respect to frequency ω . Considering, the bottom of the substrate is completely coated with copper having thickness of $0.35\mu m$ which is greater than the skin depth of copper at all the absorption frequencies, so further propagation of wave is restricted which indicates zero transmission, thus, $|S_{21}(\omega)|^2=0$. Therefore, Eq. 5.10 reduces to

$$A(\omega) = 1 - |S_{11}(\omega)|^2 \tag{5.11}$$

Thus, in order to obtain near unity absorption, Reflected power from the unit cell has to be minimized. To minimize the reflections, the impedance matching of the free space with the structure is required. Since [127],

$$S_{11} = \frac{Z(\omega) - \eta_0}{Z(\omega) + \eta_0} \tag{5.12}$$

where, $Z\omega$ is the input impedance if the absorber and η_0 is the free space impedance. Fig. 5.20 depicts the stepwise evolution of the proposed unit cell. The Case I is a simple rectangular geometry which resulted in a weak absorption at 3.85 GHz. Now,in case II a meander line structure is created with 4 vertical lines on each arm of the rectangle within the same area. This resulted in an increase in the absorptivity however, operating frequency is shifted to 4 GHz. Further increasing the number of vertical lines (Case III), the absorption frequency is shifted to lower side at 3.5 GHz, due to increase in effective length of the path covered by

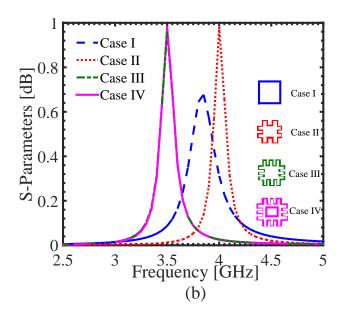


Figure 5.20: Stepwise evolution of the proposed unit cell.

surface current. The absorptivity obtained for this case is 96 %. Finally, on adding a small rectangular loop in the middle of the geometry resulted in increase in absorptivity to 98.5 % due to improved electromagnetic coupling. The final geometry resulted in the miniaturization of structure by 1.2 times.

5.2.2 Results and Discussion

The final meander line structure is simulated using periodic boundary conditions and results are obtained, shown in Fig. 5.20. The absorptivity obtained is 98.5 % at 3.5 GHz. Fig. 5.21 shows the normalized impedance of the structure. Since, at 3.5 GHz, the normalized impedance of the structure is close to unity, the reflections from the structure are minimized, as per eqn. 5.12, giving near perfect absorption. Now, for perfect impedance matching it is required that the material parameters i.e. relative permittivity (ε_r) and permeability (μ_r) of the structure must be equal, since,

$$Z_0 = \sqrt{\frac{\mu_r}{\varepsilon_r}} \tag{5.13}$$

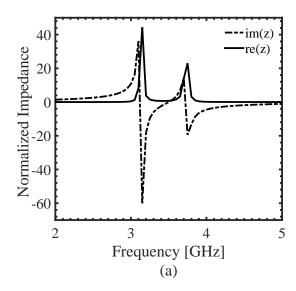


Figure 5.21: Normalized impedance of the proposed unit cell.

Therefore, if μ_r is nearly equal to ε_r , the input impedance of the structure matches to the free space impedance and the reflections are minimized. Fig. 5.22 shows the extracted material parameters of the proposed absorber and it is found that μ_r =1.001 and ε_r =0.68 which are nearly equal, obtaining good amount of impedance matching.

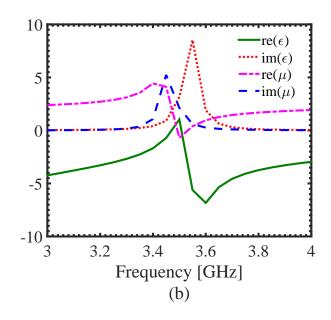


Figure 5.22: Material parameters of the proposed unit cell.

Fig. 5.23 shows the surface current distribution at 3.5 GHz on top and bottom of the struc-

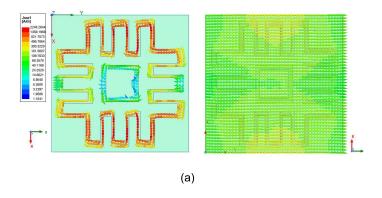


Figure 5.23: Surface Current distribution of the proposed unit cell (a)Top, (b) Bottom.

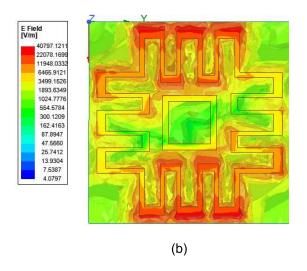


Figure 5.24: E-field distribution of the proposed unit cell.

ture. It can be observed that the net direction of propagation of current on the upper and lower part of the geometry is from positive y axis to negative y axis and on the bottom, it is from negative y to positive y axis. Thus, the current on top and bottom surfaces are anti-parallel to each other resulting in the formation of magnetic dipole in the direction perpendicular to the applied magnetic field. Now, Fig. 5.24 shows the electric field distribution on the structure at 3.5 GHz. It shows that the induced electric field is highly concentrated along the direction of incident electric field (horizontal direction in Fig. 5.24). This gives rise to electric excitation in the design. Thus, we can conclude that, at 3.5 GHz, electromagnetic excitation takes place which results in absorption of wave at that frequency. The following section proposes the

equivalent circuit for the meander line absorber structure followed by analysis of polarization insensitivity and oblique incidence.

Equivalent circuit analysis

To study the electrical behaviour of the structure it is necessary to extract the lumped equivalent circuit model of the structure, depicted in Fig. 5.25. It can be observed from Fig. 5.23(a) that at 3.5 GHz, the flow of the current is from +y axis to -y axis, which is the direction of applied electric field, on the upper and lower half of the meander line geometry. Therefore, this can be represented as an equivalent inductor (L_1). The capacitor C_1 is the net coupling capacitance between the adjacent unit cells and the two geometries (meander line and inner square). The resistance R_1 represents losses in the structure. The structure is treated as single port circuit since there is no transmission from top to bottom of the structure, also, the RLC equivalent of the top geometry is terminated to ground plane through a transmission line equivalent of the dielectric substrate.

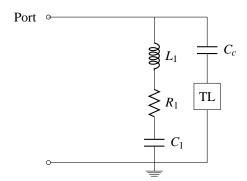


Figure 5.25: Equivalent circuit of the proposed metamaterial absorber.

Finally, the circuit is simulated using Advanced Design System (ADS) and the parameters are optimized using curve fitting tool. The equivalent circuit parameters obtained after optimization are: L_1 = 75 nH, C_1 = 27.8 fF, C_c = 250 fF and R_1 = 57 Ω . Fig. 5.26 shows a comparison of the reflection coefficient obtained after simulating the proposed unit cell and its equivalent circuit model. It can be observed that the circuit is a close approximate model

of the proposed metamaterial unit cell.

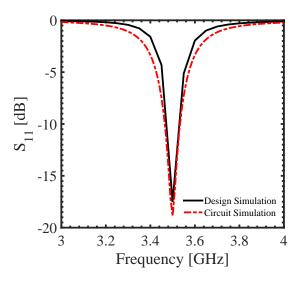


Figure 5.26: Simulated reflection coefficient of the proposed unit cell and its equivalent circuit model.

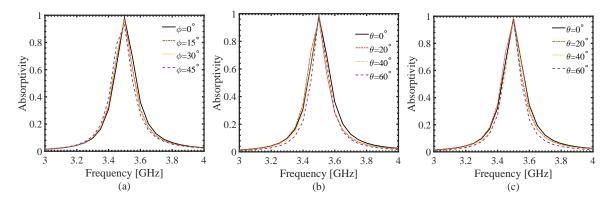


Figure 5.27: Simulated absorptivity response of structure under (a) various polarization angles (b)oblique incidence for TE polarization (c) oblique incidence for TM polarization.

Insensitivity to polarization and oblique incidence

Further, the structure is analysed for different polarization angles (Fig. 5.27(a)) as well as different angle of incidences of the incident wave for both TE (Fig. 5.27(b)) and TM modes(Fig. 5.27(c)). The variation in angle of polarization (ϕ) is observed upto 45° due to the symmetrical geometry of the unit cell and it was found that the absorptivity does not vary with variation in polarization, thus, the structure is said to be polarization insensitive. Furthermore, the performance of the absorber is tested in terms of oblique incidence (θ) upto 60° angle for both

Table 5.7: Comparative analysis of proposed absorber with previously proposed ones

Ref.	Unit cell	Unit cell size	Unit cell size corresponding	Absorption	Absorptivity
		(mm^2)	to center frequency (λ_0)	Frequency(GHz)	(%)
[7]	Electric Ring Resonator (ERR)	4.2×12×0.72	0.16×0.46×0.027	11.65	96
[76]	Electric field coupled LC (ELC)	14×21.5×1	$0.46 \times 0.71 \times 0.033$	9.92	96.7
[79]	Square loop	10×10×1	$0.2 \times 0.2 \times 0.02$	6.14	-
[80]	Snowflake	22.86×12.16×0.8	$0.85 \times 0.38 \times 0.03$	11.28	99.5
[81]	Symmetric structure	$7 \times 7 \times 0.7$	$0.2 \times 0.2 \times 0.02$	8.65	99.6
Proposed	Meander line	10×10×1	$\textbf{0.11}{\times}\textbf{0.11}{\times}\textbf{0.018}$	3.5	98.7

TE and TM modes. No significant change in the absorptivity as well as resonant frequency was observed.

Comparative Analysis

Table 5.7 gives a comparative analysis of the proposed absorber structure with previously proposed narrow band absorbers.

It can be observed that the proposed design is smaller in size and thickness as compared to previously proposed narrow band absorbers. Moreover, there is a size reduction of 1.8 times as compared to the conventional square loop structure [75] and thickness is also reduced by 1.1 times which is due to increase in the effective length of the proposed meander line structure.

5.2.3 Summary

A novel metamaterial based absorber is designed for 3.5 GHz WiMAX band application. The structure was designed to have an absorptivity of 98.5 % on the intended band. A closed meander line geometry is used to fulfil the purpose. The structure is analysed using equivalent circuit model. Also, it was observed that the structure is independent to change in polarization angle and change in angle of incidence of the incident wave. The proposed metamaterial absorber can be used for radar cross section reduction of an antenna.

After studying the basic design principle of metamaterial absorber, in the next chapter, the application of novel metamaterial absorber is investigated for mutual coupling reduction between two antennas in a 2-element MIMO system.

CHAPTER 6

ISOLATION IMPROVEMENT OF MIMO ANTENNA USING A NOVEL FLOWER SHAPED METAMATERIAL ABSORBER AT 5.5 GHZ WIMAX BAND

Contents of this chapter are published as:

Priyanka Garg and Priyanka Jain, "Isolation Improvement of MIMO Antenna Using a Novel Flower Shaped Metamaterial Absorber at 5.5 GHz WiMAX Band," *IEEE Transactions on Circuits and Systems II: Express Briefs*, vol. 67, no. 4, pp. 675-679, April 2020.

Use of MIMO (multiple-input-multiple-output) antennas has increased in modern wireless communication systems as they offer significant improvement in link range as well as data throughput within the available bandwidth and power [195, 196]. Due to increased demand of miniaturization, mutual coupling reduction in MIMO antenna systems is the major issue of concern. Various techniques are available in literature to overcome this problem [197, 198]. In [197], a T-shaped stub is introduced in the ground plane to improve the isolation in UWB MIMO antenna system, whereas a carbon film is proposed in [198] which could absorb the interference between the antennas.

Metamaterial are the artificial structures that are being extensively used to improve the characteristics of various microwave components [199]. In this paper, the use of metamaterial based absorber for mutual coupling reduction in MIMO antenna has been explored. Metamaterial absorber was introduced by Landy *et al.* [200] in 2008. Such devices can start to resonate over a certain frequency range when an electromagnetic waves is incident upon them achieving near unity or so-called "perfect" absorption [201]. Such metamaterial absorbers are being utilized for several applications such as radar cross section (RCS) reduction [202], energy harvesting [203], sensing [204] and so on. However, using metamaterial absorber for isolation improvement in MIMO antennas has not been explored much [205–207].

In this paper, a patch antenna is designed to operate at 5.5 GHz WiMAX frequency which is arranged in a 2 element MIMO array and its characteristics are studied. Further, a flower-shaped metamaterial absorber is designed and analysed using periodic boundaries and floquet ports. The proposed MA exhibits 98.7 % absorptivity at 5.5 GHz. An array of 4 elements of the designed absorber is then placed in the middle of the MIMO antenna system and its characteristics are studied. The use of MA helped in achieving a simulated isolation level of more than 30 dB. The structure is further analysed to examined its applicability as a MIMO antenna in terms of ECC, DG and TARC. The design is finally fabricated and measured to achieve an isolation level of more than 40 dB. All the designing and simulation is done using Ansys High frequency structure simulator (HFSS) [188].

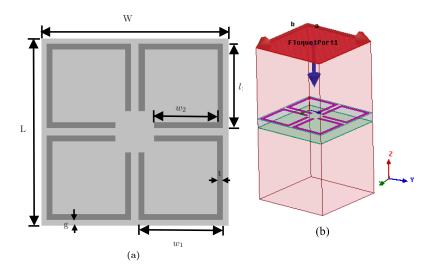


Figure 6.1: (a) Schematic of the proposed metamaterial absorber unit cell. (b) Simulation set up of the proposed MA unit cell

6.1 PROPOSED METAMATERIAL ABSORBER DESIGN AND SIMULATION

A metamaterial based absorber is designed on a 1 mm thick FR-4 substrate with dielectric constant(ε_r) of 4.4 and loss tangent(δ) of 0.02 with a unit cell size of 9×9 mm² which is much less than $\lambda/4$ where λ is the wavelength at the operating frequency, making the structure effectively homogeneous. The proposed MA unit cell consists of four square rings split at the corner, arranged in a form of a symmetrical flower shape, as shown in Fig. 6.1(a). The evolution of the proposed MA, shown in Fig. 6.2, starts with a conventional square ring operating around 9 GHz (Fig. 6.2(I)). Then a split was introduced at the corner of the ring, shown in Fig. 6.2(II), to increase the equivalent capacitance due to which the operating frequency shifted towards lower side, however, the absorptivity obtained was less than 50%. Further, to obtain four fold symmetry, a flower shaped design was constructed by rotating the split square ring 90° in the clockwise direction. It resulted in a significant improvement in the absorptivity due to increased electric and magnetic coupling between the cells. Finally, the design was scaled down and optimized to provide an absorptivity of 98.7% at 5.5 GHz (Fig. 6.2(III)).

The design parameters of MA as indicated in Fig. 6.1(a) are given as W=9mm, L=9mm, l_1 =4.05mm, w_1 =4.05mm, w_2 =3.2mm, g=0.2mm, t=0.3mm. The MA is simulated by applying

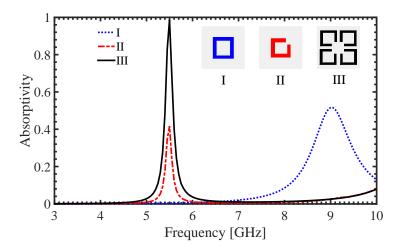


Figure 6.2: Absorptivities of different metamaterial absorber shapes.

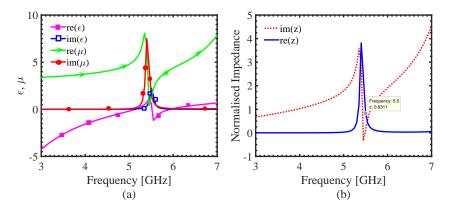


Figure 6.3: (a) Material parameters of metamaterial absorber (b) Normalized impedance of the metamaterial absorber

floquet port and periodic boundary conditions in Ansys HFSS, shown in Fig. 6.1(b). The absorptivity of the proposed MA is obtained using Eq. 6.1

$$A(\omega) = 1 - |S_{11}(\omega)|^2 - |S_{21}(\omega)|^2$$
(6.1)

Where, $|S_{11}(\omega)|^2$ and $|S_{21}(\omega)|^2$ represents the reflectivity and transitivity respectively with respect to frequency ω . Since, the bottom of the substrate is completely laminated by copper so all the power is reflected back from the bottom which indicated zero transmission, thus, $|S_{21}(\omega)|^2=0$. Therefore, Eq. 6.1 reduces to

$$A(\omega) = 1 - |S_{11}(\omega)|^2 \tag{6.2}$$

Thus, to obtain near unity absorption, Reflected power from the unit cell has to be minimized. The reflectivity from a medium for a normally incident electromagnetic wave is given by eq. 6.3 [208].

$$R = \left| \frac{\mu_r - n}{\mu_r + n} \right|^2 \tag{6.3}$$

where, μ_r and ε_r are relative permeability and permittivity of the medium and n is the refractive index of medium given by $\sqrt{\mu_r \varepsilon_r}$. When ε_r and μ_r are equal, reflectivity (R) is ideally zero. Fig. 6.3(a) depicts the real and imaginary part of permittivity and permeability. At 5.5 GHz, the value of permittivity is 0.6612+j2.269 and permeability is 1.24+j1.604 which are almost equal in magnitude, thus resulting in very low value of reflectivity.

Now, the normalized impedance (normalized to 377 ohms i.e. the free space impedance) of the absorber is given by Eq. 6.4

$$Z_{nor} = \sqrt{(\mu_r/\varepsilon_r)} \tag{6.4}$$

If both the ε_r and μ_r are equal, then the normalized impedance of the absorber Z_{nor} is ideally unity which implies perfect impedance matching of the structure with the free space, necessary to obtain perfect absorption. Fig. 6.3(b) shows the real and imaginary part of normalized impedance. The real part of normalised impedance is observed to be 0.8311 at the operating frequency 5.5 GHz which is close to the free space impedance and its imaginary part is close to zero, thus obtaining near perfect absorption.

The absorption phenomenon is further explained using the surface current density and volume current density plot of the MA at 5.5 GHz, as shown in Fig. 6.4(a) and (b) respectively. Fig. 6.4(a) shows that at the resonant frequency, current flowing on top and bottom surfaces are anti-parallel to each other forming current loops in the direction perpendicular to the applied

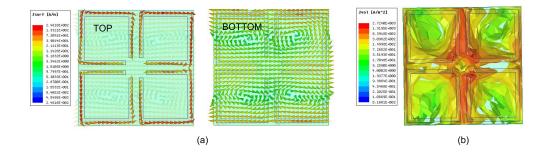


Figure 6.4: (a) Surface current density plot of MA at 5.5 GHz (Top view and Bottom view) (b) Volume current density plot of MA at 5.5 GHz.

magnetic field. This indicates magnetic excitation in the structure which manipulates magnetic permeability of the structure. Fig. 6.4(b) shows volume current distribution of the MA at the resonant frequency where near unity absorption takes place. This indicates the occurrence of dielectric losses within the FR-4 substrate. Therefore, the Fig. 6.4 clearly shows that electric and magnetic excitation leads to strong electromagnetic absorption at 5.5 GHz.

The proposed flower shaped absorber is engineered as an effective metamaterial medium (fulfilling the inclusion size requirement of an effectively homogeneous structure) to provide nearly equal value of relative permittivity and permeability (not found in any naturally occurring material) by properly optimizing the size and dimensions of the structure; therefore, it can be called as a true metamaterial.

After designing the metamaterial absorber operating at the intended frequency, the structure is investigated for isolation improvement of MIMO antenna in the next section.

6.2 MIMO ANTENNA DESIGN AND SIMULATION

First of all a conventional microstrip patch antenna with patch dimensions $12.2 \times 16.1 mm^2$ is designed on a 1 mm thick FR-4 substrate using a quarter wave transformer feed to operate at 5.5 GHz resonant frequency. The antenna is further arranged in a 1×2 array system. The centre to centre spacing between the two antennas is kept 30 mm which is nearly equivalent to $\lambda_0/2$, where λ_0 is the wavelength at operating frequency. To improve the isolation between

the two patch antennas, a linear array of four elements of the proposed MA is placed in the middle of the two patch antennas operating at 5.5 GHz, shown as an inset in the Fig. 6.5. Such a structure can be termed as a "metamaterial-inspired" kind, since its properties are determined by the interaction with only a 4-element array of the proposed absorber, rather than with an effective metamaterial medium.

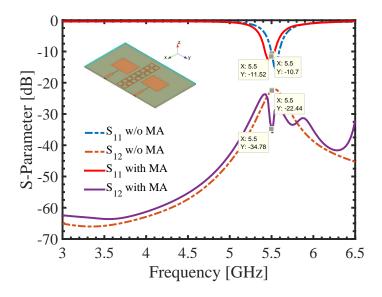


Figure 6.5: Simulated S-parameters with and without the proposed MA along with 3D view of the proposed MIMO antenna with flower shaped MA.

The proposed MIMO structure is simulated using Ansys HFSS and the results are analysed. Fig. 6.5 shows the simulated S-parameters of the MIMO antenna with and without the MA. Due to symmetry of the design, S_{11} is equivalent to S_{22} and S_{12} is equivalent to S_{21} , therefore, only S_{11} and S_{12} are displayed in the Fig. 6.5. Results show that at 5.5 GHz, the reflection coefficient (S_{11}) remains almost same for both the cases whereas the parameter S_{12} decreases from -22.46 dB to -34.87 dB showing a mutual coupling reduction by 12.41 dB as compared to the conventional MIMO antenna system. Thus a very high amount of isolation can be achieved with the help of proposed metamaterial absorber.

The operating mechanism for mutual coupling reduction using MA can be further understood using surface current distribution plot. Fig. 6.6(a) and (b) respectively shows the surface current distribution of the MIMO antenna without and with metamaterial absorber at 5.5 GHz

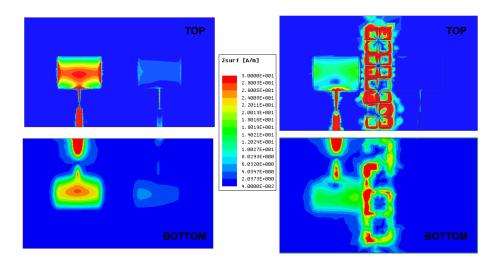


Figure 6.6: Surface current distribution at 5.5 GHz (a) without MA, (b) with MA.

obtained by exciting antenna 1 and terminating antenna 2 by matched load. It can be seen that without the use of MA, some amount of the surface current gets coupled from antenna 1 to antenna 2. Whereas, in case of MIMO antenna with MA, the propagating current on the top surface and bottom ground plane excites the absorber array in such a way that an anti-parallel current starts propagating between the top flower shape structure and the ground beneath it. This phenomenon results in trapping of the magnetic field within the MA array, thus not allowing the surface current to flow further, as shown in Fig. 6.6(b). Therefore, use of the MA stops the propagation of electromagnetic energy from antenna 1 to antenna 2, thus resulting in high level of isolation between them.

Furthermore, the simulated 2D radiation patterns of MIMO antenna are studied at 5.5 GHz to observe the effect of MA on the radiation performance of MIMO structure. Fig. 6.7(a),(b) and (c) shows the 2D far field radiation pattern of proposed structure on xz, yz and xy planes respectively. From the Fig. 6.7 it can be concluded that there is no significant effect on the radiation-pattern of the antenna after placing the MA, except that the magnitude of the main lobe is increased a little. This shows an improvement in the antenna parameters in terms of radiation efficiency and gain along with preserving the radiation characteristics as an effect of the reduced mutual coupling between the antennas. Fig. 6.8 shows the peak gain and radiation

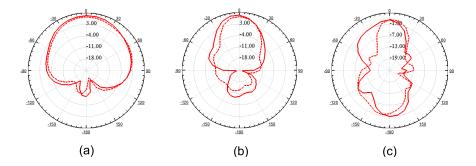


Figure 6.7: MIMO antenna far field radiation pattern at 5.5 GHz with (-solid line) and without (-dashed line) MA on (a) xz-plane (b) yz-plane (c) xy-plane.

efficiency plot of MIMO structure. The graph shows a peak gain of 7.53 dBi without MA and 7.74 dBi with MA at 5.5 GHz. Also, there is an increase in radiation efficiency from 66.64 % to 68.03%.

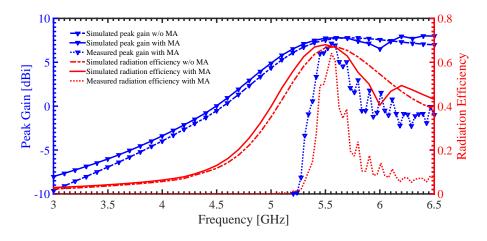


Figure 6.8: Peak gain and radiation efficiency plot of MIMO with and without MA

Now, the diversity performance is studied in the next section to validate the optimum performance of MIMO antenna.

6.3 MIMO DIVERSITY PERFORMANCE

The diversity performance of MIMO antenna is analysed on the basis of different parameters such as Envelope Correlation Coefficient (ECC), Diversity Gain (DG), and Total Active Reflection Co-efficient (TARC) [5]. For a practical MIMO antenna, it is required to have min-

$$ECC = \left| \frac{|S_{11}^* S_{12} + S_{12}^* S_{22}|}{|(1 - |S_{11}|^2 - |S_{21}|^2)(1 - |S_{12}|^2 - |S_{22}|^2)(\eta_{rad,1}\eta_{rad,2})|^{1/2}} \right|^2$$
(6.5)

Table 6.1: Performance comparison of the MIMO antenna with and without the proposed MA at 5.5

<u>GHz</u>						
MIMO	Simulated	Simulated	Measured	Measured	Peak	Radiation
antenna	S_{11} [dB]	S ₁₂ [dB]	S_{11} [dB]	S_{12} [dB]	Gain [dBi]	Efficiency
Without MA	-10.68	-22.46	-11.2	-22.1	7.53	66.64 %
With MA	-11.5	-34.77	-10.40	-43.71	7.74	68.03 %

imum signal correlation between the antenna elements which can be analysed using ECC. It can be obtained using the S-parameters and radiation efficiency, for a 2-port MIMO system, given by eq. 6.5 [209], where, $\eta_{rad,1}$ and $\eta_{rad,2}$ are the radiation efficiencies of antenna 1 and antenna 2. For a satisfactory performance MIMO antenna should have ECC less than 0.5.

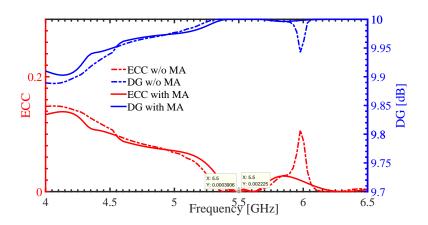


Figure 6.9: Simulated ECC and DG of MIMO antenna with MA.

Fig. 6.9 shows a simulated ECC of less than 0.05 for the operating band which shows low correlation between the two antennas. The diversity gain can be obtained using eq. 6.6 which is also shown in Fig. 6.9. The value of diversity gain is observed to be close to 10 dB, which indicates good diversity performance.

$$DG = 10 \times \sqrt{(1 - ECC^2)} \tag{6.6}$$

Total Active Reflection Co-efficient (TARC) is another parameters to define the diversity

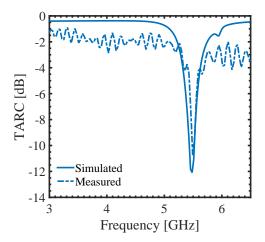


Figure 6.10: Simulated and measured TARC of MIMO antenna with MA.

performance of MIMO structure. It is the square root of the ratio of total reflected power to the total incident power and hence, it shows the apparent return loss of the overall MIMO antenna system. For a side-by-side 2-port MIMO system, it is given by eq. 6.7.

$$TARC = \sqrt{\frac{(S_{11} + S_{12})^2 + (S_{22} + S_{21})^2}{2}}$$
(6.7)

It is expected to have a TARC value of less than 0 dB for a MIMO system to work properly. Fig. 6.10 shows the plot of TARC with respect to frequency and it is observed to have a TARC value of less than -10 dB for the desired frequency which is well below the expected value.

6.4 EXPERIMENTAL RESULTS AND DISCUSSION

After studying all the simulated results, antenna is finally fabricated and tested using Keysight N9914A vector network analyzer. The fabricated prototype of the proposed structure along with the measured S-parameters compared to the simulated ones as a function of frequency are shown in Fig. 6.11 Result shows that a measured isolation level of -43.71 dB is achieved between the two conventional patch antennas at 5.5 GHz WiMAX frequency by using an array of proposed metamaterial absorber between them. The values of measured gain and radiation efficiency, shown in the Fig. 6.8, are observed to be 6.28 dBi and 56% respectively

Table 6.2: A comparison of proposed technique with previously presented ones

Reference	Technique	Isolation (dB)	Frequency [GHz]
[210]	Decoupling Structure	35	2.67
[211]	Patch separation	33	6.8
[212]	Modified Serpentine	34	2.45
[213]	Decoupling Structure	30	2.5
[205]	Metamaterial Absorber	34	5.29
[206]	Metamaterial Absorber	30	5.1
Proposed	Metamaterial Absorber	43.71	5.5

at the resonant frequency 5.5 GHz. Measured value of ECC calculated at 5.5 GHz is 0.00043. Measured TARC is also indicated in Fig. 6.10.

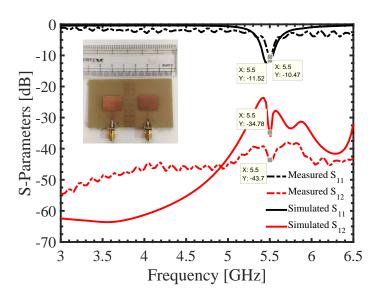


Figure 6.11: Measured and simulated S-parameters with fabricated prototype of proposed structure.

Table 6.1 gives a performance comparison of the MIMO antenna with and without the proposed MA at 5.5 GHz. Now, a comparison of proposed technique with previously presented ones is given in Table 6.2, taking into account the structures operating at single resonant frequency.

6.5 SUMMARY

The effect of utilizing a metamaterial based absorber for mutual coupling reduction in a MIMO antenna system is examined. A novel flower shaped metamaterial absorber is designed with

an absorptivity of 98.7 % and placed between the two conventional patch antennas to observe a simulated isolation level of 34.77 dB and measured isolation of 43.71 dB at the 5.5 GHz WiMAX frequency without effecting the return loss. An improvement in peak gain from 7.53 dBi to 7.74 dBi and radiation efficiency from 66.64 % to 68.03% is also observed. Other parameters like ECC, diversity gain and TARC are also studied and are found to be fairly below the expected limit of wireless communication application. Therefore, the proposed structure is quite suitable for MIMO application showing high level of isolation and good amount of radiation efficiency and peak gain.

CHAPTER 7

CONCLUSION

7.1 CONCLUSION

This thesis presents application of metamaterial in designing three different microwave components i.e. antennas, filters and absorbers. The design technique is presented and discussed for all the components. The proposed structures are low profile, simple in design which simplifies their integration with advanced small wireless systems. It was validated that each of the presented designs are suitable for multiple applications.

The application of metamterial in miniaturizing the overall size of a CPW-fed microstrip planar antenna has been investigated first in which the following points were concluded.

- 1. Dual band characteristics have been observed at 2.45 GHz and 5.45 GHz operating frequencies with a gain of 1.9 dBi to 2.41 dBi and 2.2 dBi to 2.5 dBi respectively.
- 2. The two bands are originated from the metamaterial used in the antenna consisting two triangular split rings and impedance matching is achieved using open circuited stub.
- 3. The antenna miniaturized by 2.5 times.
- 4. Nearly omnidirectional radiation patterns are observed at both frequencies.
- 5. The experimental results have a good agreement with the simulated results.
- 6. The proposed antenna supports 2.4/5.2/5.8 GHz WLAN bands which offers wide range of application in wireless communication systems.

Secondly, a complimentary split ring resonator based microstrip bandstop filter is investigated using equivalent circuit analysis.

- 1. A stop band at the vicinity of 2.4 GHz is obtained.
- 2. Based on the simulated results, the circuit arrangement is defined to be a series connected parallel resonant circuit followed by a series connected inductor.

- Simplified mathematical approach is described in detail to obtain the lumped circuit
 parameters. Only three lumped components are used to define the circuit model, thus
 reducing the circuit complexity.
- 4. Parametric variation of the split rings is also analysed which displays frequency tuning capability by varying the dimensions of split rings.
- 5. Finally, the filter is fabricated and measured to show fair agreement with the simulated results. The proposed bandstop filter shows good lower pass band performance.

The equivalent circuit approach used above is further validated by utilizing the approach to find equivalent circuits of various filters presented in literature and a comparison based study is also presented. Furthermore, another metamaterial inspired filter showing wideband bandpass filter response using two closed coupled U-shaped resonators is presented in which following points are observed.

- 1. The filter provided a 3 dB pass band from 2.44 GHz to 5.58 GHz which further increased from 1.43 GHz to 5.56 GHz when the vertical slot was placed.
- 2. The slot introduced between the two U-shaped slots to increase the bandwidth accounts for increase in electric coupling.
- 3. The propagation characteristics of the filter have been studied that demonstrated the dual balanced CRLH line behaviour of the filter.
- 4. Very small amount of group time delay (0.63 ns) is provided by the filter in the passband region.
- 5. A high return loss of 37.5 dB is achieved at the pass band resonant frequency.

Then, an ultra thin metamaterial based absorber with penta-band behaviour is presented. The penta-band obtained are as a result of the three simple geometries combined on a single $10 \times 10 mm^2$ FR-4 substrate. The dimensions of each geometry are optimised in order to obtain nearly perfect impedance matching. Following observations are drawn:

- 1. The structure provides an absorptivity greater than 90% for five bands lying in four different microwave bands i.e. S, C, X, Ku-band.
- The structure provides simulated absorption peaks at 3.35 GHz, 5.1 GHz, 9.5 GHz, 11.55 GHz and 16.9 GHz with absorptivity 99.59%, 95.49%, 97.5%, 99.25% and 93.89% respectively.
- 3. The four-fold symmetry of the structure enable polarization insensitivity and high absorption over different angle of incidence of electromagnetic wave for TE and TM polarization.
- 4. The measured results shows absorption peaks at 3.75 GHz, 4.98 GHz, 9.5 GHz, 12.2 GHz and 16.8 GHz with absorptivity of 94.75%, 92.76%, 95.43%, 99.86 %, and 96.86 % respectively.
- 5. Radar cross section reduction can be done through the proposed metamaterial absorber. Also, it can be used in other FCC-defined airborne applications.

Another simplified geometry i.e. a closed meander line shaped metamaterial absorber is also proposed in the 3.5 GHz WiMAX band which is also analysed using its equivalent circuit.

Finally, the effect of utilizing a metamaterial based absorber for mutual coupling reduction in a MIMO antenna system is examined. A novel flower shaped metamaterial absorber is designed with an absorptivity of 98.7 % and placed between the two conventional patch antennas to observe the following:

- A simulated isolation level of 34.77 dB and measured isolation of 43.71 dB at the 5.5
 GHz WiMAX frequency without effecting the return loss.
- 2. An improvement in peak gain from 7.53 dBi to 7.74 dBi and radiation efficiency from 66.64 % to 68.03% is also observed.

- 3. Other parameters like ECC, diversity gain and TARC are also studied and are found to be fairly below the expected limit of wireless communication application.
- 4. The proposed structure is quite suitable for MIMO application showing high level of isolation and good amount of radiation efficiency and peak gain.

Therefore, different applications of metamaterials have been studied and tested during the thesis and it is concluded that metamaterials have the potential to revolutionarize several applications of microwave engineering.

CHAPTER 8

FUTURE SCOPE

8.1 FUTURE SCOPE

Based on observations identified during the entire duration of this thesis, there are research areas that would be very interesting for further investigation.

8.1.1 Metamaterial Antennas

- 1. In future higher gain and directivity of antennas can be achieved by utilizing metasurfaces and also by developing multi-element MIMO systems.
- 2. The present work can also be extended to work in 5G frequency range by scaling the dimensions of proposed structure.
- 3. Reconfigurability in pattern, bandwidth and frequency may also be achieved.

8.1.2 Metamaterial Filters

- 1. Filters can be made reconfigurable by introducing active components.
- 2. Other filter configurations as discussed in the literature review can also be investigated.
- 3. UWB and super wideband filters may also be explored.

8.1.3 Metamaterial Absorbers

- 1. Broadband metamaterial absorbers can be investigated.
- 2. Use of metamaterial absorbers in mutual coupling reduction between antennas can be explored further with improvement in gain and bandwidth.
- 3. Active components can be integrated to make the devices reconfigurable.

The structures can possibly be investigated in real world systems. The components may be designed for high frequencies i.e. THz range and broadband devices can also be developed.

REFERENCES

- [1] V. G. Veselago, "The electrodynamics of substances with simultaneously negative values of ε and μ ," *Physics-Uspekhi*, vol. 10, no. 4, pp. 509–514, 1968.
- [2] J. B. Pendry, A. J. Holden, D. J. Robbins, and W. J. Stewart, "Magnetism from conductors and enhanced nonlinear phenomena," *IEEE Transactions on Microwave Theory and Techniques*, vol. 47, no. 11, pp. 2075–2084, 1999.
- [3] J. B. Pendry, A. J. Holden, W. J. Stewart, and I. Youngs, "Extremely low frequency plasmons in metallic mesostructures," *Phys. Rev. Lett.*, vol. 76, pp. 4773–4776, 1996.
- [4] W. Cao, Y. Xiang, B. Zhang, A. Liu, T. Yu, and D. Guo, "A low-cost compact patch antenna with beam steering based on CSRR-loaded ground," *IEEE Antennas and Wireless Propagation Letters*, vol. 10, pp. 1520–1523, 2011.
- [5] M. Gupta and J. Saxena, "Microstrip filter designing by SRR metamaterial," *Wireless Personal Communications*, vol. 71, no. 4, pp. 3011–3022, 2013.
- [6] S. Haxha, F. AbdelMalek, F. Ouerghi, M. Charlton, A. Aggoun, and X. Fang, "Metamaterial superlenses operating at visible wavelength for imaging applications," *Scientific reports*, vol. 8, 2018.
- [7] N. I. Landy, S. Sajuyigbe, J. J. Mock, D. R. Smith, and W. J. Padilla, "Perfect metamaterial absorber," *Physical review letters*, vol. 100, no. 20, p. 207402, 2008.
- [8] P. Alitalo and S. Tretyakov, "Electromagnetic cloaking with metamaterials," *Materials Today*, vol. 12, no. 3, pp. 22 29, 2009.
- [9] C. Sabah, F. Dincer, M. Karaaslan, E. Unal, O. Akgol, and E. Demirel, "Perfect metamaterial absorber with polarization and incident angle independencies based on ring

- and cross-wire resonators for shielding and a sensor application," *Optics Communications*, vol. 322, pp. 137–142, 2014.
- [10] T. Mynttinen, M. Lapine, J. Saily, I. S. Nefedov, and S. A. Tretyakov, "Microwave devices with enhanced phase-compensation principle," in *European Conference on Antennas and Propagation*, pp. 1–5, IEEE, 2006.
- [11] F. Falcone, T. Lopetegi, J. D. Baena, R. Marques, F. Martin, and M. Sorolla, "Effective negative stopband microstrip lines based on complementary split ring resonators," *IEEE Microwave and Wireless Components Letters*, vol. 14, no. 6, pp. 280–282, 2004.
- [12] Z. Qamar, U. Naeem, S. A. Khan, M. Chongcheawchamnan, and M. F. Shafique, "Mutual coupling reduction for high-performance densely packed patch antenna arrays on finite substrate," *IEEE Transactions on Antennas and Propagation*, vol. 64, no. 5, pp. 1653–1660, 2016.
- [13] X. Cheng, D. E. Senior, C. Kim, and Y. Yoon, "A compact omnidirectional self-packaged patch antenna with complementary split-ring resonator loading for wireless endoscope applications," *IEEE Antennas and Wireless Propagation Letters*, vol. 10, pp. 1532–1535, 2011.
- [14] R. O. Ouedraogo, E. J. Rothwell, A. R. Diaz, K. Fuchi, and A. Temme, "Miniaturization of patch antennas using a metamaterial-inspired technique," *IEEE Transactions on Antennas and Propagation*, vol. 60, no. 5, pp. 2175–2182, 2012.
- [15] J. Ha, K. Kwon, Y. Lee, and J. Choi, "Hybrid mode wideband patch antenna loaded with a planar metamaterial unit cell," *IEEE Transactions on Antennas and Propagation*, vol. 60, no. 2, pp. 1143–1147, 2012.
- [16] E. Rajo-Iglesias, . Quevedo-Teruel, and L. Inclan-Sanchez, "Mutual coupling reduction in patch antenna arrays by using a planar EBG structure and a multilayer dielectric

- substrate," *IEEE Transactions on Antennas and Propagation*, vol. 56, no. 6, pp. 1648–1655, 2008.
- [17] F. Farzami, K. Forooraghi, and M. Norooziarab, "Miniaturization of a microstrip antenna using a compact and thin magneto-dielectric substrate," *IEEE Antennas and Wireless Propagation Letters*, vol. 10, pp. 1540–1542, 2011.
- [18] Z. Liu, P. Wang, and Z. Zeng, "Enhancement of the gain for microstrip antennas using negative permeability metamaterial on low temperature co-fired ceramic (LTCC) substrate," *IEEE Antennas and Wireless Propagation Letters*, vol. 12, pp. 429–432, 2013.
- [19] M.-C. Tang, S. Xiao, T. Deng, Y. Wang, Y. Bai, C. Liu, Y. Shang, J. Xiong, and B. Wang, "Design of a broadband μ-negative planar material with low frequency dispersion," *Applied Physics A*, vol. 106, no. 4, pp. 821–828, 2012.
- [20] M. Koutsoupidou, I. S. Karanasiou, and N. Uzunoglu, "Substrate constructed by an array of split ring resonators for a THz planar antenna," *Journal of Computational Electronics*, vol. 13, no. 3, pp. 593–598, 2014.
- [21] R. Khajeh Mohammad Lou, M. Naser-Moghadasi, and R. A. Sadeghzadeh, "Compact multi-band circularly polarized CPW fed antenna based on metamaterial resonator," *Wireless Personal Communications*, vol. 94, no. 4, pp. 2853–2863, 2017.
- [22] P. Y. Chen and A. Alu, "Sub-wavelength elliptical patch antenna loaded with μ-negative metamaterials," *IEEE Transactions on Antennas and Propagation*, vol. 58, no. 9, pp. 2909–2919, 2010.
- [23] M. Tang, S. Xiao, Y. Bai, T. Deng, C. Liu, Y. Shang, C. Wei, and B. Wang, "Design of hybrid patch/slot antenna operating in induced TM120 Mode," *IEEE Transactions on Antennas and Propagation*, vol. 60, no. 5, pp. 2157–2165, 2012.

- [24] H. Xu, G. Wang, and M. Qi, "Hilbert-shaped magnetic waveguided metamaterials for electromagnetic coupling reduction of microstrip antenna array," *IEEE Transactions on Magnetics*, vol. 49, no. 4, pp. 1526–1529, 2013.
- [25] B. D. Bala, M. K. A. Rahim, and N. A. Murad, "Complementary electric-LC resonator antenna for WLAN applications," *Applied Physics A*, vol. 117, no. 2, pp. 635–639, 2014.
- [26] M. Wiltshire, J. Hajnal, J. Pendry, and D. Edwards, "Experimental verification of a negative index of refraction," *Science*, vol. 292, no. 5514, pp. 60–61, 2001.
- [27] A. S. M. Alqadami, M. F. Jamlos, P. J. Soh, S. K. A. Rahim, and A. Narbudowicz, "Left-handed compact MIMO antenna array based on wire spiral resonator for 5-GHz wireless applications," *Applied Physics A*, vol. 123, no. 1, p. 64, 2016.
- [28] J. Wang, S. Qu, H. Ma, S. Xia, Y. Yang, L. Lu, X. Wu, Z. Xu, and Q. Wang, "Experimental verification of anisotropic three-dimensional left-handed metamaterial composed of jerusalem crosses," *PIERS online*, vol. 6, no. 1, 2010.
- [29] A. R. Katko, *Artificial negative permeability based on a fractal Jerusalem Cross*. PhD thesis, The Ohio State University, 2009.
- [30] K. Inamdar, Y. P. Kosta, and S. Patnaik, "Criss-cross metamaterial-substrate microstrip antenna with enhanced gain and bandwidth," *Radioelectronics and Communications Systems*, vol. 58, no. 2, pp. 69–74, 2015.
- [31] Mahmoud, "A new miniaturized annular ring patch resonator partially loaded by a metamaterial ring with negative permeability and permittivity," *IEEE Antennas and Wireless Propagation Letters*, vol. 3, pp. 19–22, 2004.
- [32] M. Wu, F. Meng, Q. Wu, J. Wu, and J. Lee, "An approach for small omnidirectional

- microstrip antennas based on the backward waves of double negative metamaterials," *Applied Physics A*, vol. 87, no. 2, pp. 193–198, 2007.
- [33] M. M. Islam, M. R. I. Faruque, M. T. Islam, and M. F. Mansor, "Compact and broadband antenna using double-negative transmission line metamaterial," *Applied Physics A*, vol. 123, no. 1, p. 21, 2016.
- [34] P. Kaur, S. K. Aggarwal, and A. De, "Performance enhancement of rectangular microstrip patch antenna using double H- shaped metamaterial," *Radioelectronics and Communications Systems*, vol. 59, no. 11, pp. 496–501, 2016.
- [35] Y. D. Sirmaci, C. K. Akin, and C. Sabah, "Fishnet based metamaterial loaded THz patch antenna," *Optical and Quantum Electronics*, vol. 48, no. 2, p. 168, 2016.
- [36] A. Lucibello, E. Proietti, R. Marcelli, G. M. Sardi, and G. Bartolucci, "Narrow-band filtering by means of triangular meta-material resonators based on RF MEMS cantilevers in CPW configuration," *Microsystem Technologies*, vol. 23, no. 9, pp. 3955–3967, 2017.
- [37] H. A. Majid and M. K. A. Rahim, "Parametric studies on left-handed metamaterial consist of modified split-ring resonator and capacitance loaded strip," *Applied Physics A*, vol. 103, no. 3, pp. 607–610, 2011.
- [38] H.-X. Xu, G.-M. Wang, and M.-Q. Qi, "A leaky-wave antenna using double-layered metamaterial transmission line," *Applied Physics A*, vol. 111, no. 2, pp. 549–555, 2013.
- [39] J. Liang and H. Xu, "Harmonic suppressed bandpass filter using composite right/left handed transmission line," *Journal of Zhejiang University SCIENCE C*, vol. 13, no. 7, pp. 552–558, 2012.
- [40] C. Caloz and T. Itoh, *Electromagnetic Metamaterials, Transmission Line Theory and Microwave Applications*. New York: Wiley, 2005.

- [41] J. Carver, V. Reignault, and F. Gadot, "Engineering of the metamaterial-based cut-band filter," *Applied Physics A*, vol. 117, no. 2, pp. 513–516, 2014.
- [42] S. Awasthi, A. Biswas, and M. J. Akhtar, "Dual-band dielectric resonator bandstop filters," *International Journal of RF and Microwave Computer-Aided Engineering*, vol. 25, no. 4, pp. 282–288, 2014.
- [43] C. Kim, X. Cheng, D. E. Senior, and Y.-K. Yoon, "Compact frequency and bandwidth tunable stopband filters using split ring resonators and varactors coupled transmission line," *AEU International Journal of Electronics and Communications*, vol. 66, no. 11, pp. 865–870, 2012.
- [44] A. K. Gorur, A. O. Ceyhun Karpuz, and M. Emur, "Metamaterial based dualband band-pass filter design for WLAN/WiMAX applications," *Microwave and Optical Technology Letters*, vol. 56, no. 10, pp. 2211–2214, 2014.
- [45] J.-G. Park, K.-C. Yoon, H.-W. Lee, and J.-C. Lee, "A new high-Q compact resonator using combination of interdigital hair-pin resonator and meander-line with μ-near-zero metamaterial," *Microwave and Optical Technology Letters*, vol. 56, no. 8, pp. 1781–1785, 2014.
- [46] J. Fan, C. Liang, and B. Wu, "Dual-band filter using equal-length split-ring resonators and zero-degree feed structure," *Microwave and Optical Technology Letters*, vol. 50, no. 4, pp. 1098–1101, 2008.
- [47] K.-C. Yoon, J. H. Kim, and J.-C. Lee, "Band-pass filter with broad-side coupled triple split-ring resonator using left-handed metamaterial," *Microwave and Optical Technology Letters*, vol. 53, no. 9, pp. 2174–2177, 2011.
- [48] K. Afrooz, A. Abdipour, and F. Martín, "Broadband bandpass filter using open complementary split ring resonator based on metamaterial unit-cell concept," *Microwave and Optical Technology Letters*, vol. 54, no. 12, pp. 2832–2835, 2012.

- [49] T.-H. Lee, J.-W. Baik, and Y. Kim, "Compact cascaded quadruplet bandpass filter using artificial magnetic resonators," *Microwave and Optical Technology Letters*, vol. 55, no. 4, pp. 883–886, 2013.
- [50] K. U. Ahmed and B. S. Virdee, "Fine control of filter performance based on composite right/left-handed metamaterial technology," *International Journal of RF and Microwave Computer-Aided Engineering*, vol. 24, no. 1, pp. 39–45, 2014.
- [51] M. Palandöken and M. H. Ucar, "Compact metamaterial-inspired band-pass filter," *Microwave and Optical Technology Letters*, vol. 56, no. 12, pp. 2903–2907, 2014.
- [52] B. Jokanovic, V. Crnojevic-Bengin, and O. Boric-Lubecke, "Miniature high selectivity filters using grounded spiral resonators," *Electronics Letters*, vol. 44, no. 17, pp. 1019– 1020, 2008.
- [53] H. Nasraoui, A. Capobianco, A. Mouhsen, J. El Aoufi, Y. Mouzouna, and M. Taouzari, "Compact wideband band pass microstrip filter loaded by triangular split ring resonators," *Microwave and Optical Technology Letters*, vol. 59, no. 12, pp. 3101–3107, 2017.
- [54] J.-G. Park, K.-C. Yoon, and J.-C. Lee, "A new elliptic function band-pass filter with adjustable size using μ -near zero metamaterial resonators," *Microwave and Optical Technology Letters*, vol. 56, no. 10, pp. 2245–2248, 2014.
- [55] D. K. Choudhary and R. K. Chaudhary, "A compact via-less metamaterial wideband bandpass filter using split circular rings and rectangular stub," *Progress In Electromagnetics Research*, vol. 72, pp. 99–106, 2018.
- [56] F. Falcone, T. Lopetegi, M. A. G. Laso, J. D. Baena, J. Bonache, and M. Beruete, "Babinet principle applied to the design of metasurfaces and metamaterials," *Physical Review Letters*, vol. 93, no. 19, 2004.

- [57] A. Ali and Z. Hu, "Negative permittivity meta-material microstrip binomial low-pass filter with sharper cut-off and reduced size," *IET Microwaves, Antennas and Propagation*, vol. 2, no. 1, pp. 15–18, 2008.
- [58] H.-X. Xu, G.-M. Wang, C.-X. Zhang, and J.-G. Liang, "Hilbert-shaped complementary ring resonator and application to enhanced-performance low pass filter with high selectivity," *International Journal of RF and Microwave Computer-Aided Engineering*, vol. 21, no. 4, pp. 399–406, 2011.
- [59] X. Hu, Q. Zhang, and S. He, "Dual-band-rejection filter based on split ring resonator (SRR) and complimentary SRR," *Microwave and Optical Technology Letters*, vol. 51, no. 10, pp. 2519–2522, 2009.
- [60] J. Selga, G. Siso, M. Gil, J. Bonache, and F. Martín, "Microwave circuit miniaturization with complementary spiral resonators: Application to high-pass filters and dual-band components," *Microwave and Optical Technology Letters*, vol. 51, no. 11, pp. 2741– 2745, 2009.
- [61] L. Zhou, S.-b. Liu, X.-k. Kong, H.-f. Zhang, and Y.-n. Guo, "Ultra-wideband bandpass filters with a controllable and highly selective notch-band," *Microwave and Optical Technology Letters*, vol. 53, no. 12, pp. 2920–2922, 2011.
- [62] R. Ghatak, M. Pal, C. Goswami, and D. Poddar, "Moore curve fractal-shaped miniaturized complementary spiral resonator," *Microwave and Optical Technology Letters*, vol. 55, no. 8, pp. 1950–1954, 2013.
- [63] C.-H. Ahn, D.-J. Jung, and K. Chang, "Compact parallel-coupled line bandpass filter using double complementary split ring resonators," *Microwave and Optical Technology Letters*, vol. 55, no. 3, pp. 506–509, 2013.
- [64] H. Oraizi and S. Y. Torabi, "Novel application of a new metamaterial complementary electric LC resonator for the design of miniaturized sharp band-pass filters," *Inter-*

- national Journal of RF and Microwave Computer-Aided Engineering, vol. 23, no. 4, pp. 471–475, 2013.
- [65] L. Su, J. Naqui, J. Mata-Contreras, and F. Martín, "Modeling and applications of metamaterial transmission lines loaded with pairs of coupled complementary split-ring resonators (CSRRs)," *IEEE Antennas and Wireless Propagation Letters*, vol. 15, pp. 154– 157, 2015.
- [66] H.-R. Zhu, Y.-F. Sun, and X.-L. Wu, "A compact tapered EBG structure with sharp selectivity and wide stopband by using CSRR," *IEEE Microwave and Wireless Components Letters*, vol. 28, no. 9, pp. 771–773, 2018.
- [67] F. Martín, J. Bonache, F. Falcone, M. Sorolla, and R. Marqués, "Split ring resonator-based left-handed coplanar waveguide," *Applied Physics Letters*, vol. 83, no. 22, pp. 4652–4654, 2003.
- [68] A. Vélez, F. Aznar, M. Durán-Sindreu, J. Bonache, and F. Martín, "Stop-band and band-pass filters in coplanar waveguide technology implemented by means of electrically small metamaterial-inspired open resonators," *IET Microwaves, Antennas & Propagation*, vol. 4, no. 6, pp. 712–716, 2010.
- [69] M. Durán-Sindreu, F. Aznar, A. Vélez, J. Bonache, and F. Martín, "Analysis and applications of OSRR-and OCSRR-loaded transmission lines: A new path for the design of compact transmission line metamaterials," *Metamaterials*, vol. 4, no. 2-3, pp. 139–148, 2010.
- [70] M. Durán-Sindreu, P. Vélez, J. Bonache, and F. Martín, "High-order coplanar waveguide (CPW) filters implemented by means of open split ring resonators (OSRRs) and open complementary split ring resonators (OCSRRs)," *Metamaterials*, vol. 5, no. 2-3, pp. 51–55, 2011.

- [71] A. Borja, J. Carbonell, V. Boria, J. Cascon, and D. Lippens, "Synthesis of compact and highly selective filters via metamaterial-inspired coplanar waveguide line technologies," *IET microwaves, antennas & propagation*, vol. 4, no. 8, pp. 1098–1104, 2010.
- [72] A. Borja, J. Carbonell, V. Boria, J. Cascon, and D. Lippens, "Synthesis of compact and highly selective filters via metamaterial-inspired coplanar waveguide line technologies," *IET microwaves, antennas & propagation*, vol. 4, no. 8, pp. 1098–1104, 2010.
- [73] O. A. Safia, L. Talbi, and K. Hettak, "A new type of transmission line-based metamaterial resonator and its implementation in original applications," *IEEE Transactions on Magnetics*, vol. 49, no. 3, pp. 968–973, 2013.
- [74] M. A. Fouad and M. A. Abdalla, "New π-T generalised metamaterial negative refractive index transmission line for a compact coplanar waveguide triple band pass filter applications," *IET Microwaves, Antennas & Propagation*, vol. 8, no. 13, pp. 1097–1104, 2014.
- [75] D. K. Choudhary and R. K. Chaudhary, "A compact CPW-based dual-band filter using modified complementary split ring resonator," *AEU-International Journal of Electron*ics and Communications, vol. 89, pp. 110–115, 2018.
- [76] H. Li, L. H. Yuan, B. Zhou, X. P. Shen, Q. Cheng, and T. J. Cui, "Ultrathin multi-band gigahertz metamaterial absorbers," *Journal of Applied Physics*, vol. 110, no. 1, p. 014909, 2011.
- [77] S. Bhattacharyya, S. Ghosh, and K. V. Srivastava, "Bandwidth-enhanced metamaterial absorber using electric field–driven LC resonator for airborne radar applications," *Microwave and Optical Technology Letters*, vol. 55, no. 9, pp. 2131–2137, 2013.
- [78] S. Bhattacharyya and K. Vaibhav Srivastava, "Triple band polarization-independent ultra-thin metamaterial absorber using electric field-driven LC resonator," *Journal of Applied Physics*, vol. 115, no. 6, p. 064508, 2014.

- [79] S. Ghosh and K. V. Srivastava, "An equivalent circuit model of FSS-based metamaterial absorber using coupled line theory," *IEEE Antennas and Wireless Propagation Letters*, vol. 14, pp. 511–514, 2014.
- [80] Y.-J. Huang, G.-J. Wen, J. Li, W.-R. Zhu, P. Wang, and Y.-H. Sun, "Wide-angle and polarization-independent metamaterial absorber based on snowflake-shaped configuration," *Journal of Electromagnetic Waves and Applications*, vol. 27, no. 5, pp. 552–559, 2013.
- [81] S. R. Thummaluru, N. Mishra, and R. K. Chaudhary, "Design and analysis of an ultrathin X-band polarization-insensitive metamaterial absorber," *Microwave and Optical Technology Letters*, vol. 58, no. 10, pp. 2481–2485, 2016.
- [82] T. Liu, X. Cao, J. Gao, Q. Zheng, W. Li, and H. Yang, "RCS reduction of waveguide slot antenna with metamaterial absorber," *IEEE Transactions on Antennas and Propagation*, vol. 61, no. 3, pp. 1479–1484, 2012.
- [83] A. Sharma, D. Gangwar, B. K. Kanaujia, and S. Dwari, "Analysis and design of an ultrathin metamaterial absorber and its application for in-band RCS reduction of antenna," *Journal of Electromagnetic Waves and Applications*, vol. 33, no. 5, pp. 654–667, 2019.
- [84] D. Zheng, Y. Cheng, D. Cheng, Y. Nie, and R. Z. Gong, "Four-band polarization-insensitive metamaterial absorber based on flower-shaped structures," *Progress In Electromagnetics Research*, vol. 142, pp. 221–229, 2013.
- [85] M.-h. Li, S.-y. Liu, L.-y. Guo, H. Lin, H.-l. Yang, and B.-x. Xiao, "Influence of the dielectric-spacer thickness on the dual-band metamaterial absorber," *Optics Communications*, vol. 295, pp. 262–267, 2013.
- [86] S. Bhattacharyya, S. Ghosh, and K. Vaibhav Srivastava, "Triple band polarization-independent metamaterial absorber with bandwidth enhancement at X-band," *Journal of Applied Physics*, vol. 114, no. 9, p. 094514, 2013.

- [87] S. Bhattacharyya and K. Vaibhav Srivastava, "Triple band polarization-independent ultra-thin metamaterial absorber using electric field-driven LC resonator," *Journal of Applied Physics*, vol. 115, no. 6, p. 064508, 2014.
- [88] D. Sood and C. C. Tripathi, "Quad band electric field-driven LC resonator-based polarisation-insensitive metamaterial absorber," *IET Microwaves, Antennas & Propagation*, vol. 12, no. 4, pp. 588–594, 2017.
- [89] D. Singh and V. M. Srivastava, "Dual resonance shorted stub circular rings metamaterial absorber," *AEU-International Journal of Electronics and Communications*, vol. 83, pp. 58–66, 2018.
- [90] S. Bhattacharyya, S. Ghosh, and K. V. Srivastava, "Equivalent circuit model of an ultrathin polarization-independent triple band metamaterial absorber," *AIP Advances*, vol. 4, no. 9, p. 097127, 2014.
- [91] K. P. Kaur and T. Upadhyaya, "Wide-angle and polarisation-independent tri-band dual-layer microwave metamaterial absorber," *IET Microwaves, Antennas and Propagation*, vol. 12, no. 8, pp. 1428–1434, 2018.
- [92] H. Zhai, C. Zhan, L. Liu, and C. Liang, "A new tunable dual-band metamaterial absorber with wide-angle TE and TM polarization stability," *Journal of Electromagnetic Waves and Applications*, vol. 29, no. 6, pp. 774–785, 2015.
- [93] B. Bian, S. Liu, S. Wang, X. Kong, H. Zhang, B. Ma, and H. Yang, "Novel triple-band polarization-insensitive wide-angle ultra-thin microwave metamaterial absorber," *Journal of Applied Physics*, vol. 114, no. 19, p. 194511, 2013.
- [94] X. Huang, H. Yang, S. Yu, J. Wang, M. Li, and Q. Ye, "Triple-band polarization-insensitive wide-angle ultra-thin planar spiral metamaterial absorber," *Journal of Applied Physics*, vol. 113, no. 21, p. 213516, 2013.

- [95] S. Shang, S. Yang, L. Tao, L. Yang, and H. Cao, "Ultrathin triple-band polarization-insensitive wide-angle compact metamaterial absorber," *AIP Advances*, vol. 6, no. 7, p. 075203, 2016.
- [96] Z. Mao, S. Liu, B. Bian, B. Wang, B. Ma, L. Chen, and J. Xu, "Multi-band polarization-insensitive metamaterial absorber based on chinese ancient coin-shaped structures," *Journal of Applied Physics*, vol. 115, no. 20, p. 204505, 2014.
- [97] A. Bhattacharya, S. Bhattacharyya, S. Ghosh, D. Chaurasiya, and K. Vaibhav Srivastava, "An ultrathin penta-band polarization-insensitive compact metamaterial absorber for airborne radar applications," *Microwave and Optical Technology Letters*, vol. 57, no. 11, pp. 2519–2524, 2015.
- [98] M. Agarwal and M. K. Meshram, "Metamaterial-based dual-band microwave absorber with polarization insensitive and wide-angle performance," *AIP Advances*, vol. 8, no. 9, p. 095016, 2018.
- [99] H. Zhai, C. Zhan, Z. Li, and C. Liang, "A triple-band ultrathin metamaterial absorber with wide-angle and polarization stability," *IEEE Antennas and Wireless Propagation Letters*, vol. 14, pp. 241–244, 2014.
- [100] S. R. Thummaluru, N. Mishra, and R. K. Chaudhary, "Design and analysis of an ultrathin triple-band polarization independent metamaterial absorber," *AEU-International Journal of Electronics and Communications*, vol. 82, pp. 508–515, 2017.
- [101] S. K. Sharma, S. Ghosh, K. V. Srivastava, and A. Shukla, "Ultra-thin dual-band polarization-insensitive conformal metamaterial absorber," *Microwave and Optical Technology Letters*, vol. 59, no. 2, pp. 348–353, 2017.
- [102] N. Mishra, K. Kumari, and R. K. Chaudhary, "A dual resonator-based polarisation-independent dual-band metamaterial absorber," *International Journal of Electronics Letters*, vol. 7, no. 3, pp. 338–351, 2019.

- [103] A. Sarkhel and S. R. B. Chaudhuri, "Compact quad-band polarization-insensitive ultrathin metamaterial absorber with wide angle stability," *IEEE Antennas and Wireless Propagation Letters*, vol. 16, pp. 3240–3244, 2017.
- [104] H. Xiong, J.-S. Hong, C.-M. Luo, and L.-L. Zhong, "An ultrathin and broadband metamaterial absorber using multi-layer structures," *Journal of Applied Physics*, vol. 114, no. 6, p. 064109, 2013.
- [105] S. Ghosh, S. Bhattacharyya, D. Chaurasiya, and K. V. Srivastava, "Polarisation-insensitive and wide-angle multi-layer metamaterial absorber with variable bandwidths," *Electronics Letters*, vol. 51, no. 14, pp. 1050–1052, 2015.
- [106] L. Li and Z. Lv, "Ultra-wideband polarization-insensitive and wide-angle thin absorber based on resistive metasurfaces with three resonant modes," *Journal of Applied Physics*, vol. 122, no. 5, p. 055104, 2017.
- [107] H. Luo, Y. Cheng, and R. Gong, "Numerical study of metamaterial absorber and extending absorbance bandwidth based on multi-square patches," *The European Physical Journal B*, vol. 81, no. 4, pp. 387–392, 2011.
- [108] L. Li, J. Wang, H. Du, J. Wang, S. Qu, and Z. Xu, "A band enhanced metamaterial absorber based on E-shaped all-dielectric resonators," *AIP Advances*, vol. 5, no. 1, p. 017147, 2015.
- [109] S. Li, J. Gao, X. Cao, W. Li, Z. Zhang, and D. Zhang, "Wideband, thin, and polarization-insensitive perfect absorber based the double octagonal rings metamaterials and lumped resistances," *Journal of Applied Physics*, vol. 116, no. 4, p. 043710, 2014.
- [110] P. Munaga, S. Ghosh, S. Bhattacharyya, and K. V. Srivastava, "A fractal-based compact broadband polarization insensitive metamaterial absorber using lumped resistors," *Microwave and Optical Technology Letters*, vol. 58, no. 2, pp. 343–347, 2016.

- [111] T. T. Nguyen and S. Lim, "Angle-and polarization-insensitive broadband metamaterial absorber using resistive fan-shaped resonators," *Applied Physics Letters*, vol. 112, no. 2, p. 021605, 2018.
- [112] W. Zuo, Y. Yang, X. He, C. Mao, and T. Liu, "An ultrawideband miniaturized metamaterial absorber in the ultrahigh-frequency range," *IEEE Antennas and Wireless Propagation Letters*, vol. 16, pp. 928–931, 2016.
- [113] M. D. Banadaki, A. A. Heidari, and M. Nakhkash, "A metamaterial absorber with a new compact unit cell," *IEEE Antennas and Wireless Propagation Letters*, vol. 17, no. 2, pp. 205–208, 2017.
- [114] S. Ghosh, S. Bhattacharyya, Y. Kaiprath, and K. Vaibhav Srivastava, "Bandwidth-enhanced polarization-insensitive microwave metamaterial absorber and its equivalent circuit model," *Journal of Applied Physics*, vol. 115, no. 10, p. 104503, 2014.
- [115] S. Fan and Y. Song, "Bandwidth-enhanced polarization-insensitive metamaterial absorber based on fractal structures," *Journal of Applied Physics*, vol. 123, no. 8, p. 085110, 2018.
- [116] W. Wang, Y. Chen, S. Yang, X. Zheng, and Q. Cao, "Design of a broadband electro-magnetic wave absorber using a metamaterial technology," *Journal of Electromagnetic Waves and Applications*, vol. 29, no. 15, pp. 2080–2091, 2015.
- [117] L. Peng, C.-L. Ruan, and X.-H. Wu, "Design and operation of dual/triple-band asymmetric M-shaped microstrip patch antennas," *IEEE Antennas and Wireless Propagation Letters*, vol. 9, pp. 1069–1072, 2010.
- [118] T.-H. Chang and J.-F. Kiang, "Compact multi-band H-shaped slot antenna," *IEEE Transaction on Antennas and Propagation*, vol. 12, pp. 305–309, 2013.

- [119] A. K. Gautam and B. K. Kanaujia, "A novel dual-band asymmetric slit with defected ground structure microstrip antenna for circular polarization operation," *Microwave and Optical Technology Letters*, vol. 55, pp. 1198–1201, 2013.
- [120] J. Zhu, M. A. Antoniades, and G. V. Eleftheriades, "A compact tri-band monopole antenna with single-cell metamaterial loading," *IEEE Transaction on Antennas and Propagation*, vol. 58, pp. 1031–1038, 2010.
- [121] J. Ha, K. Kwon, Y. Lee, and J. Choi, "Hybrid mode wideband patch antenna loaded with a planar metamaterial unit cell," *IEEE Transaction on Antennas and Propagation*, vol. 60, pp. 1143–1147, 2012.
- [122] R. O. Ouedraogo, E. J. Rothwell, A. R. Diaz, K. Fuchi, and A. Temme, "Miniaturization of patch antennas using a metamaterial-inspired technique," *IEEE Transaction on Antennas and Propagation*, vol. 60, pp. 2175–2182, 2012.
- [123] M. S. Majedi and A. R. Attari, "A compact and broadband metamaterial-inspired antenna," *IEEE Antennas and Wireless Propagation Letters*, vol. 12, pp. 345–348, 2013.
- [124] X. Zhou, X. Quan, and R. Li, "A novel coplanar waveguide feed zeroth-order resonant antenna with resonant ring," *Antennas and Wireless Propagation Letters*, vol. 13, pp. 774–777, 2014.
- [125] P.-L. Chi and Y.-S. Shih, "Compact and bandwidth-enhanced zeroth-order resonant antenna," *IEEE Antennas and Wave Propagation Letters*, vol. 14, pp. 285–288, 2015.
- [126] M. A. Abdalla and A. A. Ibrahim, "Compact and closely spaced metamaterial MIMO antenna with high isolation for wireless applications," *IEEE Antennas and Wireless Propagation Letters*, vol. 12, pp. 1452–1455, 2013.
- [127] D. R. Smith, D. C. Vier, T. Koschny, and C. M. Soukoulis, "Electromagnetic parameter retrieval from inhomogeneous metamaterials," *Physical Review E*, vol. 71, 2005.

- [128] B. Bala, M. Rahim, and N. Murad, "Small electrical metamaterial antenna based on coupled electric field resonator with enhanced bandwidth," *Electronics Letters*, vol. 50, pp. 138–139, 2014.
- [129] Y. Li, T. Jiang, and R. Mittra, "A miniaturized dual-band antenna with toothbrush-shaped patch and meander line for WLAN applications," *Wireless Personal Communications*, vol. 91, no. 2, pp. 595–602, 2016.
- [130] R. Karli and H. Ammor, "Rectangular patch antenna for dual-band RFID and LAN applications," *Wireless Personal Communications*, vol. 83, no. 2, pp. 995–1007.
- [131] S. C. Basaran and K. Sertel, "Dual-band frequency-reconfigurable monopole antenna for WLAN applications," *Microwave and Optical Technology Letters*, vol. 57, no. 1, pp. 55–58, 2015.
- [132] L.-C. Tsai, "A dual-band bow-tie-shaped CPW-fed slot antenna for WLAN applications," *Progress In Electromagnetics Research C*, vol. 47, no. 167, pp. 167–171, 2014.
- [133] S. Yan, P. J. Soh, and G. A. E. Vandenbosch, "Compact all-textile dual-band antenna loaded with metamaterial-inspired structure," *IEEE Antennas and Wireless Propagation Letters*, vol. 14, pp. 1486–1489, 2015.
- [134] X. L. Sun, L. Liu, S. W. Cheung, and T. I. Yuk, "Dual-band antenna with compact radiator for 2.4/5.2/5.8 GHz WLAN applications," *IEEE Transactions on Antennas and Propagation*, vol. 60, no. 12, pp. 5924–5931, 2012.
- [135] M. S. M. Ali, S. K. A. Rahim, M. I. Sabran, M. Abedian, A. Eteng, and M. T. Islam, "Dual band miniaturized microstrip slot antenna for WLAN applications," *Microwave and Optical Technology Letters*, vol. 58, 06 2016.
- [136] R. Habibi, C. Ghobadi, J. Nourinia, M. Ojaroudi, and N. Ojaroudi, "Very compact broad

- band-stop filter using periodic L-shaped stubs based on self-complementary structure for X-band application.," *Electronics Letters*, vol. 48, no. 23, pp. 1483–1484, 2012.
- [137] D. La, Y. Lu, S. Sun, N. Liu, and J. Zhang, "A novel compact bandstop filter using defected microstrip structure," *Microwave and Optical Technology Letters*, vol. 53, pp. 433–435, 2010.
- [138] J. B. Pendry, A. J. Holden, D. J. Robbins, and W. J. Stewart, "Magnetism from conductors and enhanced nonlinear phenomena," *IEEE Transactions on Microwave Theory and Technology*, vol. 47, no. 11, pp. 2075–2084, 1999.
- [139] F. Falcone, T. Lopetegi, J. D. Baena, R. Marques, F. Martin, and M. Sorolla, "Effective negative epsilon stopband microstrip lines based on complementary split ring resonators," *IEEE Microwave and Wireless Components Letters*, vol. 14, pp. 280–282, 2004.
- [140] J.-C. Liu, D.-S. Shu, B.-H. Zeng, and D.-C. Chang, "Improved equivalent circuits for complementary split-ring resonator-based high-pass filter with C-shaped couplings," *IET Microwaves, Antennas and Propagation*, vol. 2, no. 6, pp. 622–626, 2008.
- [141] A. Velez, F. Aznar, J. Bonache, M. C. Velzquez-Ahumada, J. Martel, and F. Martn, "Open complementary split ring resonators (OCSRRs) and their application to wideband CPW band pass filters," *IEEE Microwave and Wireless Component Letters*, vol. 19, no. 4, pp. 197–199, 2009.
- [142] K.-T. Kim, J.-H. Ko, K. Choi, and H.-S. Kim, "Optimum design of wideband bandpass filter with CSRR-loaded transmission line using evolution strategy," *IEEE Transactions on Magnetics*, vol. 48, no. 2, pp. 811–814, 2012.
- [143] J. Bonache, M. Gil, I. Gil, J. Garcia-Garcia, and F. Martin, "On the electrical characteristics of complementary metamaterial resonators," *IEEE Microwave and Wireless Components Letters*, vol. 16, no. 10, pp. 543–545, 2006.

- [144] "Computer simulation technology microwave studio (CST MWS)."
- [145] "Computer simulation technology microwave studio (CST MWS)."
- [146] J. D. Baena, J. Bonache, F. Martn, R. M. Sillero, F. Falcone, T. Lopetegi, M. A. G. Laso, J. Garca-Garca, I. Gil, M. F. Portillo, and M. Sorolla, "Equivalent-circuit models for split-ring resonators and complementary split-ring resonators coupled to planar transmission lines," *IEEE Transaction on Microwave Theory and Techniques*, vol. 53, pp. 1151–1161, 2005.
- [147] A. Abdel-Rahman, A. K. Verma, A. Boutejdar, and A. S. Omar, "Compact stub type microstrip bandpass filter using defected ground plane," *IEEE Microwave and Wireless Components Letters*, vol. 14, pp. 136–138, 2004.
- [148] S. Karthikeyan and R. Kshetrimayum, "Composite right/left handed transmission line based on open slot split ring resonator," *Microwave and Optical Technology Letters*, vol. 52, no. 8, pp. 1729–1731, 2010.
- [149] "Computer simulation technology design studio (CST DS)."
- [150] H.-X. Xu, G.-M. Wang, and Q. Pengg, "Fractal-shaped complementary electric-LC resonator for bandstop filter," *Progress In Electromagnetics Research C*, vol. 23, pp. 205–217, 2011.
- [151] B. D. Bala, M. K. A. Rahim, and N. A. Murad, "Complementary electric-lc resonator antenna for WLAN applications," *Applied Physics A*, vol. 117, pp. 635–639, Nov 2014.
- [152] S. S. Karthikeyan and R. Kshetrimayum, "Composite right/left handed transmission line based on open slot split ring resonator," *Microwave and Optical Technology Letters*, vol. 52, no. 8, pp. 1729–1731, 2010.
- [153] M. Abessolo, Y. Diallo, A. Jaoujal, A. Moussaoui, and N. Aknin, "Stop-band filter

- using a new metamaterial complementary split triangle resonators (CSTRs)," vol. 28, pp. 353–358, 04 2013.
- [154] H. Nornikman, B. H. Ahmad, M. Z. A. A. Aziz, and A. R. Othman, "Effect of single complimentary split ring resonator structure on microstrip patch antenna design," in 2012 IEEE Symposium on Wireless Technology and Applications (ISWTA), pp. 239–244, Sept 2012.
- [155] V. Öznazı and V. B. Ertürk, "A comparative investigation of SRR- and CSRR-based band-reject filters: Simulations, experiments, and discussions," *Microwave and Optical Technology Letters*, vol. 50, no. 2, pp. 519–523, 2008.
- [156] C. Caloz and T. Itoh, *Electromagnetic Metamaterials: Transmission Line Theory and Microwave Applications*. Wiley-IEEE Press, 2005.
- [157] H. Nasraoui, A. Mouhsen, J. E. Aoufi, and M. Taouzari, "Novel microstrip low pass filter based on complementary split-ring resonators," *International Journal of Modern Communication Technologies and Research*, vol. 2, no. 10, 2014.
- [158] J. Bonache, G. Posada, G. Carchon, W. D. Raedt, and F. Martn, "Compact (< 0.5mm²) K-band metamaterial bandpass filter in MCM-D technology," *Electronics Letters*, vol. 43, no. 5, 2007.
- [159] A. L. Borja, J. Carbonell, J. D. Martinez, V. E. Boria, and D. Lippens, "A controllable bandwidth filter using varactor-loaded metamaterial-inspired transmission lines," *IEEE Antenna and Wireless Propagation Letters*, vol. 10, pp. 1575–1578, 2011.
- [160] C. Caloz, "Dual composite right/left-handed (D-CRLH) transmission line metamaterial," *IEEE Microwave and Wireless Components Letters*, vol. 16, no. 11, pp. 585–587, 2006.

- [161] V. Gonzalez-Posadas, J. L. Jimenez-Martin, A. Parra-Cerrada, L. E. Garcia-Munoz, and D. Segovia-Vargas, "Dual-composite right-left-handed transmission lines for the design of compact diplexers," *IET Microwaves, Antennas Propagation*, vol. 4, pp. 982–990, Aug 2010.
- [162] D. Kholodnyak, V. Turgaliev, and E. Zameshaeva, "Dual-band immittance inverters on dual-composite right/left-handed transmission line (D-CRLH TL)," in *German Microwave Conference*, pp. 60–63, 2015.
- [163] A. Belenguer, J. Cascón, A. L. Borja, H. Esteban, and V. E. Boria, "Dual composite right-/left-handed coplanar waveguide transmission line using inductively connected split-ring resonators," *IEEE Transaction on Microwave Theory and Techniques*, vol. 60, no. 10, pp. 3035–3042, 2012.
- [164] L. M. Cano, A. L. Borja, V. E. Boria, and A. Belenguer, "Highly versatile coplanar waveguide line with electronically reconfigurable bandwidth and propagation characteristics," *IEEE Transaction on Microwave Theory and Techniques*, 2016.
- [165] J. D. Baena, J. Bonache, F. Martn, R. M. Sillero, F. Falcone, T. Lopetegi, M. A. G. Laso, J. Garca-Garca, I. Gil, M. F. Portillo, and M. Sorolla, "Equivalent-circuit models for split-ring resonators and complementary split-ring resonators coupled to planar transmission lines," *IEEE Transaction on Microwave Theory and Techniques*, vol. 53, pp. 1151–1161, 2005.
- [166] D. R. Smith, D. C. Vier, T. Koschny, and C. M. Soukoulis, "Electromagnetic parameter retrieval from inhomogeneous metamaterials," *Physical Review E*, vol. 71, 2005.
- [167] P. Bhartia and I. Bahl, *Microwave solid state circuit design*. Wiley, 2003.
- [168] X. Ying and A. Alphones, "Propagation characteristics of complimentary split ring resonator (CSRR) based ebg structure," *Microwave and Optical Technology Letters*, vol. 47, no. 5, pp. 409–412, 2005.

- [169] D. K. Choudhary and R. K. Chaudhary, "A compact via-less metamaterial wideband bandpass filter using split circular rings and rectangular stub," *Progress In Electromagnetics Research*, vol. 72, pp. 99–106, 2018.
- [170] L. Liu, P. Zhang, M.-H. Weng, C.-Y. Tsai, and R.-Y. Yang, "A miniaturized wideband bandpass filter using quarter-wavelength stepped-impedance resonators," *Electronics*, vol. 8, no. 12, p. 1540, 2019.
- [171] M.-C. Tang, T. Shi, and X. Tan, "A novel triple-mode hexagon bandpass filter with meander line and central-loaded stub," *Microwave and Optical Technology Letters*, vol. 58, no. 1, pp. 9–12, 2016.
- [172] K.-D. Xu, D. Li, and Y. Liu, "High-selectivity wideband bandpass filter using simple coupled lines with multiple transmission poles and zeros," *IEEE Microwave and Wireless Components Letters*, vol. 29, no. 2, pp. 107–109, 2019.
- [173] W. Emerson, "Electromagnetic wave absorbers and anechoic chambers through the years," *IEEE Transactions on Antennas and Propagation*, vol. 21, no. 4, pp. 484–490, 1973.
- [174] E. F. Knott, J. F. Schaeffer, and M. T. Tulley, *Radar cross section*. SciTech Publishing, 2004.
- [175] Q. Song, W. Zhang, P. C. Wu, W. Zhu, Z. X. Shen, P. H. J. Chong, Q. X. Liang, Z. C. Yang, Y. L. Hao, H. Cai, et al., "Water-resonator-based metasurface: An ultrabroadband and near-unity absorption," Advanced Optical Materials, vol. 5, no. 8, p. 1601103, 2017.
- [176] N. Engheta, "Thin absorbing screens using metamaterial surfaces," in *IEEE Antennas and Propagation Society International Symposium (IEEE Cat. No. 02CH37313)*, vol. 2, pp. 392–395, IEEE, 2002.

- [177] D. R. Smith, W. J. Padilla, D. Vier, S. C. Nemat-Nasser, and S. Schultz, "Composite medium with simultaneously negative permeability and permittivity," *Physical review letters*, vol. 84, no. 18, p. 4184, 2000.
- [178] C. M. Watts, X. Liu, and W. J. Padilla, "Metamaterial electromagnetic wave absorbers," *Advanced materials*, vol. 24, no. 23, pp. OP98–OP120, 2012.
- [179] S. Ghosh, S. Bhattacharyya, D. Chaurasiya, and K. V. Srivastava, "An ultrawideband ultrathin metamaterial absorber based on circular split rings," *IEEE antennas and wireless propagation letters*, vol. 14, pp. 1172–1175, 2015.
- [180] D. Ye, Z. Wang, Z. Wang, K. Xu, B. Zhang, J. Huangfu, C. Li, and L. Ran, "Towards experimental perfectly-matched layers with ultra-thin metamaterial surfaces," IEEE Transactions on Antennas and Propagation, vol. 60, no. 11, pp. 5164–5172, 2012.
- [181] N. Mishra, D. K. Choudhary, R. Chowdhury, K. Kumari, and R. K. Chaudhary, "An investigation on compact ultra-thin triple band polarization independent metamaterial absorber for microwave frequency applications," *IEEE access*, vol. 5, pp. 4370–4376, 2017.
- [182] B.-X. Wang, X. Zhai, G. Wang, W. Huang, and L. Wang, "Design of a four-band and polarization-insensitive terahertz metamaterial absorber," *IEEE Photonics Journal*, vol. 7, no. 1, pp. 1–8, 2015.
- [183] B.-X. Wang, "Quad-band terahertz metamaterial absorber based on the combining of the dipole and quadrupole resonances of two SRRs," *IEEE Journal of Selected Topics in Quantum Electronics*, vol. 23, no. 4, pp. 1–7, 2017.
- [184] A. Sarkhel and S. R. B. Chaudhuri, "Compact quad-band polarization-insensitive ultrathin metamaterial absorber with wide angle stability," *IEEE Antennas and Wireless Propagation Letters*, vol. 16, pp. 3240–3244, 2017.

- [185] D. Chaurasiya, S. Ghosh, S. Bhattacharyya, and K. V. Srivastava, "An ultrathin quadband polarization-insensitive wide-angle metamaterial absorber," *Microwave and Optical Technology Letters*, vol. 57, no. 3, pp. 697–702, 2015.
- [186] A. Bhattacharya, S. Bhattacharyya, S. Ghosh, D. Chaurasiya, and K. Vaibhav Srivastava, "An ultrathin penta-band polarization-insensitive compact metamaterial absorber for airborne radar applications," *Microwave and Optical Technology Letters*, vol. 57, no. 11, pp. 2519–2524, 2015.
- [187] N. Mishra, K. Kumari, and R. K. Chaudhary, "An ultra-thin polarization independent quad-band microwave absorber-based on compact metamaterial structures for EMI/EMC applications," *International Journal of Microwave and Wireless Technologies*, vol. 10, no. 4, pp. 422–429, 2018.
- [188] Ansoft, "HFSS simulator version 14.0."
- [189] S. Ghosh and K. V. Srivastava, "An equivalent circuit model of fss-based metamaterial absorber using coupled line theory," *IEEE Antennas and Wireless Propagation Letters*, vol. 14, pp. 511–514, 2015.
- [190] C. L. Holloway, E. F. Kuester, and A. Dienstfrey, "Characterizing metasurfaces/metafilms: The connection between surface susceptibilities and effective material properties," *IEEE Antennas and Wireless Propagation Letters*, vol. 10, pp. 1507–1511, 2011.
- [191] D. Smith, D. Vier, T. Koschny, and C. Soukoulis, "Electromagnetic parameter retrieval from inhomogeneous metamaterials," *Physical review E*, vol. 71, no. 3, p. 036617, 2005.
- [192] X. Zeng, M. Gao, L. Zhang, G. Wan, and B. Hu, "Design of a triple-band metamaterial absorber using equivalent circuit model and interference theory," *Microwave and Optical Technology Letters*, vol. 60, no. 7, pp. 1676–1681, 2018.

- [193] R. Asgharian, B. Zakeri, and O. Karimi, "Modified hexagonal triple-band metamaterial absorber with wide-angle stability," *AEU International Journal of Electronics and Communications*, vol. 87, pp. 119 123, 2018.
- [194] F. S. Jafari, M. Naderi, A. Hatami, and F. B. Zarrabi, "Microwave jerusalem cross absorber by metamaterial split ring resonator load to obtain polarization independence with triple band application," *AEU International Journal of Electronics and Communications*, vol. 101, pp. 138 144, 2019.
- [195] Da-Shan Shiu, G. J. Foschini, M. J. Gans, and J. M. Kahn, "Fading correlation and its effect on the capacity of multielement antenna systems," *IEEE Transactions on Communications*, vol. 48, no. 3, pp. 502–513, 2000.
- [196] A. F. Molisch, M. Z. Win, Yang-Seok Choi, and J. H. Winters, "Capacity of MIMO systems with antenna selection," *IEEE Transactions on Wireless Communications*, vol. 4, no. 4, pp. 1759–1772, 2005.
- [197] R. Chandel and A. K. Gautam, "Compact MIMO/diversity slot antenna for UWB applications with band-notched characteristic," *Electronics Letters*, vol. 52, no. 5, pp. 336–338, 2016.
- [198] G. Lin, C. Sung, J. Chen, L. Chen, and M. Houng, "Isolation improvement in UWB MIMO antenna system using carbon black film," *IEEE Antennas and Wireless Propagation Letters*, vol. 16, pp. 222–225, 2017.
- [199] I. Buriak, V. Zhurba, G. Vorobjov, V. Kulizhko, O. Kononov, and O. Rybalko, "Metamaterials: Theory, classification and application strategies," *Journal Of Nano- And Electronic Physics*, vol. 8, no. 4 (2), pp. 04088–1, 2016.
- [200] N. I. Landy, S. Sajuyigbe, J. J. Mock, D. R. Smith, and W. J. Padilla, "Perfect metamaterial absorber," *Physical Review Letters*, vol. 100, no. 4, pp. 207–402, 2008.

- [201] S. Ji, C. Jiang, J. Zhao, X. Zhang, and Q. He, "Design of a polarization-insensitive triple-band metamaterial absorber," *Optics Communications*, vol. 432, pp. 65 70, 2019.
- [202] S. Narayan, B. Sangeetha, T. V. Sruthi, V. Shambulingappa, and R. U. Nair, "Design of low observable antenna using active hybrid-element FSS structure for stealth applications," AEU - International Journal of Electronics and Communications, vol. 80, pp. 137–143, 2017.
- [203] M. Bagmanc, M. Karaaslan, E. Unal, O. Akgol, F. Karadag, and C. Sabah, "Broadband polarization-independent metamaterial absorber for solar energy harvesting applications," *Physica E: Low-dimensional Systems and Nanostructures*, vol. 90, pp. 1–6, 2017.
- [204] M. Bakr, M. Karaaslan, E. Unal, O. Akgol, and C. Sabah, "Microwave metamaterial absorber for sensing applications," *Opto-Electronics Review*, vol. 25, no. 4, pp. 318 325, 2017.
- [205] M. Agarwal and M. K. Meshram, "Isolation improvement of 5 GHz WLAN antenna array using metamaterial absorber," in 2016 URSI Asia-Pacific Radio Science Conference (URSI AP-RASC), pp. 1050–1053, 2016.
- [206] Q. Zhang, Y. Jin, J. Feng, X. Lv, and L. Si, "Mutual coupling reduction of microstrip antenna array using metamaterial absorber," in 2015 IEEE MTT-S International Microwave Workshop Series on Advanced Materials and Processes for RF and THz Applications (IMWS-AMP), pp. 1–3, 2015.
- [207] H. S. Lee and H. M. Lee, "Isolation improvement between loop antennas with absorber cells," in 2011 IEEE International Symposium on Antennas and Propagation (APSURSI), pp. 1735–1738, 2011.

- [208] C. M. Watts, X. Liu, and W. J. Padilla, "Metamaterial electromagnetic wave absorbers," *Advanced materials*, vol. 24, no. 23, pp. OP98–OP120, 2012.
- [209] G. Srivastava and A. Mohan, "Compact MIMO slot antenna for UWB applications," *IEEE Antennas and Wireless Propagation Letters*, vol. 15, pp. 1057–1060, 2016.
- [210] S. R. Thummaluru and R. K. Chaudhary, "Mu-negative metamaterial filter-based isolation technique for MIMO antennas," *Electronics Letters*, vol. 53, no. 10, pp. 644–646, 2017.
- [211] K. J. Babu, R. W. Aldhaheri, M. Talha, and I. SAlruhaili, "Design of a compact two element MIMO antenna system with improved isolation," *Progress In Electromagnetics Research*, vol. 48, pp. 27–32, 2014.
- [212] H. Arun, A. K. Sarma, M. Kanagasabai, S. Velan, C. Raviteja, and M. G. N. Alsath, "Deployment of modified serpentine structure for mutual coupling reduction in MIMO antennas," *IEEE Antennas and Wireless Propagation Letters*, vol. 13, pp. 277–280, 2014.
- [213] C. Xue, X. Y. Zhang, Y. F. Cao, Z. Hou, and C. F. Ding, "MIMO antenna using hybrid electric and magnetic coupling for isolation enhancement," *IEEE Transactions on Antennas and Propagation*, vol. 65, no. 10, pp. 5162–5170, 2017.

LIST OF PUBLICATIONS

In peer reviewed International Journals

- Priyanka Garg and Priyanka Jain, "Design and analysis of Complementary split ring resonator backed microstrip transmission line using equivalent circuit model" *Journal* of Communication Technology and Electronics, vol. 63, no. 12, pp. 1424-1430, 2018. (SCI Journal with Impact Factor: 0.51)
- Priyanka Garg and Priyanka Jain, "Design and analysis of a metamaterial inspired dual band antenna for WLAN application" *International Journal of Microwave and Wireless Technologies*, vol. 11, no. 4, pp. 351-358, 2019. (SCIE Journal with Impact factor: 0.703)
- 3. **Priyanka Garg** and Priyanka Jain, "Isolation Improvement of MIMO Antenna Using a Novel Flower Shaped Metamaterial Absorber at 5.5 GHz WiMAX Band," *IEEE Transactions on Circuits and Systems II: Express Briefs*, vol. 67, no. 4, pp. 675-679, April 2020. (SCI Journal with Impact factor: 3.25)
- 4. **Priyanka Garg** and Priyanka Jain, "Novel ultrathin penta-band metamaterial absorber", *AEU International Journal of Electronics and Communications*, vol. 116, p. 153063, 2020. (SCIE Journal with Impact factor: 2.853).
- Priyanka Garg and Priyanka Jain, "Design and analysis of a bandpass filter using Dual Composite Right/Left Handed (D-CRLH) transmission line showing bandwidth enhancement", Wireless Personal Communication. (Communicated) (SCIE Journal with Impact factor: 1.061).

- 6. **Priyanka Garg** and Priyanka Jain, "Metamaterial-based patch antennas-Review" *Advances in System Optimization and Control*, vol. 509, pp 65-81, 2019. (SCOPUS)
- 7. **Priyanka Garg** and Priyanka Jain, "Extraction of equivalent circuit parameters of metamaterial-based bandstop filter," *Applications of Artificial Intelligence Techniques in Engineering*, vol. 697, pp. 173-179, 2019. (SCOPUS)

In International/national conferences

- Priyanka Garg, Shruti Awasthi and Priyanka Jain "A survey of microwave bandpass filter using coupled line resonator - Research design and development", Proceeding of International Conference on Sustainable Energy, Electronics and Computing Systems (SEEMS), October 27-28, 2018.
- Priyanka Garg and Priyanka Jain "Comparative analysis of transmission line based bandstop filters using different metamaterial unit cells operating at 3 GHz" Proceeding of International Conference on Signal Processing, VLSI and Communication Engineering (ICSPVCE-2019), March 28-30, 2019, New Delhi, India.
- 3. **Priyanka Garg** and Priyanka Jain, "Analysis of a novel metamaterial absorber using equivalent circuit model operating at 3.5 GHz", presented in *IEEE International Conference on Computational Electromagnetics (ICCEM-2020)*, Singapore, 2020.
- 4. Priyanka Garg and Priyanka Jain, "Analysis of metamaterial based bandstop filters: A Brief Review" presented in 5th International Conference on Microelectronics, Computing & Communication Systems (MCCS-2020), July 11-12, 2020, Advanced Regional Telecom Training Centre, BSNL, Ranchi, Jharkhand, India.
- Priyanka Garg and Priyanka Jain, "A Review of Multiband Metamaterial Absorbers" presented in *National Conference on Microwave Absorbing Materials (VAMMAM-2020)*, Aug 23-24, 2020, Roorkee, India.

CURRICULUM VITAE

Priyanka Garg

H.no. 101,

NCR Residency,

GMS Road, Dehradun-248171

Uttarakhand.

e-mail: priyankagarg_phd2k16@dtu.ac.in

+91-8800943503



Priyanka Garg was born in Dehradun, Uttarakhand state of India, on December 28, 1992. She received her B.Tech degree (Electronics & communication) in 2013 from Uttarakhand Technical University, Uttarakhand, India, and M.Tech. (Digital Signal Processing) in 2016 from G.B. Pant Engineering College, Pauri, Uttarakhand, India. She enrolled for the doctorate degree in Electronics & Communication Engineering at the Delhi Technological University, Delhi, India in 2016. She has published more than 10 research papers in reputed journals/conferences like IEEE, etc. Her main research interests are design and optimization of metamaterial based microwave components. Currently she is working on metamaterial based antennas, filters and absorbers.